UNIVERSIDADE DA BEIRA INTERIOR
Engenharia

Combustion of CH_4, H_2, and $CH_4 - H_2$ Mixtures in a Gas Turbine Can Combustor

Daniela Filipa Martins Santos

Dissertação para obtenção do Grau de Mestre em

Engenharia Aeronáutica

(Ciclo de estudos integrado)

Orientador: Prof. Doutor Francisco Miguel Ribeiro Proença Brójo

Covilhã, Outubro de 2014

Dedication

To my parents

José Santos and Manuela Moreira

who always believed and inspired me.

Acknowledgments

Foremost, I would like to express my sincere gratitude to my advisor Prof. Francisco Brójo, for his excellent guidance, patient, motivation, enthusiasm, and immense knowledge. His guidance helped me in all the time of research and writing of this dissertation. I could not have imagined having a better advisor and mentor.

I would like to be grateful to my parents José Santos and Manuela Moreira and my family that were always supporting and encouraging me with their best wishes, which without them I would never have been able to finish this dissertation.

I would like to thank my friends, especially Hugo Sousa for all his help and Cristina Vieira who always had confidence in me.

Finally, I would like to thank Paulo Marchão, he was always there helping me, cheering me up and stood by me through all the good and bad times.

"You know, Stanley, when we designed the Proteus I decided we should make the engine with the lowest fuel consumption in the world, regardless of its weight and bulk. So far, we have achieved the weight and bulk!" - Proteus Chief Engineer Frank Owner to Chief Engineer of the Engine Division Stanley Hooker.

Abstract

The fact that there is an increase in the price of fossil fuels, and that environmental changes are occurring due to pollutant emissions, makes it imperative to find alternative fuels that are less polluting and cheaper.

Gas turbines have been particularly developed as aviation engines, but nowadays they can find applicability in many areas and the fact that they have multiple fuel applications, makes them a very important subject of study.

The main objective of this dissertation is to evaluate through a CFD analysis on FLUENT the performance of the combustion in a gas turbine can combustor, fed with methane, hydrogen and methane-hydrogen mixtures taking a particular interest in the pollutants emissions.

In the end a fuel optimization was carried on to evaluate the average mass fraction of the pollutants CO, CO_2 and NO_x at the exit of the can combustor, and also a brief evaluation of the static temperature and pressure, and velocity magnitude in the several CFD simulations was executed.

Keywords

CFD, FLUENT, Gas Turbine, Can Combustor, Combustion, Methane (CH_4), Hydrogen (H_2), Pollutants.

Resumo

O facto do preço dos combustíveis fósseis estar cada vez mais elevado, e de estarem a ocorrer mudanças ambientais devido à emissão de poluentes por parte destes combustíveis torna imperativo encontrar combustíveis alternativos mais baratos e menos poluentes.

As turbinas de gás têm sido particularmente desenvolvidas como motores de aeronaves, no entanto nos dias que correm elas podem encontrar aplicabilidade nas mais diversas áreas, e aliando a isto o facto das turbinas de gás possuírem diferentes aplicabilidades de combustíveis faz delas um importante tema de estudo.

Sendo assim o principal objectivo desta dissertação é avaliar através de uma análise CFD no FLUENT o desempenho da combustão num "can combustor" de uma turbina de gás, quando alimentado com metano, hidrogénio e misturas de metano-hidrogénio, tendo especial interesse na emissão de poluentes.

Posto isto foi realizada uma optimização do combustível por forma a avaliar os valores médios da fracção mássica dos poluentes CO, CO_2 e NO_x à saída do "can combustor", e de notar que uma breve análise à temperatura estática, à pressão estática e à magnitude da velocidade das várias simulações foi também executada.

Palavras-chave

CFD, FLUENT, Turbina de Gás, "Can Combustor", Combustão, Metano (CH_4), Hidrogénio (H_2), Poluentes.

Contents

Figure List

Table List

Abbreviations List

CFD	*Computational Fluid Dynamics*
WWII	*World War II*
CCC	*Catalytic Combustion Chamber*
VAMCAT	*Ventilation Air Methane Catalytic Combustion Chamber*
EGR	*Exhaust Gas Recirculation*
PSR	*Perfectly Stirred Reactor*
IGCC	*Integrated Gasification Combined Cycle*
IRCC	*Integrated Reforming Combined Cycles*
HCF	*Hydrogen Containing Fuels*
SNG	*Synthetic Natural Gas*
DLN	*Dry Low* NO_x
SCR	*Selective Catalytic Reduction*
SRC	*Solvent Refined Coal*
EI	*(Pollutant) Emission Index*
CDC	*Colorless Distributed Combustion*
HCCI	*Homogeneous Charge Compression Ignition*
RANS	*Reynolds Averaged Navier-Stokes*
SST	*Shear-Stress Transport*
EWT	*Enhance Wall Treatment*
CAD	*Computer Aided Design*
fmean	*Mean mixture fraction*
fvar	*Mixture fraction variance*
UHC	*Unburned Hydrocarbons*

Nomenclature

ϕ	*Equivalence ratio*
k	*Turbulence kinetic energy*
ε	*Rate of dissipation*
S_m	*Mass added to the continuous phase from the dispersed second phase and any user-defined sources*
ρ	*Static pressure*
$\bar{\bar{\tau}}$	*Stress tensor*
$\rho\vec{g}$	*Gravitational body force*
$\vec{F}$	*External body forces*
μ	*Molecular viscosity*
I	*Unit tensor*
G_k	*Generation of turbulence kinetic energy due to the mean velocity gradients*
G_b	*Generation of turbulence kinetic energy due to buoyancy*
Y_M	*Contribution of the fluctuating dilatation in compressible turbulence to the overall dissipation rate*
$C_{1\varepsilon}$, $C_{2\varepsilon}$, $C_{3\varepsilon}$	*Constants*
σ_k	*Turbulent Prandtl number for* k
σ_ε	*Turbulent Prandtl number for* ε
S_k, S_ε	*User-defined source terms*
μ_t	*Turbulent (or eddy) viscosity*
C_μ	*Constant (in the Standard and RNG* $k-\varepsilon$ *model)*
α_k	*Inverse effective Prandtl number for* k
α_ε	*Inverse effective Prandtl number for* ε
$\overline{u^2}$	*Normal Reynolds stress*
$\overline{\Omega_{ij}}$	*Mean rate-of-rotation tensor viewed in a moving reference frame*
ω_k	*Angular velocity*
A_0, A_S	*Model constants*
C_μ	*Function of the mean strain and rotation rates, the angular velocity of the system rotation, and the turbulence fields (in the Realizable* $k-\varepsilon$ *model)*
C_2	*Constant*
σ_k, σ_ε	*Constants (in the Realizable* $k-\varepsilon$ *model)*
ω	*Specific dissipation rate*
G_ω	*Generation of* ω
Γ_k	*Effective diffusivity of* k
Γ_ω	*Effective diffusivity of* ω
Y_k	*Dissipation of* k *due to turbulence*

Y_ω	*Dissipation of* ω *due to turbulence*
S_k, S_ω	*User-defined source terms*
σ_ω	*Turbulent Prandtl number for* ω
α^*	*Coefficient that damps the turbulent viscosity*
S	*Modulus of the mean rate-of-strain tensor*
Y_k	*Dissipation of* k
S_{ij}	*Strain tensor*
$\mathrm{F}(\mathrm{M_t})$	*Compressibility function*
α^*_∞, α_∞, α_0, β^*_∞, β_i, R_β, R_k, R_ω, ζ^*, M_{t0}, σ_k, σ_ω	*Constants (of the Standard* $k-\omega$ *Model)*
$\widetilde{G}_k$	*Generation of turbulence kinetic energy due to mean velocity gradients*
D_ω	*Cross-diffusion term*
S	*Strain rate magnitude (in the SST* $k-\omega$ *Model)*
F_1, F_2	*Blending functions*
y	*Distance to the next surface*
D^+_ω	*Positive portion of the cross-diffusion term*
f_{β^*}	*Piecewise function*
$\sigma_{k,1}$, $\sigma_{\omega,1}$, $\sigma_{k,2}$, $\sigma_{\omega,2}$, a_1, $\beta_{i,1}$, $\beta_{i,2}$, α^*_∞, α_∞, α_0, β^*_∞, R_β, R_k, R_ω, ζ^*, M_{t0}	*Constants (of the SST* $k-\omega$ *Model)*
f	*Mixture Fraction*
Re	*Reynolds number*
I	*Radiation intensity*
q_r	*Radiation flux*
a	*Absorption coefficient*
σ_S	*Scattering coefficient*
G	*Incident radiation*
C	*Linear-anisotropic phase function coefficient*
n	*Refractive index of the medium*
σ	*Stefan-Boltzmann constant*
$\mathrm{S_G}$	*User-defined radiation source*
y^+	*Non-dimensional wall distance for a wall-bounded flow*
u_*	*Friction velocity at the nearest wall*
ν	*Local kinematic viscosity of the fluid*

u_τ	*Friction velocity*

Chapter 1

Introduction

In this opening chapter it will be presented a succinct description of the main goals of this study and its importance to the development of the aeronautical field as many other areas. It is also disclosed, briefly, the structure of the dissertation.

1.1 Motivation

The gas turbine is a power plant, which produces a great amount of energy for its size and weight [1], and has multiple fuel applications. They have been particularly developed as aviation engines, although they can find applicability in many areas.

Becoming aware of this, the reason that lead me to choose this subject resides on the fact that there is an increasing cost of fossil fuels and also environmental changes that make it necessary to find alternative fuels that are less polluting and cheaper.

1.2 Main Goals

The main purpose of the present study is to evaluate, through a CFD analysis on FLUENT, the performance of the combustion in a gas turbine can combustor, fed with methane, hydrogen, and methane-hydrogen mixtures without any changes of the general combustion system, taking special interest in the pollutants emissions.

1.3 Framework

After World War II, gas turbines became the most popular method of powering airplanes. But its history comes way long back in time, as displayed in Table 1.

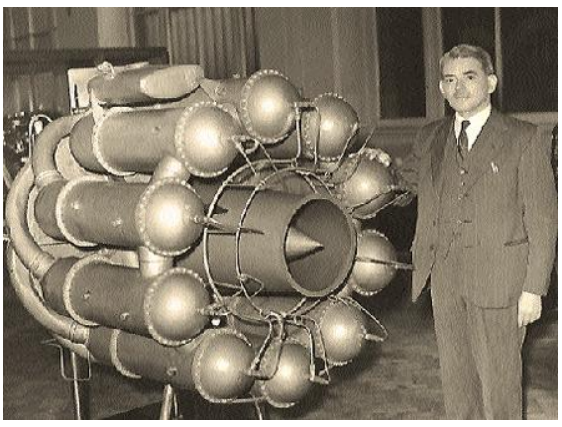

Figure 1 - Sir Frank Whittle and his multi-combustor jet turbine (Circa **1941**) [2].

Table 1 - Timeline of Gas Turbine Engines [3].

Timeline of Gas Turbine Engines

150 *BC*	Heron of Alexandria invented the *Aeolipile* (Figure 2) that rotated on top of a boiling pot of water. This caused a reaction effect of hot air or steam that moved several nozzles arranged on a wheel.
1500	Leonardo Da Vinci also has ties to gas turbine history. He designed a machine called the "chimney jack". The chimney jack was used to turn a roasting skewer. Heat from the fire would rise up and pass through fan-like blades in the chimney. These blades would then turn a series of gears to turn the skewer.
1629	Italian engineer Giovanni Branca invented an impulse turbine. His invention was a stamping mill. Power was generated by a steam-powered turbine. A nozzle directed steam onto a turbine wheel, which then turned a series of gears to operate his mill.
1687	Sir Isaac Newton announced his three laws of motion. These laws would have a significant impact on future inventions including development of the gas turbine engine.
1791	John Barber (an Englishman) patented the first gas turbine engine. His design was planned to propel a "horseless carriage." Barber's design used the thermodynamic cycle we are familiar with in the modern gas turbine — it had a compressor, a combustion chamber, and a turbine.
1872	Dr. F. Stolze designed the first true gas turbine engine. Stolze's engine used a multistage turbine section and a flow compressor. This engine never ran under its own power.
1903	While the Wright brothers were on their way to become the first to powered flight, Aegidius Elling of Norway managed to build the first successful gas turbine using both rotary compressors and turbines.
1918	General Electric started a gas turbine division. Dr. Stanford A. Moss developed the GE turbosupercharger during World War I. It used exhaust gas from piston engines to drive a turbine wheel. This in turn drove a centrifugal compressor that was used for supercharging.
1930	Englishman, Sir Frank Whittle (Figure 1), submitted a patent application for a gas turbine for jet propulsion. His engine, which had a single-stage centrifugal compressor coupled to a single-stage turbine, was successfully bench tested in April 1937.
1936	While Whittle was working on his engine, Germans Hans von Ohain and Max Hahn patented a jet propulsion engine of their own.
1939	The Ernst Heinkel Aircraft Company adapted their ideas and flew the second aircraft engine of this development in an HE-178 aircraft on August 27, 1939 in what would be the first true jet-propelled aircraft.
1941	In May 1941 the Whittle W1 engine made its first flight mounted on the Gloster Model E28/39 aircraft. This aircraft later achieved a speed of $370\ mph$ ($\cong 595.46\ km/h$) in level flight with $1\ 000$ pounds of thrust.

1942 German Scientist Dr. Franz Anslem developed the axial flow turbojet, the Junkers Jumo 004, which was used in the Messerschmitt ME 262, the world's first operational jet fighter.

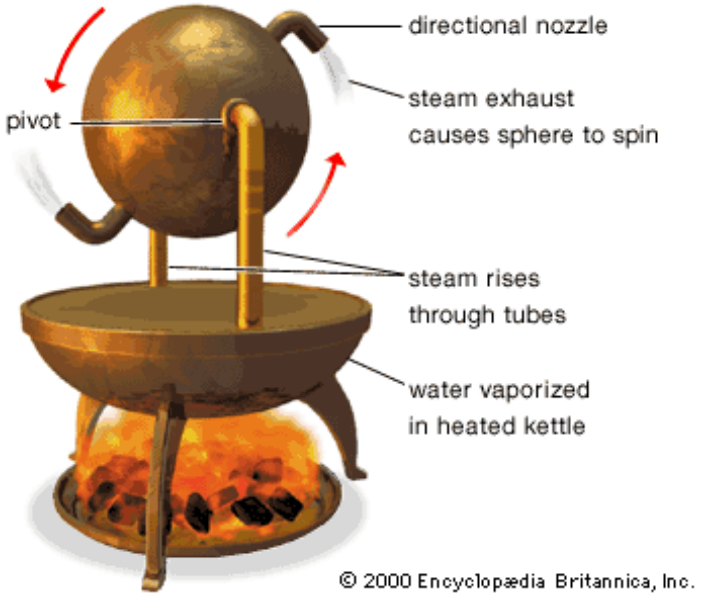

Figure 2 - Heron's *Aeolipile* illustration [4].

Nowadays the developments in the gas turbines field continue in order to obtain more efficient turbine engines.

One of the most important things to consider in order to improve the performance of gas turbines is the used fuel. A fuel is a substance that, when heated, suffers a chemical oxidation reaction where heat is released using, in most cases, the oxygen present in the air [5]. There has been a significant evolution on the type of fuels used by Man, being the first known use of fuel the combustion of wood or sticks by *Homo erectus* near 2 000 000 years ago [6], passing by the fossil fuels and todays new alternative fuels, like hydrogen (chemical information about the element hydrogen can be seen in Figure 3).

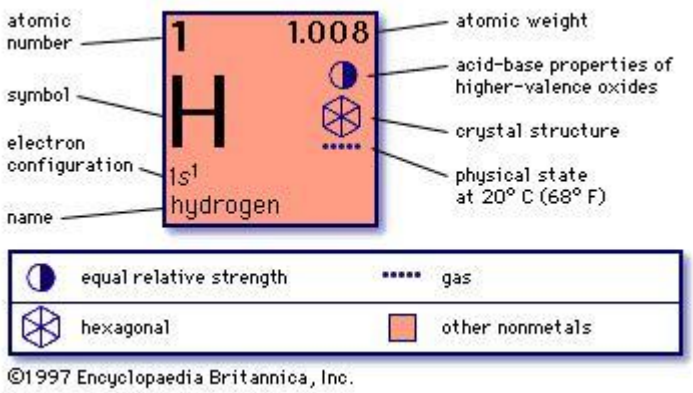

Figure 3 - Hydrogen information [7].

1.4 Work Overview

Apart from the introductory chapter (**Chapter 1**) the present dissertation is structured the following way

- **Chapter 2 -** In this chapter is made a literature review and presented some of the main developments that have occur in the usage of methane and hydrogen as fuels in gas turbines.
- **Chapter 3 -** This chapter explains the theoretical concepts about the fundamental equations used on this dissertation.
- **Chapter 4** - Here on this chapter are defined many important aspects of this dissertation, like the geometry of the combustion chamber, the generated mesh, etc., and most important it describes the validation of the numerical model.
- **Chapter 5** - Probably one of the most important chapters of this work, on Chapter 5 are described the several steps made over the fuel optimization and are exposed the obtained results.
- **Chapter 6 -** In this final chapter are presented the dissertation conclusions and some proposals for future work and research.

Chapter 2

State of the Art

This section lists the current knowledge in the field of this research and contains the respective references.

2.1 Literature Review

This work focus on the combustion of methane, hydrogen and methane-hydrogen mixtures on a gas turbine can combustor as it will be explained in more detail later on Chapter 5.

Like revealed in Table 1 the history of gas turbines comes way back in time, although its use and main developments have occur majorly after WWII. There are different types of combustion chambers, but all gas turbine combustors provide the same function. There are two basic types of combustor, tubular and annular, being the one used on this study a tubular or can combustor. A compromise between these two types is the "tuboannular" or "can-annular" combustor [8].

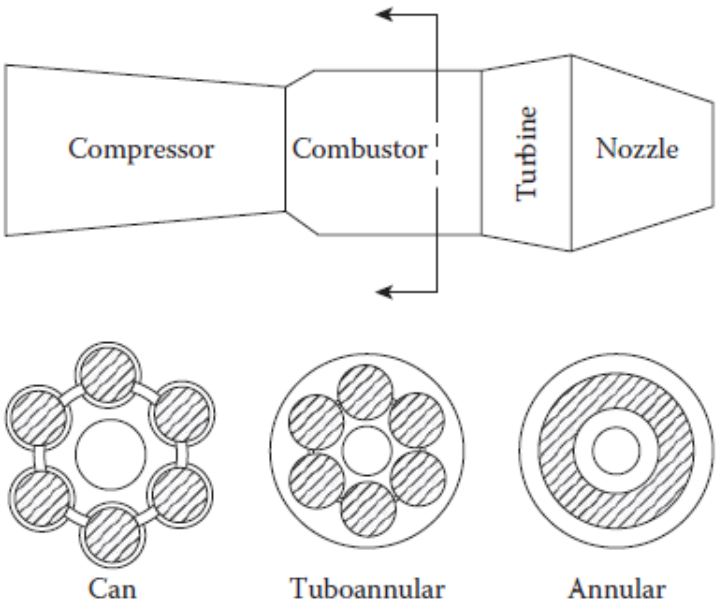

Figure 4 - Illustration of three main combustor types [8].

These three types of combustor are briefly described in Table 2, and are represented in Figure 4.

Table 2 – Gas turbine combustor types brief description [8].

Combustor Types	
Tubular	A tubular (or "can") combustor is comprised of a cylindrical liner mounted concentrically inside a cylindrical casing. *Advantages* • Relatively little time and money is incurred in their development. *Disadvantages* • Excessive length and weight prohibit their use in aircraft engines.
Tuboannular	This design, a group of tubular liners, usually from 6 to 10, is arranged inside a single annular casing. This concept attempts to combine the compactness of the annular chamber with the mechanical strength of the tubular chamber. *Advantages* • Much useful chamber development can be carried out with very modest air supplies, using just a small segment of the total chamber containing one or more liners. *Disadvantages* • Need for interconnectors; • The design of the diffuser can present serious difficulties.
Annular	In this type, an annular liner is mounted concentrically inside an annular casing. *Advantages* • Clean aerodynamic layout results in a compact unit of lower pressure loss than other combustor types. *Disadvantages* • Stems from the heavy buckling load on the outer liner.

Being very abundant in nature, methane is the main component of natural gas, and its content in the natural gas several deposits, can reach about 95%. Consequently it's an excellent chemical compound to be used as a fuel, being also claimed to be more environmentally friendly than other fossil fuels [9]. Knowing that, many studies have been done using this substance as fuel.

On the other hand, unlike methane, hydrogen can be produced from renewable energy sources such as solar or wind energy or through water electrolysis.

Hydrogen has unique characteristics that make it an ideal energy carrier, and that will allow it to be used in every application where fossil fuels are being used today [10]. These include the fact that:

- It can be produced from and converted into electricity at relatively high efficiencies;

- Its raw material for production is water, which is available in abundance;
- It is a completely renewable fuel;
- It can be stored in gaseous form (convenient for large-scale storage), in liquid form (convenient for air and space transportation), or in the form of metal hydrides (convenient for surface vehicles and other relatively small-scale storage requirements);
- It can be transported over large distances through pipelines or via tankers;
- It can be converted into other forms of energy in more ways and more efficiently than any other fuel (such as catalytic combustion, electrochemical conversion, and hydriding);
- It is environmentally compatible since its production, storage, transportation, and end use do not produce any pollutants (except for small amounts of nitrogen oxides), greenhouse gases, or any other harmful effects on the environment.

As a result hydrogen is being widely study, and presenting curious results that maybe will allow it, in a nearby future, grow to be one of the most utilized fuels.

2.1.1 Relevant Studies

Through the years many studies have been done some more relevant than others, but no less important, as they all have contributed to the advancement of knowledge.

Knowing that some relevant and recent researches are exposed here confirming the importance of fuel optimization in the process of combustion in a gas turbine; making reference essentially to the works that use methane and hydrogen as fuel.

The attempt to increase the efficiency of the combustion is a very current subject, although it is being done for several years now, in this work are exposed some studies made especially through the past 10 years, but some previous works are also referred.

In year 1997, for example a study was made on the *"Effects of pressure on fuel-rich combustion of methane-air under high pressure"* [11], in this work was proposed a new and innovate gas turbine system that could improve the thermal efficiency more than 10% compared to conventional gas turbines; in the end it was found from the experiences that

- Stable combustion could be attained with equivalence ratios in the range $\phi = 0.7 - 1.3$ at 4 MPa in pressure;
- There was little effect of pressure on the components of combustion gases;
- Flammability limit extended with increasing the pressure in the fuel-rich region while it was constant in the fuel-lean one;
- The NO_x emissions decreased with an increase in the pressure under the fuel-rich condition.

In the last years studies regarding the use of methane as fuel have been made as it can be seen in Table 3, studies that will also be explained in more detail.

Table 3 – Some studies regarding the use of methane as fuel.

Studies Regarding the Use of Methane as Fuel

Title	Authors	Published Year
"Technology of methane combustion on granulated catalysts for environmentally friendly gas turbine power plants"	Zinfer R. Ismagilov, Nadezhda V. Shikina, Svetlana A. Yashnik, Andrei N. Zagoruiko, Mikhail A. Kerzhentsev, Vladimir A. Ushakov, Vladimir A. Sazonov, Valentin N. Parmon, Vladimir M. Zakharov, Boris I. Braynin, Oleg N. Favorski	2010
"Thermodynamic characteristics of a low concentration methane catalytic combustion gas turbine"	Juan Yin, Shi Su, Xin Xiang Yu, Yiwu Weng	2010
"Methane catalytic combustion under pressure"	A. Di Benedetto, G. Landi, V. Di Sarli, P.S. Barbato, R. Pirone, G. Russo	2012
"Study of Lean Premixed Methane Combustion with CO_2 Dilution under Gas Turbine Conditions"	Stéphanie de Persis, Gilles Cabot, Laure Pillier, Iskender Gökalp, and Abdelakrim Mourad Boukhalfa	2013

The work of Z.R. Ismagilov et al. [12] published in the journal *Catalysis Today* developed and investigated the combustion of methane in small gas turbine catalytic combustors on granulated catalysts with low content of noble metals. The catalytic combustion of natural gas over uniform and combined loadings of granulated manganese-oxide and palladium-containing catalysts was studied for optimization of the design of catalytic package for use in catalytic combustion chamber (CCC), showing the catalysts based on manganese-hexaaluminate high efficiency and thermal stability during combustion of natural gas. Also a combined catalyst package including a $40\ \mathrm{mm}$ layer of an active palladium-ceria catalyst located at the CCC entrance before the main catalyst layer was shown to be efficient for natural gas combustion with similar emission characteristics and low inlet temperature.

Also in 2010 in the journal *Applied Energy* J. Yin et al. hand out the research *"Thermodynamic characteristics of a low concentration methane catalytic combustion gas turbine"* [13] this paper presents the results of the thermodynamic characteristics of a new lean burn catalytic combustion gas turbine system (a VAMCAT), powered with about 1% methane in the air by conducting performance analyses of the turbine cycle. The performance including thermal, and exergy efficiencies and exergy loss of main components

of the turbine system was analyzed under different conditions being determined that the optimal pressure ratio to be 2.4, and the maximal efficiency 29.81%. A VAMCAT system schematic diagram can be seen in Figure 5.

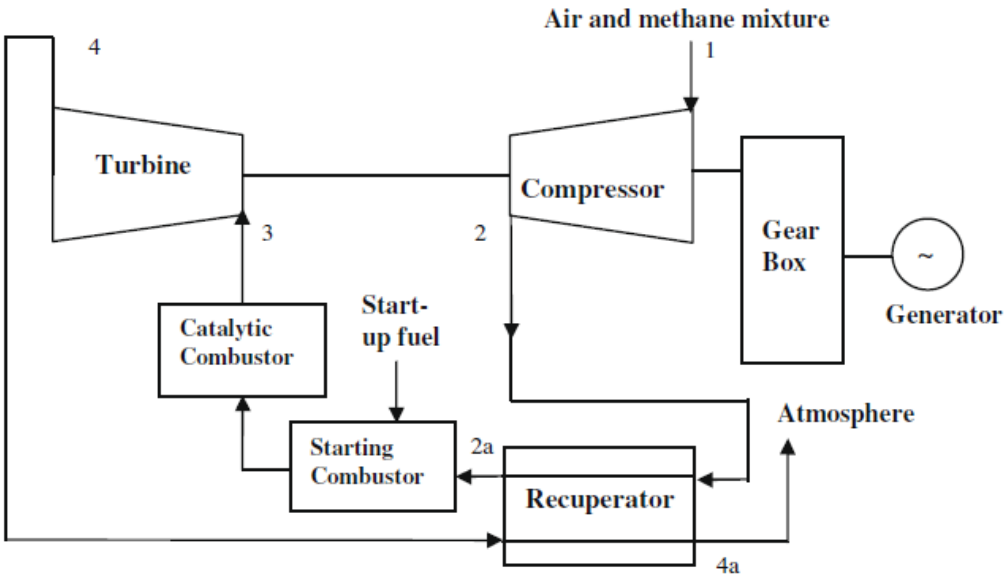

Figure 5 - A schematic diagram of the VAMCAT system [13].

In the year 2012 it can be mentioned the paper *"Methane catalytic combustion under pressure"* of A. Di Benedetto et al. [14] and in 2013 the article *"Study of Lean Premixed Methane Combustion with CO_2 Dilution under Gas Turbine Conditions"* of Stéphanie de Persis et al. [15].

The first one centers on the thermal management of a monolithic reactor for catalytic combustion of methane at pressure relevant to gas turbine applications. The role of operating pressure on methane conversion, temperature profiles, and relevance of homogeneous reaction with respect to heterogeneous reaction was investigated both experimentally and numerically, achieving the conclusions that the effect of pressure is to decrease the mass transfer from the bulk to the catalyst, thus preventing the complete methane conversion. However, this effect is counter-balanced by the activation of homogeneous reaction which is favored by increasing pressure. The interaction between these two counteracting effects allowed the identification of an optimal reactor configuration.

The second one, the study of lean premixed methane combustion with CO_2 dilution in gas turbine conditions was carried out through an experimental approach performed in a model gas turbine chamber coupled to a kinetic approach. Modeling was carried out in order to simulate the combustion conditions in terms of burning velocity, temperature, and pollutant emissions required for proper operation of the system. This work was a first approach to the study of the dry EGR effect, showing that CO_2 dilution could be an effective technique for augmenting CO_2 concentration in exhaust gas, thus making its apprehension simpler.

Table 4 - Some studies regarding the use of hydrogen as fuel.

Studies Regarding the Use of Hydrogen as Fuel

Title	Authors	Published Year
"Reduction of a detailed reaction mechanism for hydrogen combustion under gas turbine conditions"	Jochen Ströhle, Tore Myhrvold	2006
"NO_x reduction and NO_2 emission characteristics in rich-lean combustion of hydrogen"	Toshio Shudo, Kento Omori, Osamu Hiyama	2008
"Flameless combustion for hydrogen containing fuels"	Yu Yu, Wang Gaofeng, Lin Qizhao, Ma Chengbiao, Xing Xianjun	2010
"Gas turbine combustion performance test of hydrogen and carbon monoxide synthetic gas"	Min Chul Lee, Seok Bin Seo, Jae Hwa Chung, Si Moon Kim, Yong Jin Joo, Dal Hong Ahn	2010
"Numerical simulation of a hydrogen fuelled gas turbine combustor"	Paolo Gobbato, Massimo Masi, Andrea Toffolo, Andrea Lazzaretto	2010
"The effects and characteristics of hydrogen in SNG on gas turbine combustion using a diffusion type combustor"	Seik Park, Uisik Kim, Minchul Lee, Sungchul Kim, Dongjin Cha	2013

In Table 4 are exhibited some studies of the former years in which there is the employment of hydrogen as fuel; following their outcomes will be explained.

Even though these are very actual researches, an example of an earlier work can be given to prove that this subject is being studied for quite some time.

It can be mentioned the research paper of N. Kobayashi et al. *"Fuel-Rich Hydrogen-Air Combustion for a Gas-Turbine System without CO_2 Emission"* [16] published in 1997 wherein is suggested a new and innovative gas turbine system using fuel-rich hydrogen combustion, where it was established that flames under no-swirling conditions were underventilated and long in the axial direction; with swirl the flames spread in the radial direction and were greatly shortened, also the $\mathrm{NO_x}$ emission depended strongly on the equivalence ratio and swirl, (swirl was effective in reducing $\mathrm{NO_x}$ emission). These results insinuate that swirling flames may allow size reductions of combustors while significantly suppressing $\mathrm{NO_x}$ emissions.

The study of J. Ströhle, T. Myhrvold [17] purpose was to find a reduced mechanism that accurately represents chemical kinetics for lean hydrogen combustion at elevated pressures, as present in a typical gas turbine combustor. Several reduced mechanisms were tested under conditions of a typical lean premixed gas turbine combustor, i.e. $\mathrm{H_2/air}$ mixtures at $\phi = 0.5$,

17 bar, and 609 K, in which the main results were that in a freely propagating laminar flame, OH is the radical with the highest concentrations; for the process of extinction in a perfectly stirred reactor (PSR), the H radical is the dominating radical, followed by OH and O; in autoignition calculations, H, O, and OH are also the radicals with the highest concentrations; the present investigations show that at least 11 elementary reactions are necessary for satisfactory prediction of the processes of ignition, extinction, and laminar flame propagation under gas turbine conditions.

The paper of T. Shudo et al. [18] focus on a subject that is very important regarding the environment once that the nitrogen oxides are very toxic. This study focused on experimental measurements of NO and NO_2 emissions from a coaxial rich-lean burner (see Figure 6) fueled with hydrogen, being the results compared with diffusion combustion and methane rich-lean combustion. The obtained results can be concise as; (1) NO_x emissions from hydrogen combustion can be reduced by the rich-lean combustion in a coaxial burner as compared with diffusion combustion; (2) NO_x reduction effect is larger in the rich-lean combustion of hydrogen than that of methane; (3) NO_2/NO_x emission fractions are lower in the rich-lean combustion of hydrogen than in that of methane; (4) hydrogen is a suitable fuel to reduce both NO and NO_2 by rich-lean combustion, because of the zero emission of the prompt NO and the lower NO_2 emission.

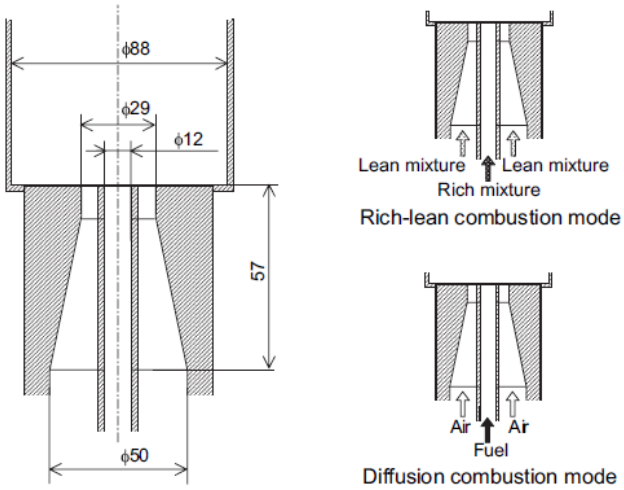

Figure 6 - Coaxial rich-lean burner used in the experiments [18].

The Y. Yu et al. work *"Flameless combustion for hydrogen containing fuels"* [19] used a PSRN model to formulate the flameless combustion in the air of four fuels: H_2/CH_4 60%/40% (by volume), H_2/CH_4 40%/60%, H_2/CH_4 20%/80% and pure hydrogen. The numerical outcomes were compared with experimental data, being the main conclusions of this research the follows: (1) different hydrogen containing fuels can work in the "clean flameless combustion" mode. Above the required threshold temperature and entrainment ratio, flameless combustion can be sustained; (2) for the fuels with more hydrogen contents, higher peak temperature can be obtained in the flameless combustion process. In the case, both the NO_x and CO emissions calculated by the PSRN model are similar to the experimental

data, corresponding to the clean flameless combustion mode; (3) the pollutant formations are extremely low in the flameless combustion condition for all the fuels studied. In the flameless combustion mode, the CO emission decreases by increasing the hydrogen contents in HCFs, but the NO_x emissions are not sensitive to the hydrogen composition of the HCFs when the furnace temperature and dilution are kept constant; (4) further analysis reveals that in the highly diluted case, the NO_x and CO emissions do not depend on the entrainment ratio.

In 2009 an experimental study was conducted by M. C. Lee et al. [20] on the GE 7EA gas turbine, in order to study the combustion performance of synthetic gas, which was composed essentially of hydrogen and carbon monoxide, being the results compared with the ones of methane combustion.

After conducting the combustion tests of syngas and methane, the following conclusions were acquired

- The combustion characteristics of syngas may vary with respect to the ratio of hydrogen to carbon monoxide. A fuel with high hydrogen content emits more NO_x, but does not emit CO even in a low load condition;
- Synthetic gas does not generate combustion pulsation, unlike methane;
- It is supposed that synthetic gas composed of hydrogen and carbon monoxide with nitrogen or steam diluents could be applied to the GE 7EA gas turbine with only a small modification, and that it would ensure clean and stable operation upon its application.

In the Department of Mechanical Engineering of the University of Padova (Italy) the investigators P. Gobbato et al. made a *"Numerical simulation of a hydrogen fuelled gas turbine combustor"* [21]. A sketch of the GE-10 combustor can be observed in Figure 7.

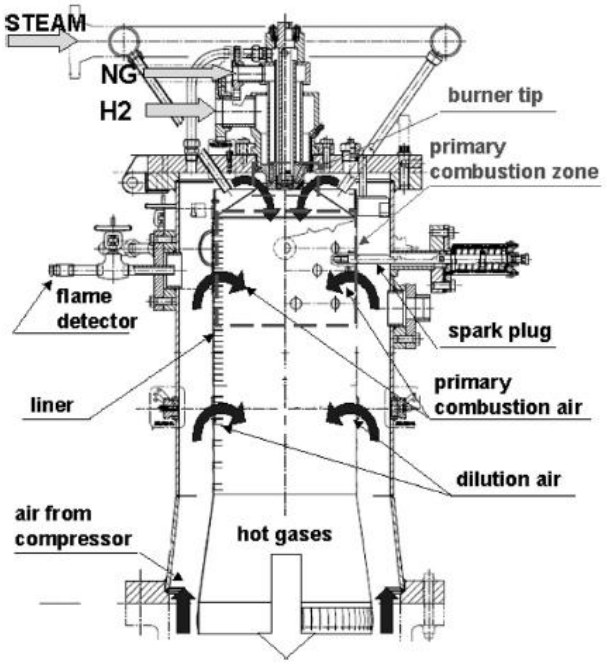

Figure 7 - Sketch of a longitudinal section of the combustor [21].

The analyzed configuration was tested with pure hydrogen fuelling to evaluate the reliability of the components designed for natural gas operation. The research goal was to evaluate the capability of a rather basic CFD approach to predict the temperature field inside the combustor. Liner wall temperatures and turbine inlet temperatures measured during full scale full pressure experimental tests were used to validate the numerical results.

It was found a close match between CFD profiles and experimental data at the combustor discharge in terms of non-dimensional values, the calculated thermal field was useful to explain the non-uniform distribution of the temperature measured at the turbine inlet. The hot zone in the upper part of the combustor discharge is due to the high temperature axial stream leaving the core of the liner which does not distribute regularly on the outlet section.

According to the obtained results, it can be said that the CFD approach can be employ to make a preliminary selection among new combustor configurations in spite of the basic features of the numerical models.

Last year, in 2013 in the Republic of Korea a joint work between the Korea Electric Power Research Institute and the Building and Plant Engineering Department of the Hanbat National University studied *"The effects and characteristics of hydrogen in SNG on gas turbine combustion using a diffusion type combustor"* [22]. Three kinds of SNG with different H_2 content ranging from 0% volume up to 3% were used for the combustion tests in a GE 7EA model combustor (see Figure 8), and a macro flame image was taken to analyze the effect of hydrogen content on the combustion characteristics at ambient pressure conditions and the pattern factor of each fuel was examined at higher pressure combustion conditions.

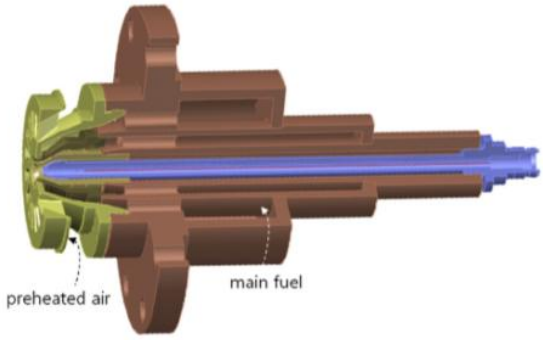

Figure 8 - A cutaway view of the model combustor GE 7EA [22].

In the end the following results were achieved:

- The higher reaction activity of hydrogen shortened and widened the flame at the same load. As the hydrogen content increased to 3% volume, the flame length decreased by 3.2% and the flame angle increased by 4.2%.
- As the slanted flame of the combustor liner due to the hydrogen content in SNG can be a source of thermal damage to a gas turbine combustor, the gas turbine combustor should be tuned when a higher hydrogen SNG fuel is used for gas turbines.

- The NO_x emission and the combustion efficiencies of three kinds of SNG with different hydrogen content were almost identical at the same load.
- Due to a similarity in real gas turbine combustor conditions for power generation, the high pressure combustion test helped verify the ambient pressure combustion tests conducted to determine the effect of hydrogen in SNG. The evaluated pattern factors using different types of SNG in the gas turbine combustion test rig were almost identical.

Finally is important to mention that similar work to this dissertation has been made, as the ones expressed in Table 5.

Table 5 – Similar studies to the current dissertation.

Similar Studies

Title	Authors	Published Year
"Investigation of a Gas Turbine Combustion System Fired with Mixtures of Natural Gas and Hydrogen"	H-J Tomczak, G Benelli, L Carrai and D Cecchini	2002
"Emissions reduction benefits from hydrogen addition to midsize gas turbine feedstocks"	C.Y. TerMaath, E.G. Skolnik, R.W. Schefer, J.O. Keller	2006
"Hydrogen injection as additional fuel in gas turbine combustor. Evaluation of effects"	G.L. Juste	2006
"Hydrogen addition effects on methane-air colorless distributed combustion flames"	Vaibhav K. Arghode, Ashwani K. Gupta	2011
"The effect of hydrogen addition on combustion and emission characteristics of an n-heptane fuelled HCCI engine"	Hongsheng Guo, W. Stuart Neill	2013
"A computational study on the combustion of hydrogen/methane blended fuels for a micro gas turbines"	Hsin-Yi Shih, Chi-Rong Liu	2014

For each study shown above (Table 5) the subsequent results and conclusions were reached.

The study made by Tomczak, Benelli, Carrai and Cecchini in 2002 *"Investigation of a Gas Turbine Combustion System Fired with Mixtures of Natural Gas and Hydrogen"* [23] was both numerical and experimental, the numerical one was carried through a CFD simulation using FLUENT and the experimental investigation took place in a Gas Turbine Test Facility located in Italy, the *ENEL Facility Sesta*.

The investigated combustion chamber is coupled with a diffusion flame type gas turbine; the combustor is a typical reverse-flow multi-can combustion system (see Figure 9) similar to most of the GE heavy-duty gas turbines.

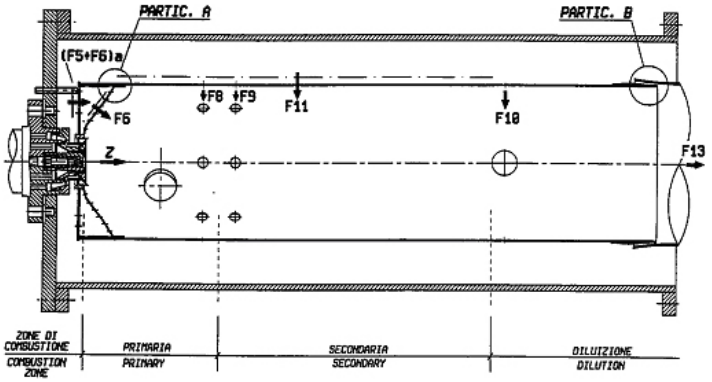

Figure 9 – Reverse-flow combustion system [23].

As fuel, different natural gas – hydrogen mixtures were used, as described below

- 100% Natural Gas – 0% Hydrogen;
- 75% Natural Gas – 25% Hydrogen;
- 50% Natural Gas – 50% Hydrogen;
- 25% Natural Gas – 75% Hydrogen;
- 0% Natural Gas – 100% Hydrogen.

In the end both numerical and experimental results have confirmed the general thermodynamic aspects from the technical literature of hydrogen flame features. Its better flame stability has been confirmed as well as the tendencies of NO_x and CO pollutant emission, without any modification of a traditional gas turbine combustion system, hydrogen rich mixtures, until pure hydrogen have been successfully used as an alternative fuel.

Nevertheless the high NO_x emission measured at the combustor outlet using pure hydrogen (up to 3.4 times greater than using natural gas) forces the design combustion systems that includes NO_x emission reduction techniques.

A joint work in the USA between the *Energetics, Inc.* and the *Combustion Research Facility, Sandia National Laboratories*, investigated the benefits from the addition of hydrogen to midsize gas turbine feedstocks [24]. A cost analysis of hydrogen addition as a method of reducing nitrogen oxide emissions from midsize gas turbines was performed. Comparisons were made with current NO_x control technologies that included both dry low NO_x (DLN) combustors and selective catalytic reduction (SCR). The results showed that up to 15% hydrogen addition is cost competitive with current control technologies and, in some cases such as high temperature SRC, could be cheaper. Although over 20% hydrogen addition is somewhat more expensive, several advantages are provided over SRC. These advantages include achievable NO_x emissions of $1\ \text{ppm}$ with $30-40\%$ hydrogen addition, the fact that no ammonia or catalyst is needed, and that hydrogen addition also reduces carbon dioxide emissions.

G. L. Juste made a research to evaluate the effects of hydrogen injection as an additional fuel in a gas turbine combustor to reduce the pollutants emissions [25]. For that it was made an experimental study in the combustion chamber, exposed in Figure 10, of a conventional tubular type.

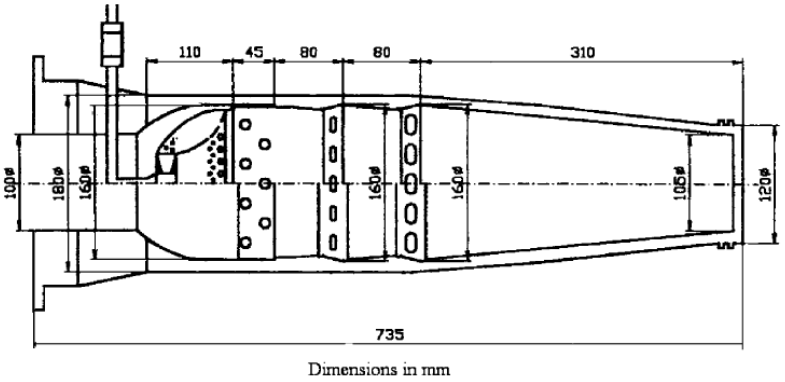

Figure 10 - Gas turbine combustor [25].

In the end the subsequent results were accomplished

- At full load conditions, leaning the primary zone of combustion chamber, increasing the primary air, is an efficient meant to reduce NO_x emissions, but at a cost of decreasing efficiency, because CO and HC emissions increase;
- Injecting small quantities of hydrogen, until 4%, to lean primary zones, the EI_{CO} can be reduced a 30%, without a relevant increase in NO_x;
- The CO reduction is partially due to hydrocarbon substitution and mainly to chemical kinetics;
- Addition of small quantities of hydrogen contributes substantially to the reduction of the emissions of CO_2 by substitution effect;
- As the heating value of the hydrogen is higher than that of fossil fuel, if it is hold the same energy contribution to combustion chamber, the decrease in hydrocarbon weight, and therefore of the CO_2 emissions, is very important.

More recent in 2011 the paper *"Hydrogen addition effects on methane-air colorless distributed combustion flames"* [26] was available in the international journal *Hydrogen Energy*. This work main goal was to investigate for the CDC flames, the role of hydrogen addition in a reverse flow configuration, consisting of both non-premixed and premixed combustion modes.

Development of CDC for gas turbine applications requires careful examination on the role of various input and operational parameters for ultra-low NO_x, CO, UHC emissions, stable combustion and higher efficiency. Reverse flow geometry including a premixed mode and a non-premixed mode was examined for the role of hydrogen addition to methane fuel. Numerical simulations suggest that significant recirculation of gases was present and maximum recirculation was limited due to the confinement. Residence time calculation suggests that CDC combustor can result in lower CO emissions as compared to perfectly

stirred reactor case. Experimental studies show ultra-low NO emissions for both non-premixed and premixed mode. CO emissions in both premixed and non-premixed cases were lower as compared to the calculated values for perfectly stirred reactor. Addition of hydrogen to methane resulted in increase in NO emissions in the non-premixed case. CO emissions decreased with addition of hydrogen for both premixed and non-premixed modes. Addition of hydrogen extended lean operational limits of the CDC combustor.

From the *Energy, Mining and Environment Portfolio*, National Research Council Canada came the work of H. Guo et al. about *"The effect of hydrogen addition on combustion and emission characteristics of an n-heptane fuelled HCCI engine"* [27] were an HCCI engine (the studied engine is a Cooperative Fuel Research) was numerically investigated using a multi-zone model, and the results compared with previous experimental data.

- Both experiment and calculation show that hydrogen addition retards combustion phasing of an n-heptane fuelled HCCI engine. The analysis of the detailed numerical results indicates that the combustion phasing retardation by hydrogen addition is due to both dilution and chemical effects, with dilution effect being more significant;
- At a constant compression ratio, combustion duration is also reduced if an appropriate amount of hydrogen is added;
- When an appropriate amount of hydrogen is added, indicated thermal efficiency increases at a constant compression ratio due to the optimization of combustion phasing. However, unless the combustion phasing is overly advanced, hydrogen addition always improves indicated thermal efficiency at a constant combustion phasing owing to the optimized combustion phasing and the higher compression ratio used;
- Hydrogen addition reduces indicated specific unburned hydrocarbon emissions, but slightly increases unburned hydrocarbon emissions per unit burned n-heptane mass;
- The numerical simulation result also shows that N_2O emissions may increase with overly retarding combustion phasing at a constant fraction of hydrogen, but hydrogen addition can moderate this increase in N_2O emissions.

The most recent paper discussed here is the 2014 Hsin-Yi Shih et al. study about *"A computational study on the combustion of hydrogen/methane blended fuels for a micro gas turbines"* [28].

The can type combustor (see Figure 11) has been modeled and the effects of hydrogen content in the methane/hydrogen blended fuels on combustion performance were studied and characterized. In order to understand the potential applications of hydrogen fuels for the innovative micro gas turbine, the numerical simulations were conducted with $0\% - 90\%$ volumetric fraction of hydrogen in the blended fuels. Flame structures were compared and the combustion performance including the average flame temperature in the primary zone, exit temperature of the combustor, pattern factor and emissions were analyzed with the modeling results.

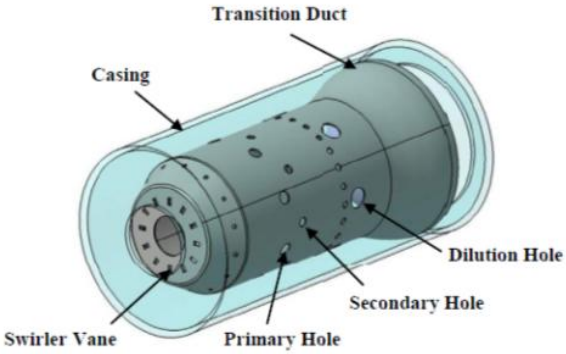

Figure 11 - The modeled can combustor [28].

As hydrogen is substituted for methane at a fixed fuel injection velocity, the flame temperatures become higher, but lower fuel flow rate and heat input at higher hydrogen substitution percentages cause a power shortage.

To apply the blended fuels at a constant fuel flow rate, the flame temperatures are increased with increasing hydrogen percentages. This will benefit the performance of gas turbine, but the cooling and the NO_x emissions are the primary concerns. While fixing a certain heat input to the engine with blended fuels, wider but shorter flames at higher hydrogen percentages are found, but the substantial increase of CO emission indicates a decrease in combustion efficiency. The NO_x emission decreases quickly at higher hydrogen content.

The simulated results demonstrated the ability to reach good combustion performance at moderate hydrogen fractions. Although further experimental testing and the performance measurements of the combustor are still needed to employ the blended fuels for the micro gas turbine, the model simulation is an important step to understand the combustion characteristics and optimum design of the combustor with hydrogen addition.

Chapter 3

Fundamental Equations

3.1 Governing Equations

The transport equations that describe the unsteady flow for reacting flow are conservation of mass, species mass, momentum and energy.

3.1.1 Conservation of Mass

The equation for conservation of mass, or continuity equation, can be written as follow:

$$\frac{\partial \rho}{\partial t} + \nabla \cdot (\rho \vec{v}) = S_m \qquad (1)$$

Equation (1) is the general form of the mass conservation equation and is valid for incompressible as well as compressible flows. The source S_m is the mass added to the continuous phase from the dispersed second phase and any user-defined sources [29].

3.1.2 Conservation of Species Mass

For a system containing one phase but more than one component, the total mass of the system is composed of different species. If the concentrations of each of these species are not uniform, mass transfer occurs in a way that makes the concentrations more uniform. Therefore, it is necessary to track the individual components by applying the principle of conservation of species mass. The conservation of species mass that contains only one phase is [30]:

$$\frac{\partial}{\partial t}\int_V \rho_i dV + \int_A \rho_i (V_{rel} \cdot n) dA = -\int_A J_i \cdot n dA + \int_V \dot{m}_i''' dV \qquad (2)$$

3.1.3 Conservation of Momentum

Conservation of momentum in an inertial (non-accelerating) reference frame is described by [31].

$$\frac{\partial}{\partial t}(\rho \vec{v}) + \nabla \cdot (\rho \vec{v}\vec{v}) = -\nabla p + \nabla \cdot \left(\bar{\bar{\tau}}\right) + \rho \vec{g} + \vec{F} \qquad (3)$$

Where ρ is the static pressure, $\bar{\bar{\tau}}$ is the stress tensor (defined beneath), and $\rho\vec{g}$ and $\vec{F}$ are the gravitational body force and external body forces, respectively. $\vec{F}$ also contains other model-dependent source terms such as porous-media and user-defined sources.

The stress tensor is given by:

$$\bar{\bar{\tau}} = \mu\left[(\nabla\vec{v} + \nabla\vec{v}^T) - \frac{2}{3}\nabla\cdot\vec{v}I\right] \quad (4)$$

Where μ is the molecular viscosity, I is the unit tensor, and the second term on the right hand side is the effect of volume dilation [29].

3.1.4 Conservation of Energy

Conservation of energy is described by [29]:

$$\frac{\partial}{\partial t}(\rho E) + \nabla\cdot\left(\vec{v}(\rho E + p)\right) = -\nabla\cdot\left(\sum_j h_j J_j\right) + S_h \quad (5)$$

3.2 Reynolds Averaged Navier-Stokes (RANS) Turbulence

RANS models offer the most economic approach for computing complex turbulent industrial flows. Typical examples of such models are the $k-\varepsilon$ or the $k-\omega$ models in their different forms. These models simplify the problem to the solution of two additional transport equations and introduce an Eddy-Viscosity (turbulent viscosity) to compute the Reynolds Stresses [29].

3.2.1 Reynolds Averaged Equations

The equations governing viscous incompressible flow, whether turbulent or laminar, are

$$\partial_t\tilde{u}_i + \tilde{u}_j\partial_j\tilde{u}_i = -\frac{1}{\rho}\partial_i\tilde{p} + \nu\nabla^2\tilde{u}_i, \qquad \partial_i\tilde{u}_i = 0 \quad (6)$$

The first expresses conservation of momentum. The second expresses the incompressibility of fluid volumes, which is equivalent to mass conservation in the present case.

The Navier–Stokes equations, Equations (6) govern fluid turbulence. The snag is that the phenomenon of turbulence is the complete solution to these equations – a chaotic, spatially, and temporally complex solution. Such solutions are not easily obtained. A much simpler level of description is needed: this call for a statistical approach. There are no closed equations for the statistics of turbulent flow. The equations obtained by averaging the exact laws (6) contain more unknowns than the number of equations [32].

The total velocity is decomposed into a sum of its mean and a fluctuation, $\tilde{\boldsymbol{u}}(\boldsymbol{x},\boldsymbol{t}) = \boldsymbol{U}(\boldsymbol{x}.\boldsymbol{t}) + \boldsymbol{u}(\boldsymbol{x}.\boldsymbol{t})$, where $\boldsymbol{U} \equiv \bar{\tilde{\boldsymbol{u}}}$. If this decomposition is substituted into Equation (6) they become

$$\boldsymbol{\partial_t}(\boldsymbol{U_i} + \boldsymbol{u_i}) + (\boldsymbol{U_j} + \boldsymbol{u_j})\boldsymbol{\partial_j}(\boldsymbol{U_i} + \boldsymbol{u_i}) = -\frac{\boldsymbol{1}}{\boldsymbol{\rho}}\boldsymbol{\partial_i}(\boldsymbol{P} + \boldsymbol{p}) + \boldsymbol{\nu}\boldsymbol{\nabla^2}(\boldsymbol{U_i} + \boldsymbol{u_i}),$$
$$\boldsymbol{\partial_i}(\boldsymbol{U_i} + \boldsymbol{u_i}) = \boldsymbol{0} \qquad \textbf{(7)}$$

The average of these equations is obtained by drawing a bar over each term, noting the rules $\overline{\boldsymbol{U}} = \boldsymbol{U}$ and $\overline{\boldsymbol{u}} = \boldsymbol{0}$:

$$\boldsymbol{\partial_t U_i} + \boldsymbol{U_j}\boldsymbol{\partial_j U_i} = -\frac{\boldsymbol{1}}{\boldsymbol{\rho}}\boldsymbol{\partial_i P} + \boldsymbol{\nu}\boldsymbol{\nabla^2 U_i} - \boldsymbol{\partial_j}\overline{\boldsymbol{u_j u_i}}, \qquad \textbf{(8)}$$
$$\boldsymbol{\partial_i U_i} = \boldsymbol{0}$$

These are the Reynolds averaged Navier–Stokes (RANS) equations. Equations (8) for the mean velocity are the same as Equations (6) for the total instantaneous velocity, except for the last term of the momentum equation, $-\boldsymbol{\partial_j}\overline{\boldsymbol{u_j u_i}}$. This term is a derivative of the Reynolds stress tensor.

3.3 $k - \varepsilon$ Model

The $k - \varepsilon$ model is the most widely used general-purpose turbulence transport model. The current form was initially developed by Jones and Launder [33].

3.3.1 Standard $k - \varepsilon$ Model

What is now called the "standard" $k - \varepsilon$ model is the Jones–Launder form, without wall damping functions, and with the empirical constants given by Launder and Sharma [34].

3.3.1.1 Transport Equations for the Standard $k - \varepsilon$ Model

The turbulence kinetic energy, k, and its rate of dissipation, ε, are obtained from the following transport equations:

$$\frac{\partial}{\partial t}(\rho k) + \frac{\partial}{\partial x_i}(\rho k u_i) = \frac{\partial}{\partial x_j}\left[\left(\mu + \frac{\mu_t}{\sigma_k}\right)\frac{\partial k}{\partial x_j}\right] + G_k + G_b - \rho\varepsilon - Y_M + S_k \qquad \textbf{(9)}$$

and

$$\frac{\partial}{\partial t}(\rho \varepsilon) + \frac{\partial}{\partial x_i}(\rho \varepsilon u_i) = \frac{\partial}{\partial x_j}\left[\left(\mu + \frac{\mu_t}{\sigma_\varepsilon}\right)\frac{\partial \varepsilon}{\partial x_j}\right] + C_{1\varepsilon}\frac{\varepsilon}{k}(G_k + C_{3\varepsilon}G_b) - C_{2\varepsilon}\rho\frac{\varepsilon^2}{k} + S_\varepsilon \qquad \textbf{(10)}$$

In these equations, G_k represents the generation of turbulence kinetic energy due to the mean velocity gradients. G_b is the generation of turbulence kinetic energy due to buoyancy. Y_M represents the contribution of the fluctuating dilatation in compressible turbulence to the overall dissipation rate. $C_{1\varepsilon}$, $C_{2\varepsilon}$, and $C_{3\varepsilon}$ are constants. σ_k and σ_ε are the

turbulent Prandtl numbers for k and ε, respectively. S_k and S_ε are user-defined source terms [29].

3.3.1.2 Modeling the Turbulent Viscosity

The turbulent (or eddy) viscosity, μ_t, is computed by combining k and ε as follows:

$$\mu_t = \rho C_\mu \frac{k^2}{\varepsilon} \quad (11)$$

where C_μ is a constant.

3.3.1.3 Model Constants

The model constants $C_{1\varepsilon}$, $C_{2\varepsilon}$, C_μ, σ_k and σ_ε have the following default values [35]: $C_{1\varepsilon}$=1.44, $C_{2\varepsilon} = 1.92$, $C_\mu = 0.09$, $\sigma_k = 1.0$ and $\sigma_\varepsilon = 1.3$

3.3.2 RNG $k - \varepsilon$ Model

The RNG $k - \varepsilon$ model was derived using a statistical technique called renormalization group theory. It is similar in form to the standard $k - \varepsilon$ model, but includes the following refinements [29]:

- The RNG model has an additional term in its ε equation that improves the accuracy for rapidly strained flows.
- The effect of swirl on turbulence is included in the RNG model, enhancing accuracy for swirling flows.
- The RNG theory provides an analytical formula for turbulent Prandtl numbers, while the standard $k - \varepsilon$ model uses user-specified, constant values.
- While the standard $k - \varepsilon$ model is a high-Reynolds number model, the RNG theory provides an analytically-derived differential formula for effective viscosity that accounts for low-Reynolds number effects. Effective use of this feature does, however, depend on an appropriate treatment of the near-wall region

These features make the RNG $k - \varepsilon$ model more accurate and reliable for a wider class of flows than the standard $k - \varepsilon$ model.

The RNG-based $k - \varepsilon$ turbulence model is derived from the instantaneous Navier-Stokes equations, using a mathematical technique called “renormalization group” (RNG) methods. The analytical derivation results in a model with constants different from those in the standard $k - \varepsilon$ model, and additional terms and functions in the transport equations for k and ε.

3.3.2.1 Transport Equations for the RNG $k - \varepsilon$ Model

The RNG k – ε model has a similar form to the standard $k - \varepsilon$ model:

$$\frac{\partial}{\partial t}(\rho k) + \frac{\partial}{\partial x_i}(\rho k u_i) = \frac{\partial}{\partial x_j}\left(\alpha_k \mu_{eff} \frac{\partial k}{\partial x_j}\right) + G_k + G_b - \rho\varepsilon - Y_M + S_k \quad (12)$$

and

$$\frac{\partial}{\partial t}(\rho \varepsilon) + \frac{\partial}{\partial x_i}(\rho \varepsilon u_i) = \frac{\partial}{\partial x_j}\left(\alpha_\varepsilon \mu_{eff} \frac{\partial \varepsilon}{\partial x_j}\right) + C_{1\varepsilon}\frac{\varepsilon}{k}(G_k + C_{3\varepsilon}G_b) - C_{2\varepsilon}\rho\frac{\varepsilon^2}{k} - R_\varepsilon + S_\varepsilon \quad (13)$$

In these equations, G_k represents the generation of turbulence kinetic energy due to the mean velocity gradients. G_b is the generation of turbulence kinetic energy due to buoyancy. Y_M represents the contribution of the fluctuating dilatation in compressible turbulence to the overall dissipation rate. The quantities α_k and α_ε are the inverse effective Prandtl numbers for k and ε, respectively. S_k and S_ε are user-defined source terms.

3.3.2.2 Modeling the Effective Viscosity

The scale elimination procedure in RNG theory results in a differential equation for turbulent viscosity:

$$d\left(\frac{\rho^2 k}{\sqrt{\varepsilon\mu}}\right) = 1.72\frac{\hat{\nu}}{\sqrt{\hat{\nu}^3 - 1 + C_\nu}}d\hat{\nu} \quad (14)$$

where

$\hat{\nu} = \frac{\mu_{eff}}{\mu}$

$C_\nu \approx 100$

Equation (14) is integrated to obtain an accurate description of how the effective turbulent transport varies with the effective Reynolds number (or eddy scale), allowing the model to better handle low-Reynolds number and near-wall flows.

In the high-Reynolds number limit, Equation (14) gives

$$\mu_t = \rho C_\mu \frac{k^2}{\varepsilon} \quad (15)$$

with $C_\mu = 0.0845$, derived using RNG theory [29].

3.3.2.3 Model Constants

The model constants $C_{1\varepsilon}$ and $C_{2\varepsilon}$ in Equation (13) have values derived analytically by the RNG theory. These values are $C_{1\varepsilon} = 1.42$ and $C_{2\varepsilon} = 1.68$ [29].

3.3.3 Realizable $k - \varepsilon$ Model

The realizable $k - \varepsilon$ model [36] differs from the standard $k - \varepsilon$ model in two important ways [29]:

- The realizable $k - \varepsilon$ model contains an alternative formulation for the turbulent viscosity.
- A modified transport equation for the dissipation rate, ε, has been derived from an exact equation for the transport of the mean-square vorticity fluctuation.

The term "realizable" means that the model satisfies certain mathematical constraints on the Reynolds stresses, consistent with the physics of turbulent flows. Neither the standard $k - \varepsilon$ model nor the RNG $k - \varepsilon$ model is realizable.

To understand the mathematics behind the realizable $k - \varepsilon$ model, consider combining the Boussinesq relationship and the eddy viscosity definition to obtain the following expression for the normal Reynolds stress in an incompressible strained mean flow:

$$\overline{u^2} = \frac{2}{3}k - 2\nu_t \frac{\partial U}{\partial x} \qquad (16)$$

Using Equation (15) for $\nu_t \equiv \mu_t/\rho$, one obtains the result that the normal stress, $\overline{u^2}$, which by definition is a positive quantity, becomes negative, that is, "non-realizable", when the strain is large enough to satisfy

$$\frac{k}{\varepsilon}\frac{\partial U}{\partial x} > \frac{1}{3C_\mu} \approx 3.7 \qquad (17)$$

Similarly, it can also be shown that the Schwarz inequality for shear stresses ($\overline{\mu_\alpha \mu_\beta}^2 \leq \overline{\mu_\alpha^2 \mu_\beta^2}$; no summation over α and β) can be violated when the mean strain rate is large. The most straightforward way to ensure the realizability (positivity of normal stresses and Schwarz inequality for shear stresses) is to make C_μ variable by sensitizing it to the mean flow (mean deformation) and the turbulence (k, ε). The notion of variable C_μ is suggested by many modelers including Reynolds [37], and is well substantiated by experimental evidence.

Both the realizable and RNG $k-\varepsilon$ models have shown substantial improvements over the standard $k-\varepsilon$ model where the flow features include strong streamline curvature, vortices, and rotation. Since the model is still relatively new, it is not clear in exactly which instances the realizable $k-\varepsilon$ model consistently outperforms the RNG model. However, initial studies have shown that the realizable model provides the best performance of all the $k-\varepsilon$ model versions for several validations of separated flows and flows with complex secondary flow features.

One of the weaknesses of the standard $k-\varepsilon$ model or other traditional $k-\varepsilon$ models lies with the modeled equation for the dissipation rate (ε). The well-known round-jet anomaly is considered to be mainly due to the modeled dissipation equation.

The realizable $k-\varepsilon$ model proposed by Shih et al. [36] was intended to address these deficiencies of traditional $k-\varepsilon$ models by adopting the following:

- A new eddy-viscosity formula involving a variable C_μ originally proposed by Reynolds [37].
- A new model equation for dissipation (ε) based on the dynamic equation of the mean-square vorticity fluctuation.

One limitation of the realizable $k-\varepsilon$ model is that it produces non-physical turbulent viscosities in situations when the computational domain contains both rotating and stationary fluid zones. This is due to the fact that the realizable $k-\varepsilon$ model includes the effects of mean rotation in the definition of the turbulent viscosity. This extra rotation effect has been tested on single moving reference frame systems and showed superior behavior over the standard $k-\varepsilon$ model. However, due to the nature of this modification, its application to multiple reference frame systems should be taken with some caution.

3.3.3.1 Transport Equations for the Realizable $k-\varepsilon$ Model

The modeled transport equations for k and ε in the realizable $k-\varepsilon$ model are:

$$\frac{\partial}{\partial t}(\rho k)+\frac{\partial}{\partial x_j}(\rho k u_j)=\frac{\partial}{\partial x_j}\left[\left(\mu+\frac{\mu_t}{\sigma_k}\right)\frac{\partial k}{\partial x_j}\right]+G_k+G_b-\rho\varepsilon-Y_M+S_k \qquad (18)$$

and

$$\frac{\partial}{\partial t}(\rho\varepsilon)+\frac{\partial}{\partial x_j}(\rho\varepsilon u_j)=\frac{\partial}{\partial x_j}\left[\left(\mu+\frac{\mu_t}{\sigma_\varepsilon}\right)\frac{\partial\varepsilon}{\partial x_j}\right]+\rho C_1 S\varepsilon-\rho C_2\frac{\varepsilon^2}{k+\sqrt{\nu\varepsilon}}+C_{1\varepsilon}\frac{\varepsilon}{k}C_{3\varepsilon}G_b+S_\varepsilon \qquad (19)$$

where

$C_1=max\left[0.43,\frac{\eta}{\eta+5}\right]$, $\eta=S\frac{k}{\varepsilon}$, $S=\sqrt{2S_{ij}S_{ij}}$

In these equations, G_k represents the generation of turbulence kinetic energy due to the mean velocity gradients. G_b is the generation of turbulence kinetic energy due to buoyancy. Y_M represents the contribution of the fluctuating dilatation in compressible turbulence to the overall dissipation rate. $C_2$and $C_{1\varepsilon}$ are constants. σ_k and $\sigma_\varepsilon$re the turbulent Prandtl numbers for k and ε, respectively. S_k and S_ε are user defined source terms [29].

3.3.3.2 Modeling the Turbulent Viscosity

As in other $k-\varepsilon$ models, the eddy viscosity is computed from Equation (11).

The difference between the realizable $k-\varepsilon$ model and the standard and RNG $k-\varepsilon$ models is that C_μ is no longer constant. It is computed from

$$C_\mu=\frac{1}{A_0+A_S\frac{kU^*}{\varepsilon}} \qquad (20)$$

where

$$U^*\equiv\sqrt{S_{ij}S_{ij}+\tilde{\Omega}_{ij}\tilde{\Omega}_{ij}} \qquad (21)$$

and

$\widetilde{\boldsymbol{\Omega}}_{ij} = \boldsymbol{\Omega}_{ij} - 2\boldsymbol{\varepsilon}_{ijk}\boldsymbol{\omega}_k$

$\boldsymbol{\Omega}_{ij} = \overline{\boldsymbol{\Omega}_{ij}} - \boldsymbol{\varepsilon}_{ijk}\boldsymbol{\omega}_k$

where $\overline{\boldsymbol{\Omega}_{ij}}$ is the mean rate-of-rotation tensor viewed in a moving reference frame with the angular velocity $\boldsymbol{\omega}_k$. The model constants $\boldsymbol{A_0}$ and $\boldsymbol{A_S}$ are given by

$$\boldsymbol{A_0 = 4.04},\ \boldsymbol{A_S = \sqrt{6}cos\phi} \qquad (22)$$

where

$$\boldsymbol{\phi = \frac{1}{3}cos^{-1}(\sqrt{6}W)},\ \boldsymbol{W = \frac{S_{ij}S_{jk}S_{ki}}{\tilde{S}^3}},\ \boldsymbol{\tilde{S} = \sqrt{S_{ij}S_{ij}}},\ \boldsymbol{S_{ij} = \frac{1}{2}\left(\frac{\partial u_j}{\partial x_i} + \frac{\partial u_i}{\partial x_j}\right)} \qquad (23)$$

It can be seen that $\boldsymbol{C_\mu}$ is a function of the mean strain and rotation rates, the angular velocity of the system rotation, and the turbulence fields ($\boldsymbol{k}$ and $\boldsymbol{\varepsilon}$). $\boldsymbol{C_\mu}$ in Equation (11) can be shown to recover the standard value of 0.009 for an inertial sublayer in an equilibrium boundary layer [29].

3.3.3.3 Model Constants

The model constants $\boldsymbol{C_2}$, $\boldsymbol{\sigma_k}$ and $\boldsymbol{\sigma_\varepsilon}$ have been established to ensure that the model performs well for certain canonical flows. The model constants are $\boldsymbol{C_{1\varepsilon} = 1.44}$, $\boldsymbol{C_2 = 1.9}$, $\boldsymbol{\sigma_k = 1.0}$, $\boldsymbol{\sigma_\varepsilon = 1.2}$ [29].

3.4 $\boldsymbol{k - \omega}$ Model

Like the $\boldsymbol{k - \varepsilon}$ model discussed in the previous subsection, $\boldsymbol{k - \omega}$ model is also very popular and widely used. Over the years, this model has gone over many changes and improvements.

3.4.1 Standard $\boldsymbol{k - \omega}$ Model

The standard $\boldsymbol{k - \omega}$ model in ANSYS FLUENT is based on the Wilcox $\boldsymbol{k - \omega}$ model [38], which incorporates modifications for low-Reynolds number effects, compressibility, and shear flow spreading. One of the weak points of the Wilcox model is the sensitivity of the solutions to values for $\boldsymbol{k}$ and $\boldsymbol{\omega}$ outside the shear layer (free stream sensitivity). While the new formulation implemented in ANSYS FLUENT has reduced this dependency, it can still have a significant effect on the solution, especially for free shear flows [39].

The standard $\boldsymbol{k - \omega}$ model is an empirical model based on model transport equations for the turbulence kinetic energy ($\boldsymbol{k}$) and the specific dissipation rate ($\boldsymbol{\omega}$), which can also be thought of as the ratio of $\boldsymbol{\varepsilon}$ to $\boldsymbol{k}$ [38].

As the $\boldsymbol{k - \omega}$ model has been modified over the years, production terms have been added to both the $\boldsymbol{k}$ and $\boldsymbol{\omega}$ equations, which have improved the accuracy of the model for predicting free shear flows [29].

3.4.1.1 Transport Equations for the Standard $k-\omega$ Model

The turbulence kinetic energy, k, and the specific dissipation rate, ω, are obtained from the following transport equations:

$$\frac{\partial}{\partial t}(\rho k) + \frac{\partial}{\partial x_i}(\rho k u_i) = \frac{\partial}{\partial x_j}\left(\Gamma_k \frac{\partial k}{\partial x_j}\right) + G_k - Y_k + S_k \quad (24)$$

and

$$\frac{\partial}{\partial t}(\rho \omega) + \frac{\partial}{\partial x_i}(\rho \omega u_i) = \frac{\partial}{\partial x_j}\left(\Gamma_\omega \frac{\partial \omega}{\partial x_j}\right) + G_\omega - Y_\omega + S_\omega \quad (25)$$

In these equations, G_k represents the generation of turbulence kinetic energy due to mean velocity gradients. G_ω represents the generation of ω. Γ_k and Γ_ω represent the effective diffusivity of k and ω, respectively. Y_k and Y_ω represent the dissipation of k and ω due to turbulence. All of the above terms are calculated as described below. S_k and S_ω are user-defined source terms [29].

3.4.1.2 Modeling the Effective Diffusivity

The effective diffusivities for the $k-\omega$ model are given by

$$\Gamma_k = \mu + \frac{\mu_t}{\sigma_k}$$
$$\Gamma_\omega = \mu + \frac{\mu_t}{\sigma_\omega} \quad (26)$$

where σ_k and σ_ω are the turbulent Prandtl numbers for k and ω, respectively. The turbulent viscosity, μ_t, is computed by combining k and ω as follows:

$$\mu_t = \alpha^* \frac{\rho k}{\omega} \quad (27)$$

3.4.1.2.1 Low-Reynolds-Number Correction

The coefficient α^* damps the turbulent viscosity causing a low-Reynolds number correction. It is given by

$$\alpha^* = \alpha_0^* \left(\frac{\alpha_0^* + Re_t/R_k}{1 + Re_t/R_k}\right) \quad (28)$$

where

$$Re_t = \frac{\rho k}{\mu \omega} \quad (29)$$

$$R_k = 6 \quad (30)$$

$$\alpha_0^* = \frac{\beta_i}{3} \quad (31)$$

$$\beta_i = 0.072 \quad (32)$$

Note that in high-Reynolds number form of the $k - \omega$ model, $\alpha^* = \alpha_0^* = 1$.

3.4.1.3 Modeling the Turbulence Production

3.4.1.3.1 Production of k

The term G_k represents the production of turbulence kinetic energy. From the exact equation for the transport of k, this term may be defined as

$$G_k = -\rho\overline{u_i' u_j'}\frac{\partial u_j}{\partial x_i} \quad (33)$$

To evaluate G_k in a manner consistent with the Boussinesq hypothesis,

$$G_k = \mu_t S^2 \quad (34)$$

where S is the modulus of the mean rate-of-strain tensor, defined in the same way as for the $k - \varepsilon$ model.

3.4.1.3.2 Production of ω

The production of ω is given by

$$G_\omega = \alpha\frac{\omega}{k}G_k \quad (35)$$

where $\mathbf{G_k}$ is given by Equation (33).

The coefficient $\boldsymbol{\alpha}$ is given by

$$\alpha = \frac{\alpha_0}{\alpha^*}\left(\frac{\alpha_0 + Re_t/R_\omega}{1 + Re_t/R_\omega}\right) \quad (36)$$

where $\mathbf{R_\omega} = 2.95$. $\boldsymbol{\alpha}^*$ and $\mathbf{Re_t}$ are given by Equation (28) and Equation (29) respectively.

Note that in the high-Reynolds number form of the $k - \omega$ model, $\alpha = \alpha_\infty = 1$.

3.4.1.4 Modeling the Turbulence Dissipation

3.4.1.4.1 Dissipation of k

The dissipation of k is given by

$$Y_k = \rho\beta^* f_{\beta^*} k\omega \quad (37)$$

where

$$f_{\beta^*} = \begin{cases} 1 & \chi_k \le 0 \\ \dfrac{1 + 680\chi_k^2}{1 + 400\chi_k^2} & \chi_k > 0 \end{cases} \quad (38)$$

where

$$\chi_k \equiv \frac{1}{\omega^3}\frac{\partial k}{\partial x_j}\frac{\partial \omega}{\partial x_j} \quad (39)$$

and

$$\beta^* = \beta_i^*[1 + \zeta^* F(M_t)] \quad (40)$$

$$\beta_i^* = \beta_\infty^*\left(\frac{4/15 + (Re_t/R_\beta)^4}{1 + (Re_t/R_\beta)^4}\right) \quad (41)$$

$$\zeta^* = 1.5 \quad (42)$$

$$R_\beta = 8 \quad (43)$$

$$\beta_\infty^* = 0.09 \quad (44)$$

where Re_t is given by Equation (29).

3.4.1.4.2 Dissipation of ω

The dissipation of ω is given by

$$Y_\omega = \rho\beta f_\beta \omega^2 \quad (45)$$

where

$$f_\beta = \frac{1 + 70\chi_\omega}{1 + 80\chi_\omega} \quad (46)$$

$$\chi_\omega = \left|\frac{\Omega_{ij}\Omega_{jk}S_{ki}}{(\beta_\infty^*\omega)^3}\right| \quad (47)$$

$$\Omega_{ij} = \frac{1}{2}\left(\frac{\partial u_i}{\partial x_j} - \frac{\partial u_j}{\partial x_i}\right) \quad (48)$$

The strain tensor is defined by

$$S_{ij} = \frac{1}{2}\left(\frac{\partial u_j}{\partial x_i} + \frac{\partial u_i}{\partial x_j}\right) \quad (49)$$

Also,

$$\beta = \beta_i\left[1 - \frac{\beta_i^*}{\beta_i}\zeta^* F(M_t)\right] \quad (50)$$

β_i^* and $F(M_t)$ are defined by Equation (41) and Equation (51), respectively.

3.4.1.4.3 Compressibility Correction

The compressibility function, $\mathbf{F(M_t)}$, is given by

$$F(M_t) = \begin{cases} 0 & M_t \le M_{t0} \\ M_t^2 - M_{t0}^2 & M_t > M_{t0} \end{cases} \quad (51)$$

where

$$M_t^2 \equiv \frac{2k}{a^2} \quad (52)$$

$$M_{t0} = 0.25 \quad (53)$$

$$a = \sqrt{\gamma RT} \quad (54)$$

Note that, in the high-Reynolds number form of the $k-\omega$ model, $\beta_i^* = \beta_\infty^*$. In the incompressible form, $\beta^* = \beta_\infty^*$.

3.4.1.5 Model Constants

$$\alpha_\infty^* = 1,\ \alpha_\infty = 0.52,\ \alpha_0 = \frac{1}{9},\ \beta_\infty^* = 0.09,\ \beta_i = 0.072,\ R_\beta = 8$$
$$R_k = 6,\ R_\omega = 2.95,\ \zeta^* = 1.5,\ M_{t0} = 0.25,\ \sigma_k = 2.0,\ \sigma_\omega = 2.0$$

3.4.2 Shear-Stress Transport (SST) $k-\omega$ Model

The shear-stress transport (SST) $k-\omega$ model was developed by Menter [40] to effectively blend the robust and accurate formulation of the $k-\omega$ model in the near-wall region with free-stream independence of the $k-\varepsilon$ model in the far field. To achieve this, the $k-\varepsilon$ model is converted into a $k-\omega$ formulation. The SST $k-\omega$ model is similar to the standard $k-\omega$ model, but includes the following refinements:

- The standard $k-\omega$ model and the transformed $k-\varepsilon$ model are both multiplied by a blending function and both models are added together. The blending function is designed to be one in the near-wall region, which activates the standard $k-\omega$ model, and zero away from the surface, which activates the transformed $k-\varepsilon$ model.
- The SST model incorporates a damped cross-diffusion derivative term in the ω equation.
- The definition of the turbulent viscosity is modified to account for the transport of the turbulent shear stress.
- The modeling constants are different.

These features make the SST $k-\omega$ model more accurate and reliable for a wide class of flows than the standard $k-\omega$ model [29].

3.4.2.1 Transport Equations for the SST $k-\omega$ Model

The SST $k-\omega$ model has a similar form to the standard $k-\omega$ model:

$$\frac{\partial}{\partial t}(\rho k)+\frac{\partial}{\partial x_i}(\rho k u_i)=\frac{\partial}{\partial x_j}\left(\Gamma_k\frac{\partial k}{\partial x_j}\right)+\widetilde{G}_k-Y_k+S_k \quad (55)$$

and

$$\frac{\partial}{\partial t}(\rho \omega)+\frac{\partial}{\partial x_i}(\rho \omega u_i)=\frac{\partial}{\partial x_j}\left(\Gamma_\omega\frac{\partial \omega}{\partial x_j}\right)+G_\omega-Y_\omega+D_\omega+S_\omega \quad (56)$$

In these equations, $\widetilde{G}_k$ represents the generation of turbulence kinetic energy due to mean velocity gradients, calculated from G_k and defined in Equation (66). G_ω represents the generation of ω, calculated as described for the standard $k-\omega$ model. Γ_k and Γ_ω represent the effective diffusivity of k and ω, respectively, which are calculated as described below. Y_k and Y_ω represent the dissipation of k and ω due to turbulence. D_ω represents the cross-diffusion term, calculated as described below. S_k and S_ω are user-defined source terms.

3.4.2.2 Modeling the Effective Diffusivity

The effective diffusivities for the SST $k-\omega$ model are given by

$$\Gamma_k=\mu+\frac{\mu_t}{\sigma_k} \quad (57)$$

$$\Gamma_\omega=\mu+\frac{\mu_t}{\sigma_\omega} \quad (58)$$

where σ_k and σ_ω are the turbulent Prandtl numbers for k and ω, respectively. The turbulent viscosity, μ_t, is computed as follows:

$$\mu_t=\frac{\rho k}{\omega}\frac{1}{max\left[\frac{1}{\alpha^*},\frac{SF_2}{a_1\omega}\right]} \quad (59)$$

where S is the strain rate magnitude and

$$\sigma_k=\frac{1}{F_1/\sigma_{k,1}+(1-F_1)/\sigma_{k,2}} \quad (60)$$

α^* is defined in Equation (28). The blending functions, F_1 and F_2, are given by

$$F_1=tanh\left(\Phi_1^4\right) \quad (61)$$

$$\Phi_1=min\left[max\left(\frac{\sqrt{k}}{0.09\omega y},\frac{500\mu}{\rho y^2\omega}\right),\frac{4\rho k}{\sigma_{\omega,2}D_\omega^+ y^2}\right] \quad (62)$$

$$D_\omega^+=max\left[2\rho\frac{1}{\sigma_{\omega,2}}\frac{1}{\omega}\frac{\partial k}{\partial x_j}\frac{\partial \omega}{\partial x_j},10^{-10}\right] \quad (63)$$

$$F_2 = tanh\left(\Phi_2^2\right) \quad (64)$$

$$\Phi_2 = max\left[2\frac{\sqrt{k}}{0.09\omega y}, \frac{500\mu}{\rho y^2 \omega}\right] \quad (65)$$

where $\mathbf{y}$ is the distance to the next surface and $\mathbf{D}_{\omega}^{+}$ is the positive portion of the cross-diffusion term.

3.4.2.3 Modeling the Turbulence Production

3.4.2.3.1 Production of k

The term $\widetilde{G}_k$ represents the production of turbulence kinetic energy, and is defined as:

$$\widetilde{G}_k = min(G_k, 10\rho\beta^* k\omega) \quad (66)$$

where G_k is defined in the manner as in the standard $k-\omega$ model.

3.4.2.3.2 Production of ω

The term G_ω represents the production of ω and is given by

$$G_\omega = \frac{\alpha}{\nu_t}\widetilde{G}_k \quad (67)$$

Note that this formulation differs from the standard $k-\omega$ model. The difference between the two models also exists in the way the term α_∞ is evaluated. In the standard $k-\omega$ model, α_∞ is defined as constant (0.52). For the SST $k-\omega$ model, α_∞ is given by

$$\alpha_\infty = F_1\alpha_{\infty,1} + (1 - F_1)\alpha_{\infty,2} \quad (68)$$

where

$$\alpha_{\infty,1} = \frac{\beta_{i,1}}{\beta_\infty^*} - \frac{\kappa^2}{\sigma_{w.1}\sqrt{\beta_\infty^*}} \quad (69)$$

$$\alpha_{\infty,2} = \frac{2}{\beta_\infty^*} - \frac{\kappa^2}{\sigma_{w.2}\sqrt{\beta_\infty^*}} \quad (70)$$

where κ is 0.41.

3.4.2.4 Modeling the Turbulence Dissipation

3.4.2.4.1 Dissipation of k

The term $\mathbf{Y_k}$ represents the dissipation of turbulence kinetic energy, and is defined in a similar manner as in the standard $\boldsymbol{k-\omega}$ model. The difference is in the way the term f_{β^*} is evaluated. In the standard $\boldsymbol{k-\omega}$ model, f_{β^*} is defined as a piecewise function. For the SST $\boldsymbol{k-\omega}$ model, f_{β^*} is a constant equal to 1. Thus,

$$Y_k = \rho\beta^* k\omega \qquad (71)$$

3.4.2.4.2 Dissipation of ω

The term Y_ω represents the dissipation of ω, and is defined in a similar manner as in the standard $\boldsymbol{k-\omega}$ model. The difference is in the way the terms β_i and f_β are evaluated. In the standard $\boldsymbol{k-\omega}$ model, β_i is defined as a constant (0.072) and f_β is defined in Equation (45). For the SST $\boldsymbol{k-\omega}$ model, f_β is a constant equal to 1. Thus,

$$Y_k = \rho\beta\omega^2 \qquad (72)$$

Instead of having a constant value, β_i is given by

$$\beta_i = F_1\beta_{i,1} + (1-F_1)\beta_{i,2} \qquad (73)$$

and F_1 is obtained from Equation (61).

3.4.2.5 Cross-Diffusion Modification

The SST $\boldsymbol{k-\omega}$ model is based on both the standard $\boldsymbol{k-\omega}$ model and the standard $\boldsymbol{k-\varepsilon}$ model. To blend these two models together, the standard $\boldsymbol{k-\varepsilon}$ model has been transformed into equations based on k and ω, which leads to introduction of a cross-diffusion term (D_ω in Equation (56). D_ω is defined as

$$D_\omega = 2(1-F_1)\rho\frac{1}{\omega\sigma_{\omega,2}}\frac{\partial k}{\partial x_j}\frac{\partial \omega}{\partial x_j} \qquad (74)$$

3.4.2.6 Model Constants

$\sigma_{k,1} = 1.176,\ \sigma_{\omega,1} = 2.0,\ \sigma_{k,2} = 1.0,\ \sigma_{\omega,2} = 1.168$

$a_1 = 0.31,\ \beta_{i,1} = 0.075,\ \beta_{i,2} = 0.0828$

All additional model constants (α_∞^*, α_∞, α_0, β_∞^*, R_β, R_k, R_ω, ζ^*, and M_{t0}) have the same value as for the standard $\boldsymbol{k-\omega}$ model.

3.5 Species Model - Non-premixed Combustion

In non-premixed combustion, fuel and oxidizer enter the reaction zone in distinct streams. This is in contrast to premixed systems, in which reactants are mixed at the molecular level before burning.

Under certain assumptions, the thermochemistry can be reduced to a single parameter: the mixture fraction. The mixture fraction, denoted by $\boldsymbol{f}$, is the mass fraction that originated from the fuel stream. The approach is elegant because atomic elements are conserved in chemical reactions. In turn, the mixture fraction is a conserved scalar quantity, and therefore its governing transport equation does not have a source term. Combustion is simplified to a mixing problem, and the difficulties associated with closing non-linear mean reaction rates are avoided. Once mixed, the chemistry can be modeled as being in chemical equilibrium with the Equilibrium model, being near chemical equilibrium with the Steady Diffusion Flamelet model, or significantly departing from chemical equilibrium with the Unsteady Diffusion Flamelet model [29].

3.6 $P-1$ Radiation Model

The $P-1$ radiation model is the simplest case of the more general $\boldsymbol{P-N}$ model, which is based on the expansion of the radiation intensity $\boldsymbol{I}$ into an orthogonal series of spherical harmonics [41], [42], [29].

3.6.1 The $P-1$ Model Equations

As mentioned above, the $\boldsymbol{P-1}$ radiation model is the simplest case of the $\boldsymbol{P-N}$ model. When modeling gray radiation, the following equation is obtained for the radiation flux $\boldsymbol{q_r}$ if only four terms in the series are used:

$$q_r = -\frac{1}{3(a+\sigma_S)-C\sigma_S}\nabla G \qquad (75)$$

where $\boldsymbol{a}$ is the absorption coefficient, $\boldsymbol{\sigma_S}$ is the scattering coefficient, $\boldsymbol{G}$ is the incident radiation, and $\boldsymbol{C}$ is the linear-anisotropic phase function coefficient, described below. After introducing the parameter

$$\Gamma = \frac{1}{(3(a+\sigma_S)-C\sigma_S} \qquad (76)$$

Equation (75) simplifies to:

$$q_r = -\Gamma\nabla G \qquad (77)$$

The transport equation for $\boldsymbol{G}$ is

$$\nabla\cdot(\Gamma\nabla G) - aG + 4an^2\sigma T^4 = S_G \qquad (78)$$

where $\mathbf{n}$ is the refractive index of the medium, $\boldsymbol{\sigma}$ is the Stefan-Boltzmann constant and $\mathbf{S_G}$ is a user-defined radiation source.

Combining Equation (77) and Equation (78) yields the following equation:

$$-\nabla \cdot \boldsymbol{q_r} = \boldsymbol{aG} - \boldsymbol{4an^2\sigma T^4} \qquad \textbf{(79)}$$

The expression $-\nabla \cdot \boldsymbol{q_r}$ can be directly substituted into the energy equation to account for heat sources (or sinks) due to radiation [29].

3.7 Near-Wall Treatments for Wall-Bounded Turbulent Flows

Turbulent flows are significantly affected by the presence of walls. Obviously, the mean velocity field is affected through the no-slip condition that has to be satisfied at the wall. However, the turbulence is also changed by the presence of the wall in non-trivial ways. Very close to the wall, viscous damping reduces the tangential velocity fluctuations, while kinematic blocking reduces the normal fluctuations. Toward the outer part of the near-wall region, however, the turbulence is rapidly augmented by the production of turbulence kinetic energy due to the large gradients in mean velocity.

A non-dimensional wall distance for a wall-bounded flow can be defined in the following way:

$$\boldsymbol{y^+} \equiv \frac{\boldsymbol{u_* y}}{\boldsymbol{\nu}} \qquad \textbf{(80)}$$

Where u_* is the friction velocity at the nearest wall, y is the distance to the nearest wall and ν is the local kinematic viscosity of the fluid [43].

The near-wall modeling significantly impacts the fidelity of numerical solutions, inasmuch as walls are the main source of mean vorticity and turbulence. After all, it is in the near-wall region that the solution variables have large gradients, and the momentum and other scalar transports occur most vigorously. Therefore, accurate representation of the flow in the near-wall region determines successful predictions of wall-bounded turbulent flows.

Numerous experiments have shown that the near-wall region can be largely subdivided into three layers. In the innermost layer, called the “viscous sublayer”, the flow is almost laminar, and the (molecular) viscosity plays a dominant role in momentum and heat or mass transfer. In the outer layer, called the fully-turbulent layer, turbulence plays a major role. Finally, there is an interim region between the viscous sublayer and the fully turbulent layer where the effects of molecular viscosity and turbulence are equally important. Figure 12 illustrates these subdivisions of the near-wall region, plotted in semi-log coordinates [29].

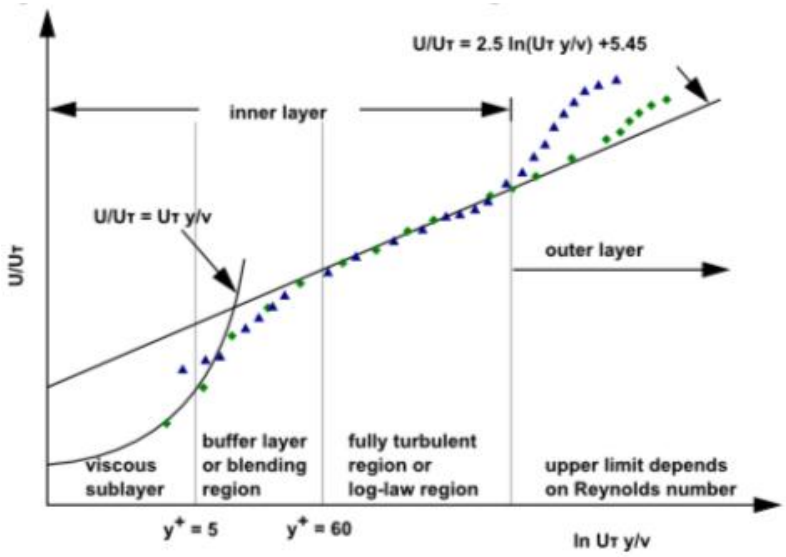

Figure 12 - Subdivisions of the Near-Wall Region [29].

In Figure 12, $y^+ \equiv {\rho u_\tau y}/{\mu}$, where u_τ is the friction velocity, defined as $\sqrt{\frac{\tau_w}{\rho}}$.

3.7.1 Wall Functions vs. Near-Wall Model

Traditionally, there are two approaches to modeling the near-wall region. In one approach, the viscosity-affected inner region (viscous sublayer and buffer layer) is not resolved. Instead, semi-empirical formulas called "wall functions" are used to bridge the viscosity-affected region between the wall and the fully-turbulent region. The use of wall functions obviates the need to modify the turbulence models to account for the presence of the wall.

In another approach, the turbulence models are modified to enable the viscosity-affected region to be resolved with a mesh all the way to the wall, including the viscous sublayer. For the purposes of discussion, this will be termed the "near-wall modeling" approach. These two approaches are depicted schematically in Figure 13.

The main shortcoming of all wall functions (except the scalable wall function) is that the numerical results deteriorate under refinement of the grid in wall normal direction. Y^+ values of below 15 will gradually result in unbounded errors in wall shear stress and wall heat transfer. While this was the industrial standard some years ago, ANSYS FLUENT has taken steps to offer more advanced wall formulations which allow a consistent mesh refinement without a deterioration of the results. Such y^+-independent formulations are the default for all ω-equation based turbulence models. For the ε-equation based models, the Enhance Wall Treatment (EWT) serves the same purpose. This option is also the default for the Spalart-Allmaras model and allows you to run this model independent of the near wall y^+-resolution.

High quality numerical results for the wall boundary layer will only be obtained if the overall resolution of the boundary layer is sufficient. This requirement is actually more

important than achieving certain y^+ values. The minimum number of cells to cover a boundary layer accurately is around 10, but values of 20 are desirable. It should also be noted that an improvement of boundary layer resolution can often be achieved with moderate increase in numerical effort, as it requires only a mesh refinement in the wall-normal direction. The associated increase in accuracy is typically well worth the additional computing costs. For unstructured meshes, it is recommended that you generate prism layers near the wall with 10–20 or more layers for an accurate prediction of the wall boundary layers. The thickness of the prism layer should be designed to ensure that around 15 or more nodes are actually covering the boundary layer. This can be checked after a solution is obtained, by looking at the turbulent viscosity, which has a maximum in the middle of the boundary layer – this maximum gives an indication of the thickness of the boundary layer (twice the location of the maximum gives the boundary layer edge). It is essential that the prism layer is thicker than the boundary layer as otherwise there is a danger that the prism layer confines the growth of the boundary layer [29].

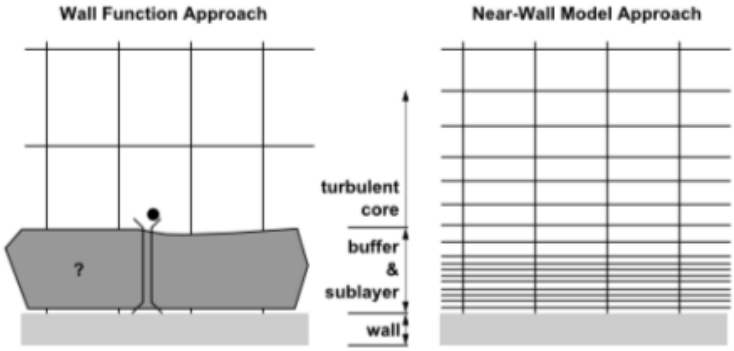

- The viscosity-affected is not resolved, instead is bridged by the wall function.
- High-Re turbulence models can be used.

- The near-wall region is resolved all the way down to the wall.
- The turbulence models ought to be valid throughout the near-wall region.

Figure 13 - Near-Wall Treatments in ANSYS FLUENT [29].

3.7.2 Wall Functions

Wall functions are a set of semi-empirical formulas and functions that in effect "bridge" or "link" the solution variables at the near-wall cells and the corresponding quantities on the wall. The wall functions comprise [29]:

- Laws-of-the-wall for the mean velocity and temperature (or other scalars);
- Formulae for the near-wall turbulent quantities.

Chapter 4

Validation of the Numerical Model

The numerical model implemented in this work will be validated using other numerical solutions; in this technique is used more than one numerical method to solve the problem. If the physics of the problem is properly modeled in all the techniques used, the results should have a clear trend and similarity; therefore, knowing the advantages and disadvantages of each technique it will be possible to perform a validation of our technique [44].

Also it is used the validation using convergence; this type of validation is based on a comparison of the convergence of the numerical model with the pattern or the reference results. This comparison is done knowing that the solution found is not the best, but assuming that the model results converge.

4.1 Combustion Chamber

The chosen combustor chamber geometry was based on the one used by Ghenai [45], that was also employed in the work of Pathan et al. [46]. As in both works the data of the geometry is not complete some data had to be estimated; therefore some differences occur between the geometry of this study and the ones that it had been based.

The CAD model of the gas turbine can combustor, Figure 14 and Figure 15, was design in the software CATIA V5R20.

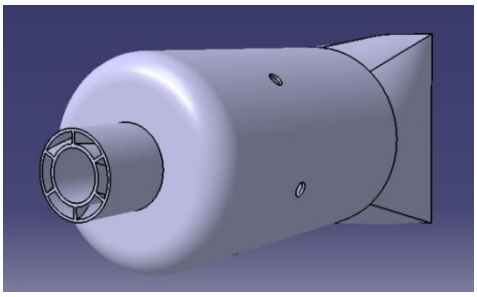

Figure 14 – CAD model of the gas turbine can combustor.

The size of the combustor is $590\ \mathrm{mm}$ in the Z direction, $250\ \mathrm{mm}$ in the Y direction, and $220\ \mathrm{mm}$ in the X direction (see Figure 16).

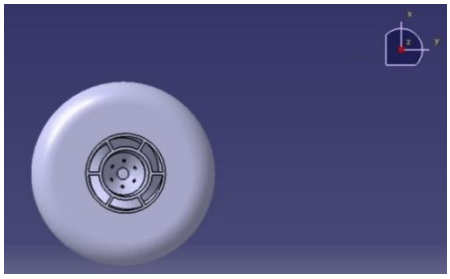

Figure 15 – Front view of the CAD model of the gas turbine can combustor.

The primary inlet air is guided by vanes to give the air a swirling velocity component, and has a diameter of $85\ \mathrm{mm}$. The fuel is injected through six fuel inlets in the swirling primary air flow, having each fuel injector the diameter of $4.2\ \mathrm{mm}$. The secondary air is injected in the combustion chamber through six side air inlets each with a diameter of $16\ \mathrm{mm}$. The can combustor outlet has a rectangular shape of $250\ \mathrm{mm} \times 50\ \mathrm{mm}$. The gas turbine can combustor wall thickness is $3\ \mathrm{mm}$.

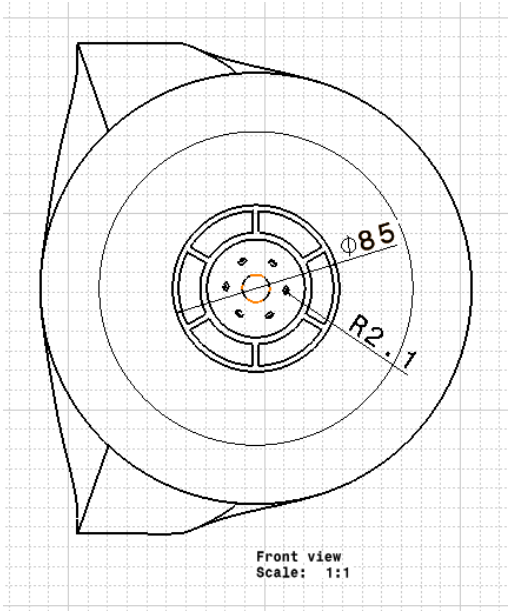

(a)

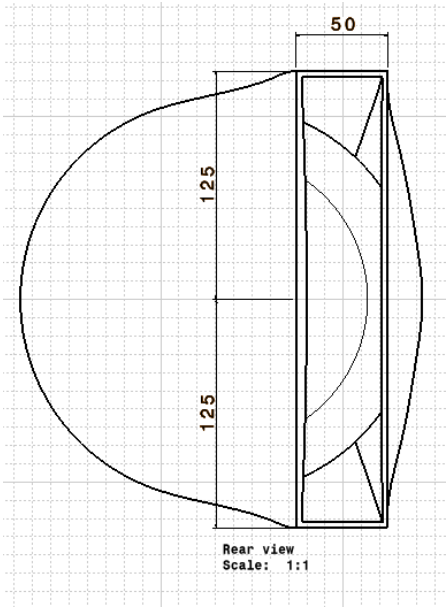

(b)

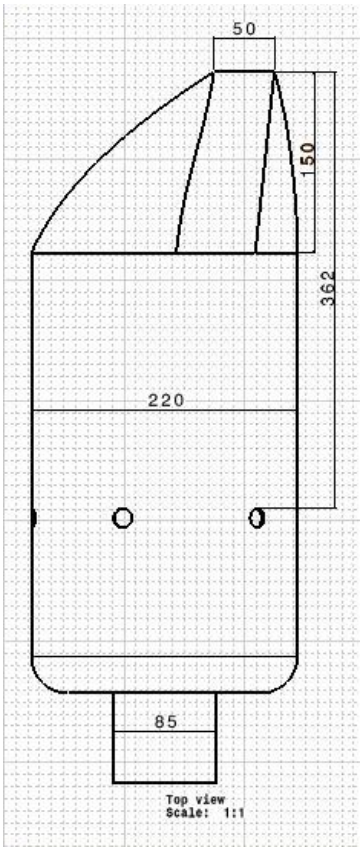

(c)

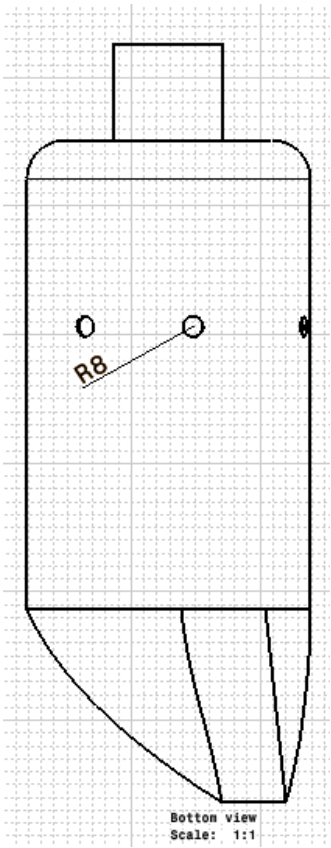

(d)

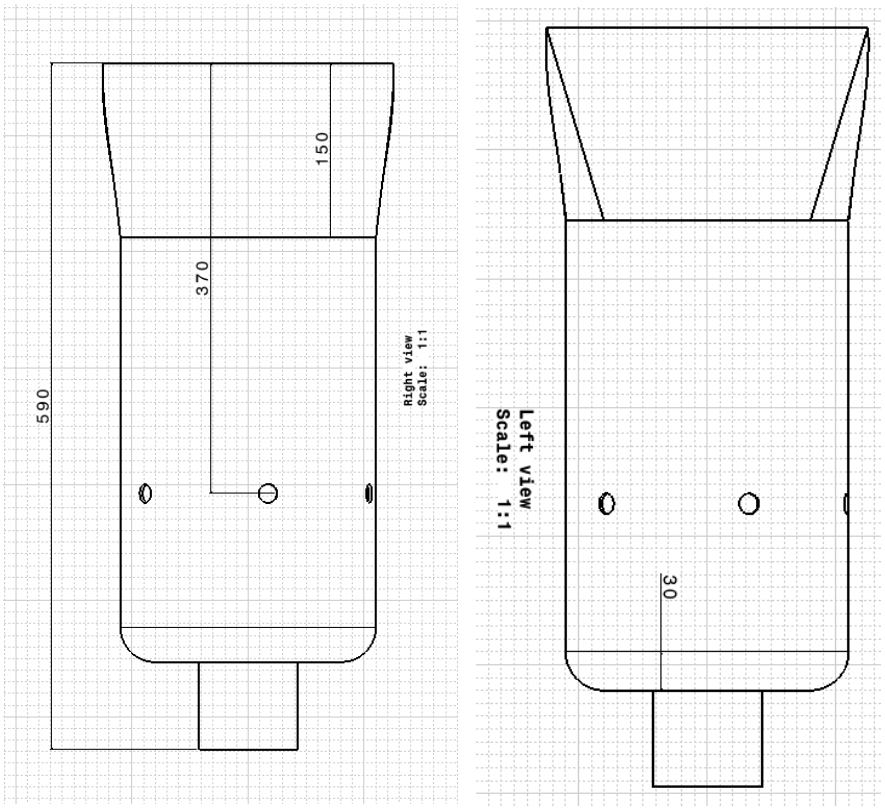

(e) **(f)**

Figure 16 – Gas turbine can combustor dimensions **(a)** Front view; **(b)** Rear view; **(c)** Top view; **(d)** Bottom view **(e)** Right view **(f)** Left view.

In Figure 17 it's possible to observe the detail of the gas turbine can combustor fuel injectors.

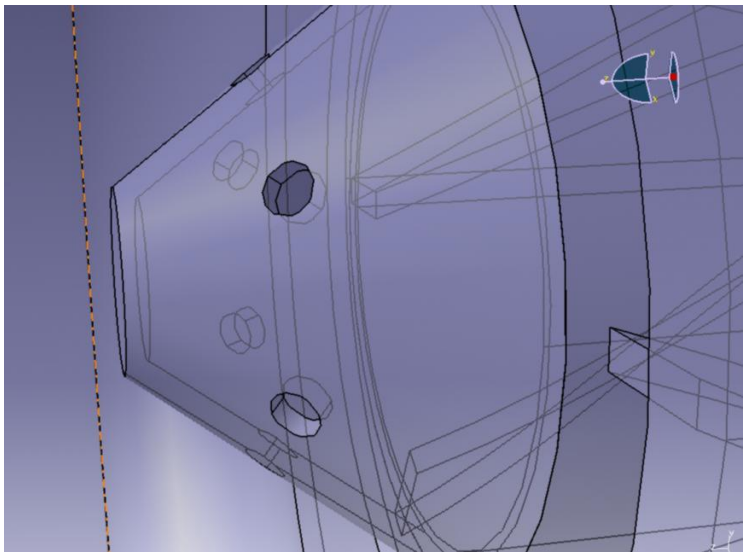

Figure 17 – Detail of the gas turbine can combustor fuel injectors.

In the ANSYS FLUENT simulation, only the volume inside the gas turbine can combustor will be needed, therefore it was made an pad of this volume in CATIA V5R20, as it can be seen in Figure 18 and Figure 19, that then it was export to ANSYS 14.5, see Figure 20.

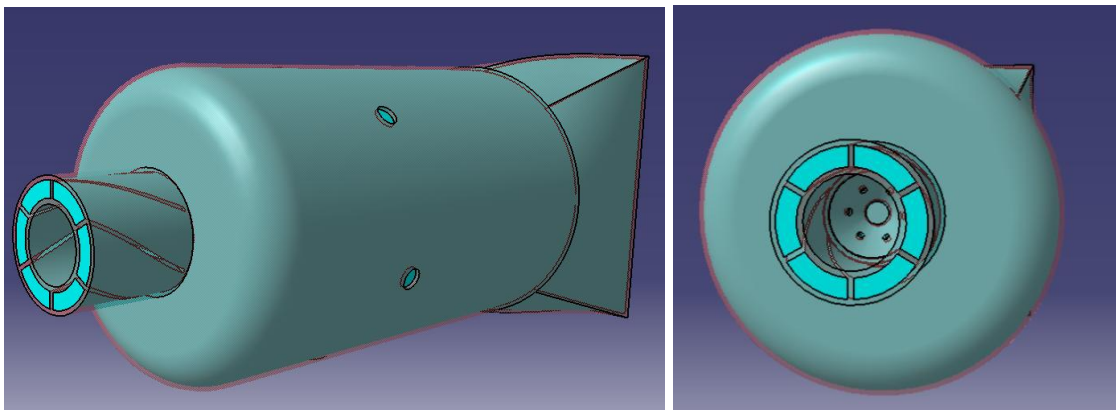

Figure 18 – Gas turbine can combustor chamber with the volume pad inside.

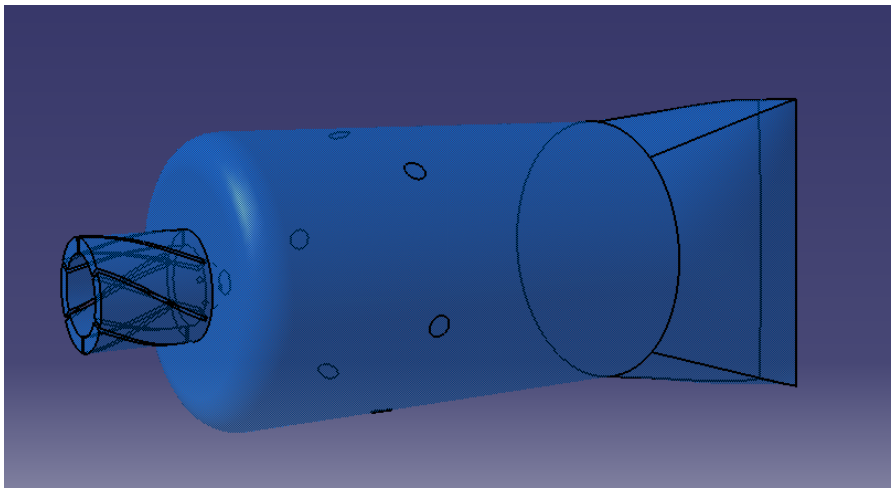

Figure 19 – Gas turbine can combustor volume pad.

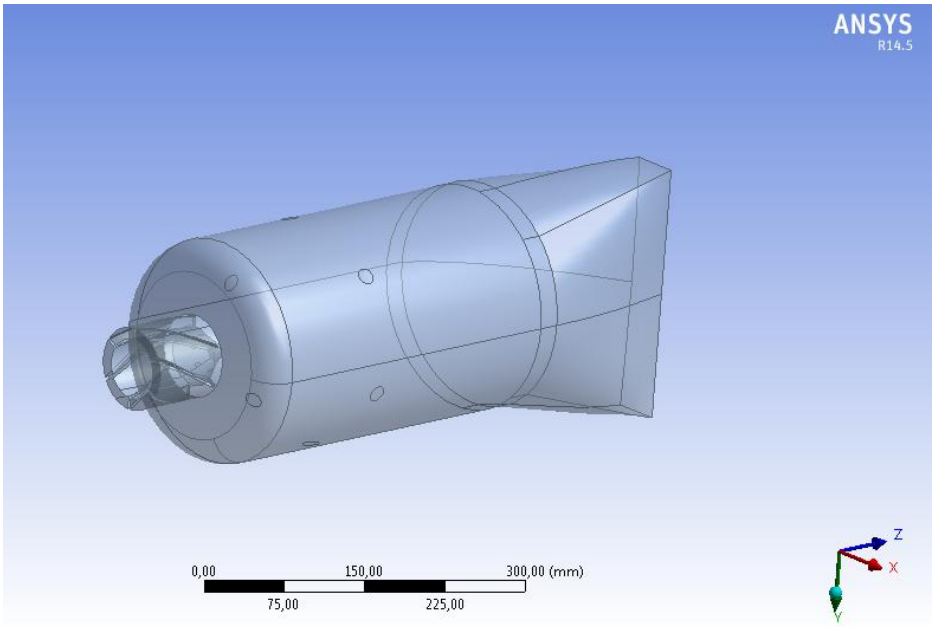

Figure 20 – Gas turbine can combustor volume pad in ANSYS 14.5 DesignModeler.

4.2 Mesh

In order to obtain the best computational results for the validation of the numerical model several meshes were generated (see Table 6).

Table 6 – Number of nodes and elements of the gas turbine can combustor several meshes.

Meshes		
Mesh	**Nodes**	**Elements**
Mesh 1	292 118	1 095 538
Mesh 2	176 645	624 572
Mesh 3	67 980	205 889
Mesh 4	65 492	190 840

The one that gave the best results was Mesh 2 (see Figure 21), being the one used in the present validation and also in the Fuel Optimization (which will be later discussed on Chapter 5).

Mesh 2 was considered the best option because it was the one, when employed, that gave results of CO_2 and NO average mass fraction at the exit of the can combustor more similar to the ones obtained by Ghenai [45] (these values will be discussed later on this chapter) when compared with Mesh 1, Mesh 3 and Mesh 4. Also it was with this mesh that the standard $\boldsymbol{k-\varepsilon}$ model and the SST $\boldsymbol{k-\omega}$ model gave almost exactly the same values.

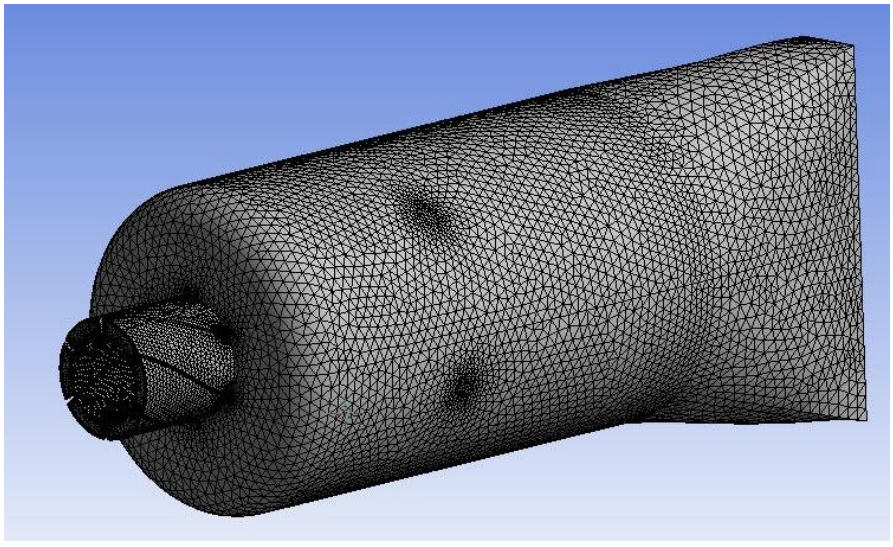

Figure 21 – Mesh for the geometry of the can combustor - Mesh 2

Notice that the mesh used by Ghenai [45] consisted of $106\,651$ elements, with a maximum cell skewness of 0.99, and a maximum aspect ratio of 83.17.

Mesh 2 is composed by three types of elements, tetrahedral, wedges, and pyramids and is metrics are described in Table 7.

Table 7 – Mesh 2 Metrics.

Mesh 2 - Mesh Metric

Element Quality	**Min**	8.675×10^{-2}	**Aspect Ratio**	**Min**	1.165
	Max	0.999		**Max**	19.433
	Average	0.678		**Average**	3.156
	Standard Deviation	0.257		**Standard Deviation**	2.266
Jacobian Ratio	**Min**	1	**Warping Factor**	**Min**	0
	Max	4.969		**Max**	0.361
	Average	1.039		**Average**	1.905×10^{-2}
	Standard Deviation	0.119		**Standard Deviation**	2.007×10^{-2}
Parallel Deviation	**Min**	0	**Maximum Corner Angle**	**Min**	60.032°
	Max	74.147		**Max**	165.05°
	Average	7.711		**Average**	88.435°
	Standard Deviation	6.335		**Standard Deviation**	16.357°
Skewness[1]	**Min**	1.444×10^{-4}	**Orthogonal Quality**	**Min**	0.112
	Max	0.888		**Max**	0.999
	Average	0.236		**Average**	0.865
	Standard Deviation	0.136		**Standard Deviation**	0.105

4.3 Fuel

The fuel selected to be applied in the validation of the numerical model was methane (CH_4), note that this fuel has been also used by Ghenai [45].

Methane is the simplest member of the paraffin series of hydrocarbons, is a colorless, and odorless gas that occurs abundantly in nature as the chief constituent of natural gas, as a component of firedamp in coal mines, and as a product of the anaerobic bacterial decomposition of vegetable matter under water, it is also produced industrially by the destructive distillation of bituminous coal in the manufacture of coal gas and coke-oven gas [47]. On Figure 22 is shown the methane cycle.

[1] Skewness is one of the primary quality measures for a mesh. Skewness determines how close to ideal a face or cell is. Its value varies between 0 and 1. A value of 1 indicates a degenerate cell quality and a value of 0 indicates a equilateral cell quality [29].

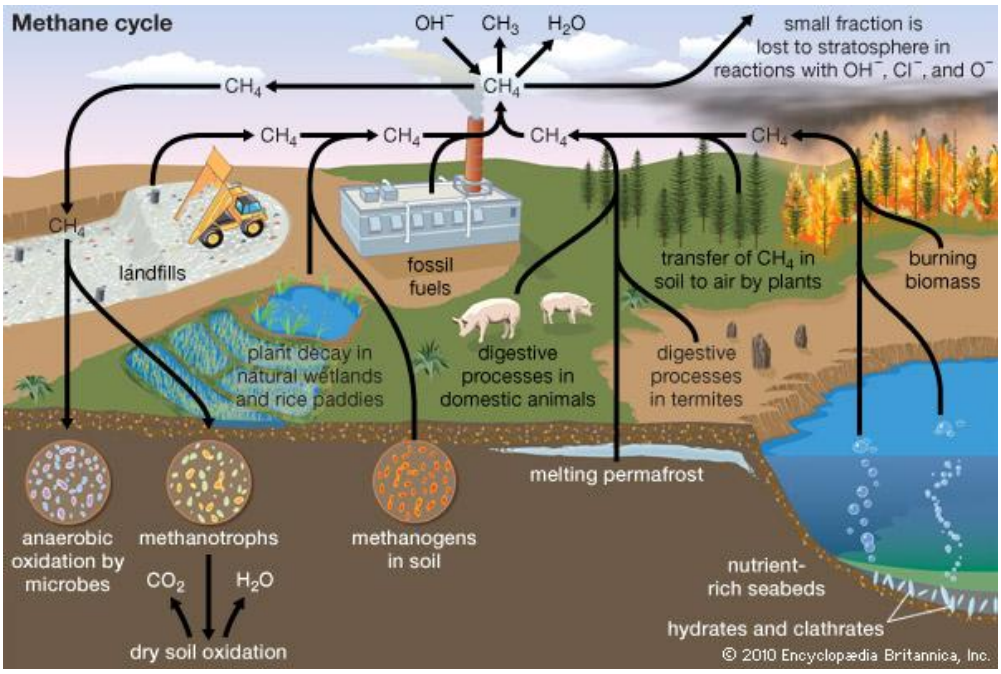

Figure 22 - Methane cycle [47].

The combustion of methane is a chemical reaction that occurs between carbon, or hydrogen, and oxygen. Heat is given off as the reaction takes place. The products of combustion are carbon dioxide and water [1]. The reaction is

$$\mathbf{CH_4 + 4O \rightarrow CO_2 + 2H_2O + Heat}$$

$$(Methane + Oxygen) \rightarrow (Carbon\ dioxide + Water + Heat)$$

Four parts of oxygen are required to burn one part of methane. The products of combustion are one part of carbon dioxide and two parts of water. One cubic foot[2] of methane will produce one cubic foot of carbon dioxide gas.

Oxygen used for combustion occurs in the atmosphere. The chemical composition of air is approximately 21% oxygen and 79% nitrogen, or one part oxygen to four parts nitrogen.

Oxygen and nitrogen molecules each contain two atoms of oxygen or nitrogen. Noting that one part, or molecule, of methane requires four parts of oxygen for complete combustion, and since the oxygen molecule contains two atoms, or two parts, the volumetric ratio of methane and oxygen is as follows:

$$\mathbf{1CH_4 + 2(O_2 \pm 4N_2) \rightarrow 1CO_2 + 8N_2 + 2H_2O + Heat}$$

The preceding equation is the true chemical equation for the combustion process. One cubic foot of methane actually requires two cubic feet of oxygen for combustion.

Since the oxygen is contained in air, which also has nitrogen, the combustion reaction can be written as follows:

$$\mathbf{1CH_4 + 2(O_2 + 4N_2) \rightarrow 1CO_2 + 8N_2 + 2H_2O + Heat}$$

$$(Methane + Air) \rightarrow (Carbon\ dioxide + Nitrogen + Water + Heat)$$

[2] $1\ cubic\ foot$ (cu. ft) $\cong 0.03$ cubic meters (m^3)

0.03 cubic meters of methane requires $0.28\ \mathrm{m}^3$ of air ($0.06\ \mathrm{m}^3$ of oxygen and $0.23\ \mathrm{m}^3$ of nitrogen) for combustion. The products are carbon dioxide, nitrogen, and water. The combustion product of one cubic foot of methane yields a total of $0.25\ \mathrm{m}^3$ of carbon dioxide gas. Also, the gas burned contains some ethane, propane, and other hydrocarbons. The yield of inert combustion gas from burning a $0.03\ \mathrm{m}^3$ of methane will be $0.26\ \mathrm{m}^3$.

If the combustion process created only the reactions shown previous, no provision would be necessary for control. Unfortunately, other reactions occur in which undesirable products are formed like $\mathrm{NO_x}$[3].

4.4 Numerical Conditions

In order to validate the study, it's necessary to delimit the numerical models several options and define the boundary conditions.

4.4.1 Numerical Models

The numerical models initially used were the $\boldsymbol{k-\varepsilon}$ model, the Non-Premixed Combustion and de $\mathrm{P-1}$ radiation model, that are the ones used in the work *"Combustion of Syngas Fuel in Gas Turbine Can Combustor"* [45]; this numerical models have been already described in Chapter 3.

But, as it will be later explained in the Results and Discussion of the Validation of the Numerical Model, there was the need to apply a $\boldsymbol{k-\omega}$ model, instead of a $\boldsymbol{k-\varepsilon}$ model.

First of all, the Energy Equation was enabled. Then the standard $\boldsymbol{k-\varepsilon}$ model was chosen with the Enhanced Wall Treatment enabled from the options of Near-Wall Treatment.

For the Non-Premixed Combustion, in order to create a PDF Table, the following options were enabled and values defined in the selections Chemistry, Boundary, Control and Table, the ones not presented here were kept default.

Table 8 - Non-Premixed Combustion: Chemistry.

Chemistry	
PDF Options	Inlet Diffusion
State Relation	Chemical Equilibrium
Energy Treatment	Non-Adiabatic

[3] Generic term for mono-nitrogen oxides $\mathbf{NO}$ and $\mathbf{NO_2}$ (Nitric Oxide and Nitrogen Dioxide).

Table 9 - Non-Premixed Combustion: Boundary.

Boundary		
Specify Species in		Mole Fraction
Temperature	Fuel $[K]$	300
	Oxid $[K]$	300

Table 10 - Non-Premixed Combustion: Boundary (Species).

Boundary Species		
Species	**Fuel**	**Oxid**
$\mathbf{CH_4}$	1	0
$\mathbf{N_2}$	0	0.78992
$\mathbf{O_2}$	0	0.21008

The species CO_2, NO and NO_2 where remove from the list of Species Excluded from Equilibrium.

Table 11 - Non-Premixed Combustion: Table.

Table Parameters	
Initial Number of Grid Points	15
Maximum Number of Grid Points	200
Maximum Change in Value Ratio	0.25
Maximum Change in Slope Ratio	0.25
Maximum Number of Species	20
Minimum Temperature $[K]$	275

After the entire parameters of the Table 8, Table 9, Table 10, and Table 11 were defined the PDF Table was calculated.

In the $\boldsymbol{P-1}$ radiation model all the FLUENT specifications where maintained unaltered.

After the computational simulation was accomplished using the previous numerical models, a new one was made replacing the standard $\boldsymbol{k-\varepsilon}$ model with the SST $\boldsymbol{k-\omega}$ model.

4.4.2 Boundary Conditions

The boundary conditions are the same ones used by Chaouki Ghenai [45], which are described on Table 12, Table 13, and Table 14; the boundary conditions explicit where will also be employed next on Chapter 5.

Table 12 – Boundary conditions of the primary air.

Primary Air		
Injection Velocity	10	m/s
Temperature	300	K
Turbulence Intensity	10	$\%$
Mixture Fraction	$f = 0$	

Table 13 - Boundary conditions of the fuel.

Fuel		
Mass Flow Rate	0.001	Kg/s
Temperature	300	K
Turbulence Intensity	10	$\%$
Mixture Fraction	$f = 1$	

Table 14 - Boundary conditions of the secondary air.

Secondary Air		
Injection Velocity	6	m/s
Temperature	300	K
Turbulence Intensity	10	$\%$
Mixture Fraction	$f = 0$	

In Table 15 are described the boundary conditions types applied to the combustor in the ANSYS FLUENT, which are also visible in Figure 23.

Table 15 – Boundary conditions types of the gas turbine combustor can.

Boundary Conditions	
Zone	**Type**
Primary Air	velocity_inlet
Fuel	mass_flow_inlet
Secondary Air	velocity_inlet
Outlet	outflow

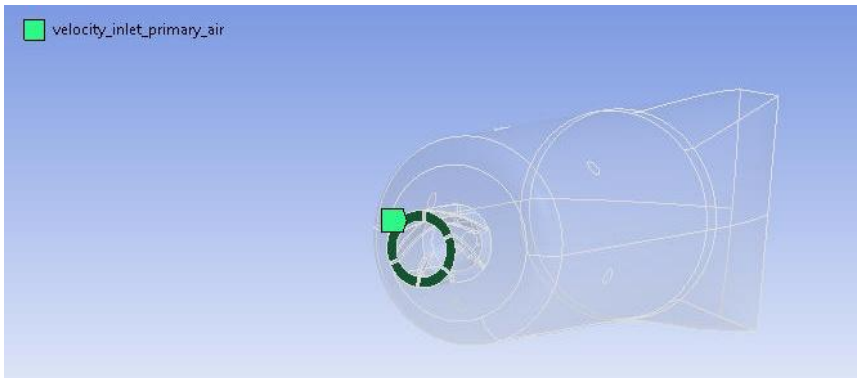

(a)

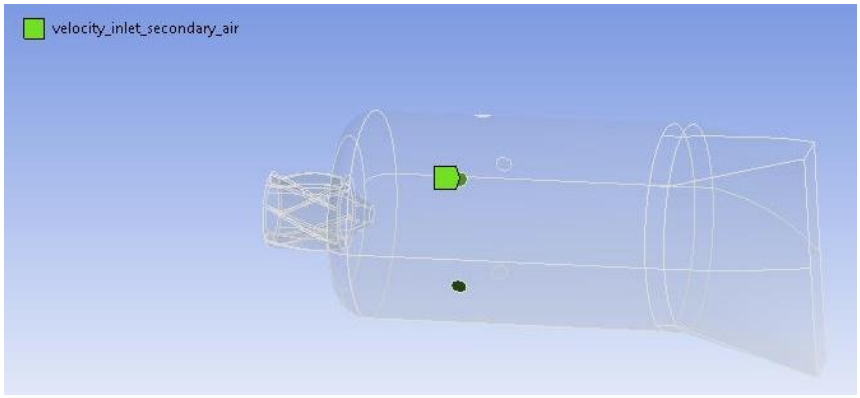

(b)

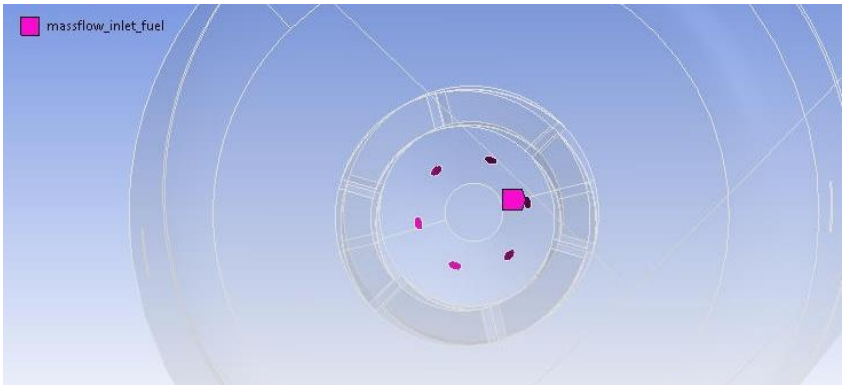

(c)

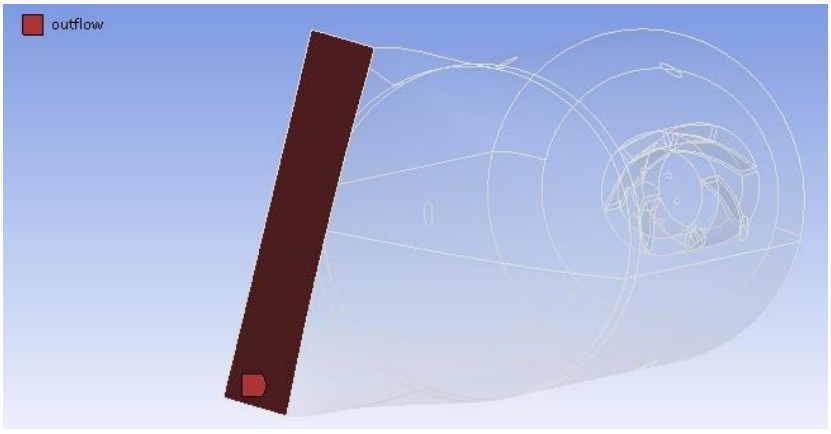

(d)

Figure 23 - Boundary conditions types. **(a)** Primary Air (velocity_inlet); **(b)** Secondary Air (velocity_inlet); **(c)** Fuel (mass_flow_inlet); **(d)** Outlet (outflow).

4.5 Numerical Method

ANSYS FLUENT allows you to choose one of the two numerical methods:

- Pressure-Based Solver;
- Density-Based Solver.

Historically speaking, the pressure-based approach was developed for low-speed incompressible flows, while the density-based approach was mainly used for high-speed compressible flows. However, recently both methods have been extended and reformulated to solve and operate for a wide range of flow conditions beyond their traditional or original intent.

In both methods the velocity field is obtained from the momentum equations. In the density-based approach, the continuity equation is used to obtain the density field while the pressure field is determined from the equation of state.

On the other hand, in the pressure-based approach, the pressure field is extracted by solving a pressure or pressure correction equation which is obtained by manipulating continuity and momentum equations.

Using either method, ANSYS FLUENT will solve the governing integral equations for the conservation of mass and momentum, and (when appropriate) for energy and other scalars such as turbulence and chemical species. In both cases a control-volume-based technique is used that consists of:

- Division of the domain into discrete control volumes using a computational grid.
- Integration of the governing equations on the individual control volumes to construct algebraic equations for the discrete dependent variables ("unknowns") such as velocities, pressure, temperature, and conserved scalars.
- Linearization of the discretized equations and solution of the resultant linear equation system to yield updated values of the dependent variables.

The two numerical methods employ a similar discretization process (finite-volume), but the approach used to linearize and solve the discretized equations is different [29].

4.5.1 Pressure-Based Solver

The numerical method employed in this work, was the Pressure-Based Solver, as defined by Dr. Francisco Brójo.

The pressure-based solver employs an algorithm which belongs to a general class of methods called the projection method [48]. In the projection method, wherein the constraint of mass conservation (continuity) of the velocity field is achieved by solving a pressure (or pressure correction) equation. The pressure equation is derived from the continuity and the momentum equations in such away that the velocity field, corrected by the pressure, satisfies the continuity. Since the governing equations are nonlinear and coupled to one another, the

solution process involves iterations wherein the entire set of governing equations is solved repeatedly until the solution converges.

Two pressure-based solver algorithms are available in ANSYS FLUENT. A segregated algorithm, and a coupled algorithm [29].

4.5.1.1 The Pressure-Based Segregated Algorithm

The pressure-based solver uses a solution algorithm where the governing equations are solved sequentially (that is, segregated from one another). Because the governing equations are non-linear and coupled, the solution loop must be carried out iteratively in order to obtain a converged numerical solution.

In the segregated algorithm, the individual governing equations for the solution variables are solved one after another. Each governing equation, while being solved, is "decoupled" or "segregated" from other equations, hence its name. The segregated algorithm is memory-efficient, since the discretized equations need only be stored in the memory one at a time. However, the solution convergence is relatively slow, inasmuch as the equations are solved in a decoupled manner.

With the segregated algorithm, each iteration consists of the steps illustrated in Figure 24 and outlined below [29]:

1. Update fluid properties (for example, density, viscosity, specific heat) including turbulent viscosity (diffusivity) based on the current solution.
2. Solve the momentum equations, one after another, using the recently updated values of pressure and face mass fluxes.
3. Solve the pressure correction equation using the recently obtained velocity field and the mass-flux.
4. Correct face mass fluxes, pressure, and the velocity field using the pressure correction obtained from Step 3.
5. Solve the equations for additional scalars, if any, such as turbulent quantities, energy, species, and radiation intensity using the current values of the solution variables.
6. Update the source terms arising from the interactions among different phases (for example, source term for the carrier phase due to discrete particles).
7. Check for the convergence of the equations.

These steps are continued until the convergence criteria are met.

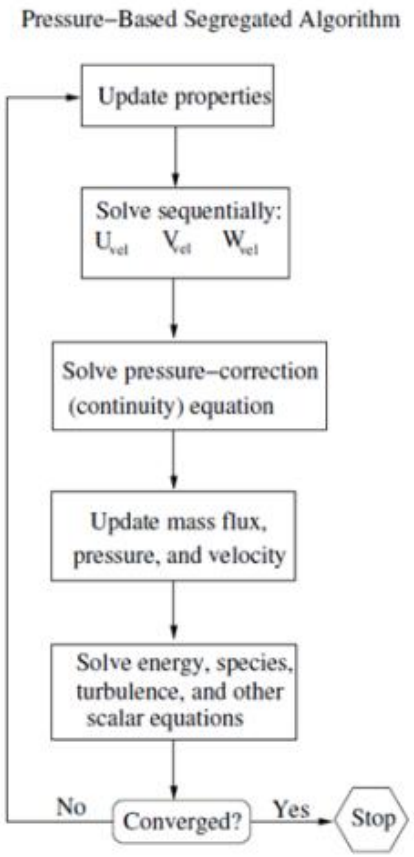

Figure 24 - Overview of the Pressure-Based Segregated Algorithm [29].

4.5.1.2 The Pressure-Based Coupled Algorithm

Unlike the segregated algorithm described above, the pressure-based coupled algorithm solves a coupled system of equations comprising the momentum equations and the pressure-based continuity equation. Thus, in the coupled algorithm, Steps 2 and 3 in the segregated solution algorithm are replaced by a single step in which the coupled system of equations are solved. The remaining equations are solved in a decoupled fashion as in the segregated algorithm. With the coupled algorithm, each iteration consists of the steps illustrated in Figure 25.

Since the momentum and continuity equations are solved in a closely coupled manner, the rate of solution convergence significantly improves when compared to the segregated algorithm. However, the memory requirement increases by $1.5 - 2$ times that of the segregated algorithm since the discrete system of all momentum and pressure-based continuity equations must be stored in the memory when solving for the velocity and pressure fields (rather than just a single equation, as is the case with the segregated algorithm) [29].

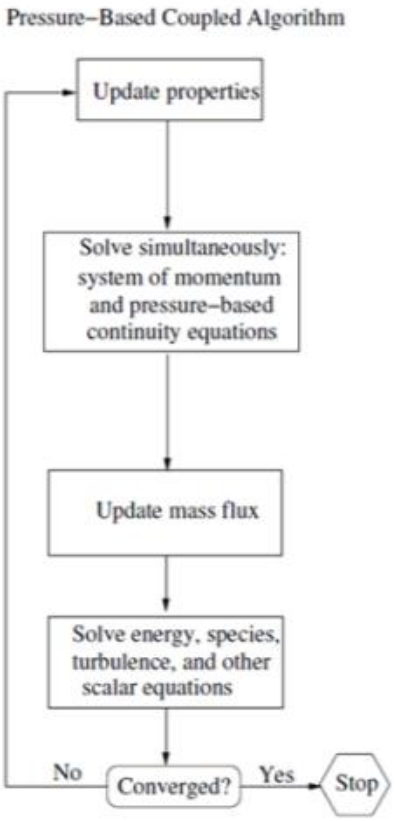

Figure 25 - Overview of the Pressure-Based Coupled Algorithm [29].

4.6 Convergence Criteria

To define the convergence criteria the values used by Ghenai [45] were taken into account; thus for the simulations that used the standard $\boldsymbol{k-\varepsilon}$ model the convergence criteria defined can be seen on Table 16, and for the SST $\boldsymbol{k-\omega}$ model on Table 17.

Table 16 - Convergence criteria used on the simulations of the standard $\boldsymbol{k-\varepsilon}$ model.

Convergence Criterion	
Residual	**Absolute Criteria**
Continuity	10^{-3}
x-velocity	10^{-3}
y-velocity	10^{-3}
z-velocity	10^{-3}
Energy	10^{-6}
Epsilon	10^{-3}
fmean	10^{-3}
fvar	10^{-3}
p1	10^{-6}

Table 17 - Convergence criteria used on the simulations of the SST $k-\omega$ model.

Convergence Criterion	
Residual	**Absolute Criteria**
Continuity	10^{-3}
x-velocity	10^{-3}
y-velocity	10^{-3}
z-velocity	10^{-3}
Energy	10^{-6}
Omega	10^{-3}
fmean	10^{-3}
fvar	10^{-3}
p1	10^{-6}

4.7 Results and Discussion of the Validation of the Numerical Model

In order to validate the numerical model the average carbon dioxide and NO mass fractions at the exit of can combustor of the combustion of methane were taken in consideration and compared with the ones obtained by Chaouki Ghenai [45] in is work *"Combustion of Syngas Fuel in Gas Turbine Can Combustor"*; the outcomes of his work can be seen in Figure 26 and Figure 27.

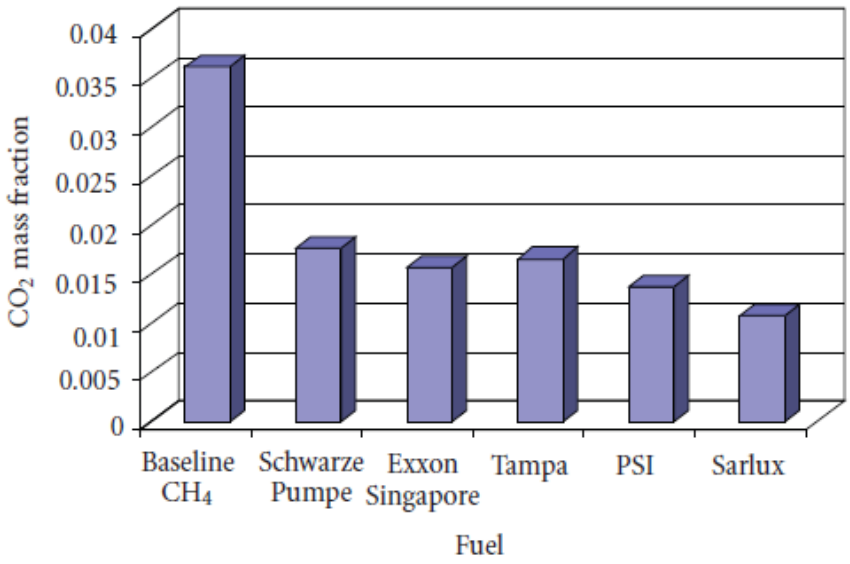

Figure 26 - Average carbon dioxide (CO_2) mass fractions at the exit of can combustor [45].

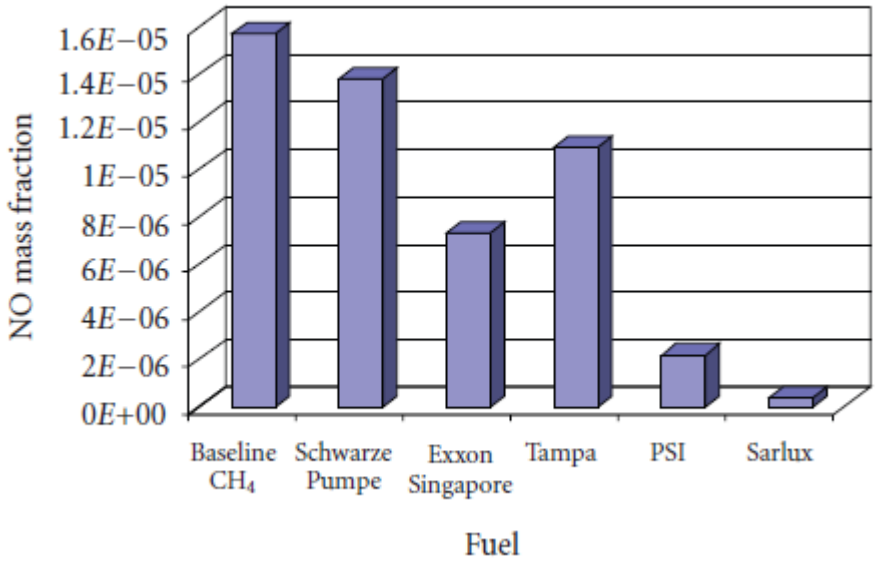

Figure 27 - Average **NO** mass fractions at the exit of the can combustor [45].

For methane (CH_4) in Figure 26 it's perceived that the average value of the CO_2 mass fraction is within a range from 0.035 to 0.04, and in Figure 27 that the average mass fraction value of NO is in a span between 0.000014 and 0.000016.

The results that were obtained in the current study using the Mesh 2 with the standard $k-\varepsilon$ model can be seen in Table 18. And the ones obtained with the SST $k-\omega$ model in Table 19.

Table 18 - Results of the average mass fraction at the exit of the can combustor with the standard $k-\varepsilon$ model.

Results - Standard k – ε Model

Specie	Average mass fraction at the exit of the can combustor
CO_2	0.07925916
NO	0.000376014

Table 19 - Results of the average mass fraction at the exit of the can combustor with the SST $k-\omega$ model.

Results - SST $k-\omega$ Model

Specie	Average mass fraction at the exit of the can combustor
CO_2	0.077498354
NO	0.00035718924

As referred earlier in this chapter, the given geometry data isn't complete and therefore the used model of the combustor has some differences from the one used in Ghenai's work, so the values expressed in Table 18 and Table 19 differ from the ones that are shown in Figure 26 and Figure 27. For better visualization of the results Figure 28, and Figure 29 can be checked.

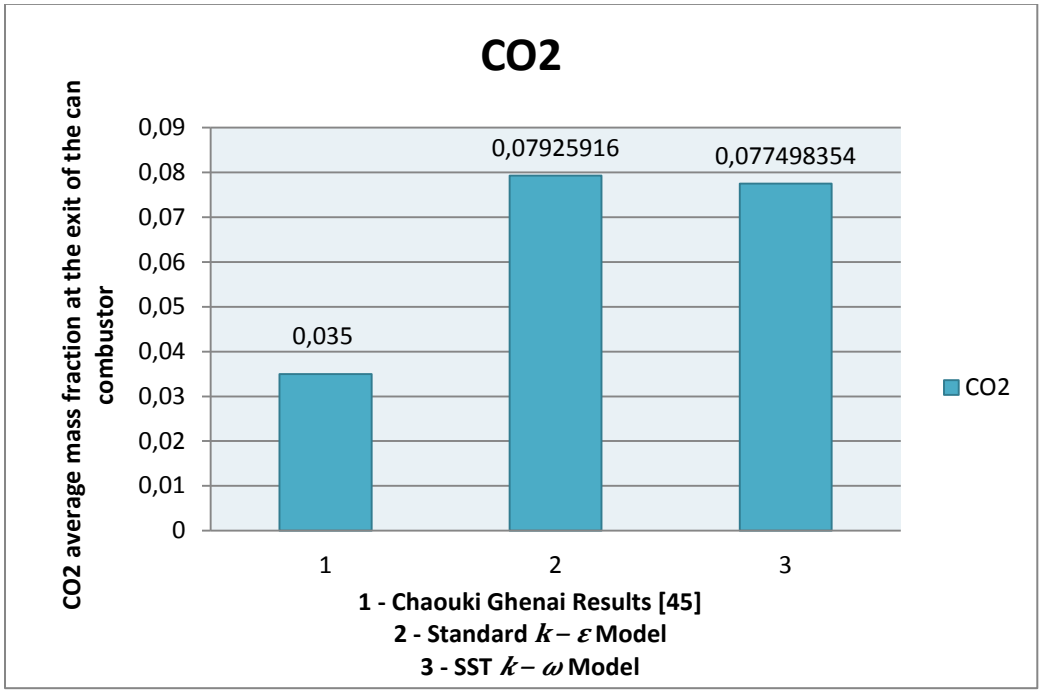

Figure 28 – Comparison between the CO_2 values obtained in the Chaouki Ghenai work [45] and the ones acquired in the validation simulations.

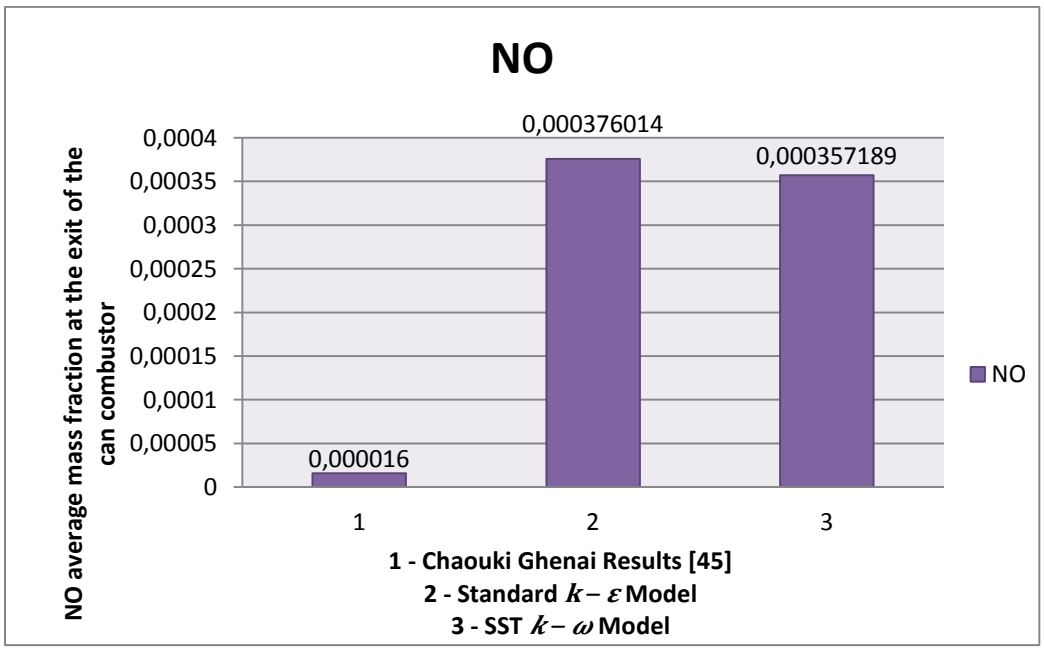

Figure 29 - Comparison between the **NO** values obtained in the Chaouki Ghenai work [45] and the ones acquired in the validation simulations.

Before was said that although the work of Ghenai used a $\boldsymbol{k-\varepsilon}$ model, there would be the need of using a $\boldsymbol{k-\omega}$ model, this is because that in the $\boldsymbol{k-\varepsilon}$ models the value of $\mathbf{y}^{+}$ at the wall-adjacent cell should be in the range of $30 < \mathbf{y}^{+} < 300$ which was not achieved in the validation of the numerical model. Has for the $\mathbf{k-\omega}$ models the value of $\mathbf{y}^{+}$ at the wall-adjacent cell should be on the order of $\boldsymbol{y^{+} \cong 1}$, being however, acceptable values of $\boldsymbol{y^{+}}$ lower than 4 to 5, values that have been obtained; being this the reason of the appliance of the SST $\boldsymbol{k-\omega}$ model.

Comparing now the values of Table 18 and Table 19, and even though they differ from the ones of Figure 26 and Figure 27, the values are very similar being this divergences cause of the differences that exist between both applied models; finally it can be consider that the validation of the numerical model as accomplished, once that also the convergence criteria was accomplished in the two models.

4.8 Conclusions

In short of Chapter 4 there are some aspects that should be retained as very important, first is that exist some differences in the geometry used by Ghenai and the one used in this study, second is the fact that these same divergences lead to not obtain the same values of the average mass fraction at the exit of the can combustor as the ones of the work *"Combustion of Syngas Fuel in Gas Turbine Can Combustor"*, and third is that there was the necessity to apply a $\boldsymbol{k-\omega}$ model.

To conclude, the numerical model was able to be validated and consequently the fuel optimization was able to be carried on.

Chapter 5

Fuel Optimization

This section focus the importance of using renewable fuels (like hydrogen) in replacement of the fossil ones due to economic and environmental reasons, explaining the differences that exist between the combustion of methane, hydrogen and methane-hydrogen mixtures through CFD simulations on FLUENT, having as a main point the comparison of the emission values of the pollutants CO, CO_2 and NO_x.

5.1 Fuels to Consider

The fuels considered are methane (CH_4) and hydrogen (H_2) both in the pure state, and also methane-hydrogen mixtures as shown in Table 20.

In Chapter 4 in the subsection Fuel was made a brief explanation of methane and its combustion.

Table 20 – Fuels to consider in the Fuel Optimization.

Fuel	Methane (CH_4) Percentage [%]	Hydrogen (H_2) Percentage [%]
Fuel 1[4]	100	0
Fuel 2	75	25
Fuel 3	50	50
Fuel 4	25	75
Fuel 5	0	100

Regarding hydrogen although it's the most abundant element in the Universe, it makes up only about 0.14 percent of the Earth's crust by weight. It occurs, however, in vast quantities as part of the water in oceans, ice packs, rivers, lakes, and the atmosphere [7] (see Figure 30 for the cycle of renewable hydrogen). Molecular hydrogen is a future energy source/carrier that is being actively investigated as an alternative to fossil fuels. It reacts with oxygen, forming only water; hence, it is a clean renewable energy source, and it has a high calorific value [49].

However, the use of hydrogen in gas turbine combustors is not straightforward since hydrogen has some characteristics that strongly deviate from those of the main components of conventional fuels, such as methane. Hydrogen is strongly exposed to molecular diffusion

[4] Fuel used in the validation of the numerical model.

processes and has a wide flammability range, short ignition times, and a high laminar flame speed. The relatively high adiabatic temperatures of H_2/air mixtures might cause large amounts of thermal NO_x in the flame. The flame temperature, and therefore NO_x emissions, can be reduced by lean premixing of fuel and air. However, the high reactivity and flame speed of premixed H_2/air mixtures enhance the danger of autoignition and flashback, respectively [50].

Hydrogen combustion is the process by which hydrogen reacts with an oxidizing agent and burns. Hydrogen combustion is an exothermic combustion, meaning that it releases heat energy. Hydrogen burns based on the chemical formula

$$\mathbf{2H_2 + O_2 \rightarrow 2H_2O + Heat}$$

meaning that it reacts with oxygen. While it is not shown in the chemical equation, an input of energy is necessary to begin the reaction, which releases a significant amount of energy when carried through to completion [51].

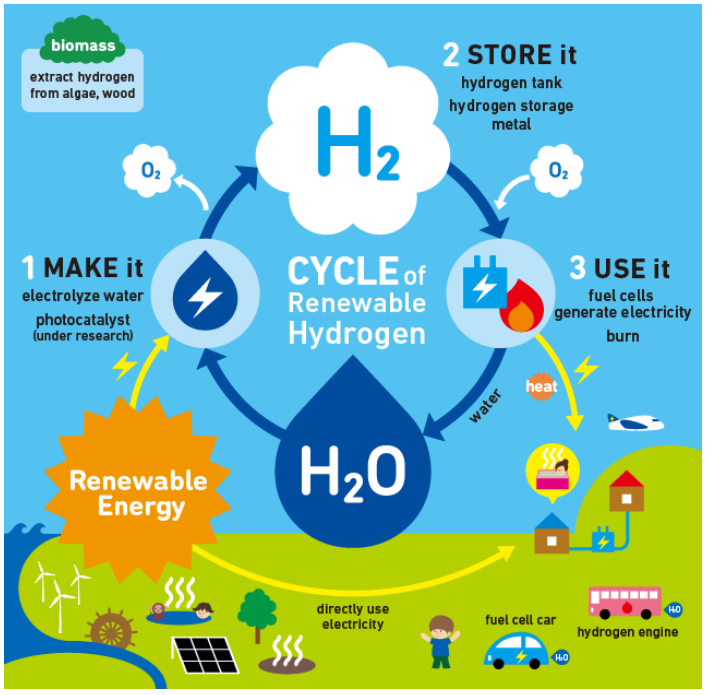

Figure 30 - Cycle of renewable hydrogen [52].

5.2 Emissions

As stated before pollutant emissions from combustion processes have become a global concern due to their impact on the environment.

The exhaust from a gas turbine is composed of carbon monoxide (CO), carbon dioxide (CO_2), water vapor (H_2O), unburned hydrocarbons (UHC), particulate matter (mainly carbon), NO_x, and excess atmospheric oxygen and nitrogen. CO_2 and H_2O have not always been regarded as pollutants because they are the natural consequence of complete combustion of a hydrocarbon fuel, however, they both contribute to global warming [8].

In Table 21 are enumerated the principal pollutants emitted by gas turbines and their main effects.

Table 21 - Principal pollutants emitted by gas turbines [8].

Principal Pollutants Emitted by Gas Turbines

Pollutant	Effect
Carbon Monoxide ($\mathbf{CO}$)	Toxic
Unburned Hydrocarbons ($\mathbf{UHC}$)	Toxic
Particulate Matter ($\mathbf{C}$)	Visible
Oxides of Nitrogen ($\mathbf{NO_x}$)	Toxic, precursor of chemical smog, depletion of ozone in stratosphere
Oxides of Sulfur ($\mathbf{SO_x}$)	Toxic, corrosive

In this work, like said before, emphasis will be give to the emissions of the pollutants CO, CO_2 and NO_x.

5.2.1 Carbon Monoxide

Carbon monoxide is colorless, odorless, and tasteless gas, but highly toxic. It's produced by the incomplete burning of various fuels.

When a combustion zone is operating fuel-rich, large amounts of CO are formed owing to the lack of sufficient oxygen to complete the reaction to CO_2. If, however, the combustion zone mixture strength is stoichiometric or moderately fuel-lean, significant amounts of CO will also be present due to the dissociation of CO_2 [8].

5.2.2 Carbon Dioxide

Carbon dioxide (CO_2) is the primary greenhouse gas emitted through human activities. Carbon dioxide is naturally present in the atmosphere as part of the Earth's carbon cycle. Human activities are altering the carbon cycle—both by adding more CO_2 to the atmosphere and by influencing the ability of natural sinks, like forests, to remove CO_2 from the atmosphere. While CO_2 emissions come from a variety of natural sources, human-related emissions are responsible for the increase that has occurred in the atmosphere since the industrial revolution [53].

The main human activity that emits CO_2 is the combustion of fossil fuels (coal, natural gas, and oil) for energy and transportation, although certain industrial processes and land-use changes also emit CO_2.

5.2.3 Oxides of Nitrogen

Most of the nitric oxide (NO) formed in combustion subsequently oxidizes to NO_2. For this reason, it is customary to lump NO and NO_2 together and express results in terms of NO_x, rather than NO. It can be produced by four different mechanisms: thermal NO, nitrous oxide mechanism, prompt NO, and fuel NO [8].

Nitric oxide is a gas with a sharp, sweet smell; it is colorless to brown at room temperature. Nitrogen dioxide is a colorless to brown liquid at room temperature, with a strong, harsh odor; it becomes a reddish-brown gas at temperatures above 294.261 Kelvin [54].

5.3 Optimization

In order to attempt to improve the combustion results it was made a fuel optimization. So, as explained before in the subsection Fuels to Consider hydrogen was added to methane till only H_2 was used in the simulated combustion.

The selected numerical models used in FLUENT were the same that had been previously used in the Validation of the Numerical Model (with the exception of the $\boldsymbol{k-\varepsilon}$ model, which its use had been already discarded for this work purpose), the same applies for the boundary conditions values.

Be aware that before at Chapter 4 in the Table 10 was explicit the case where the fuel was only compose by methane (Fuel 1), for the other fuel variations the boundary species composition can be checked in below in Table 22, Table 23, Table 24, and Table 25.

Table 22 - Boundary Species - Fuel 2

Boundary Species – Fuel 2

Species	Fuel	Oxid
$\mathbf{CH_4}$	0.75	0
$\mathbf{H_2}$	0.25	0
$\mathbf{N_2}$	0	0.78992
$\mathbf{O_2}$	0	0.21008

Table 23 - Boundary Species - Fuel 3

Boundary Species – Fuel 3

Species	Fuel	Oxid
CH_4	0.50	0
H_2	0.50	0
N_2	0	0.78992
O_2	0	0.21008

Table 24 - Boundary Species - Fuel 4

Boundary Species – Fuel 4

Species	Fuel	Oxid
CH_4	0.25	0
H_2	0.75	0
N_2	0	0.78992
O_2	0	0.21008

Table 25 - Boundary Species - Fuel 5

Boundary Species – Fuel 5

Species	Fuel	Oxid
CH_4	0	0
H_2	1	0
N_2	0	0.78992
O_2	0	0.21008

5.4 Results and Discussion

The results obtained through the FLUENT simulations using different fuels are exposed below. The average mass fraction of the pollutants CO, CO_2 and NO_x at the exit of the can combustor for each one of the considered fuels are displayed in Table 26, Table 27, Table 28, Table 29, and Table 30.

Table 26 – Results of the average mass fraction at the exit of the can combustor - Fuel 1

Fuel 1 - Results

Specie	Average mass fraction at the exit of the can combustor
CO	0.00012450371
CO_2	0.077498354
NO	0.00035718924
NO_2	3.118261×10^{-6}

Table 27 - Results of the average mass fraction at the exit of the can combustor - Fuel 2

Fuel 2 - Results

Specie	Average mass fraction at the exit of the can combustor
CO	0.00024271815
CO_2	0.07720089
NO	0.00052440696
NO_2	2.9794269×10^{-6}

Table 28 - Results of the average mass fraction at the exit of the can combustor - Fuel 3

Fuel 3 - Results

Specie	Average mass fraction at the exit of the can combustor
CO	0.00050059153
CO_2	0.069246151
NO	0.00081232464
NO_2	3.3103984×10^{-6}

Table 29 - Results of the average mass fraction at the exit of the can combustor - Fuel 4

Fuel 4 - Results

Specie	Average mass fraction at the exit of the can combustor
CO	0.0014575864
CO_2	0.055611413
NO	0.0010900323
NO_2	2.9880407×10^{-6}

Table 30 - Results of the average mass fraction at the exit of the can combustor - Fuel 5

Fuel 5 - Results

Specie	Average mass fraction at the exit of the can combustor
CO	0
CO_2	0
NO	0.0021973494
NO_2	1.1890703×10^{-6}

To better understand and compare the results of the average mass fraction of CO, CO_2, NO, and NO_2 at the exit of the can combustor of the different fuels the graphics exposed in Figure 31, Figure 32, Figure 33, and Figure 34 can be analyzed.

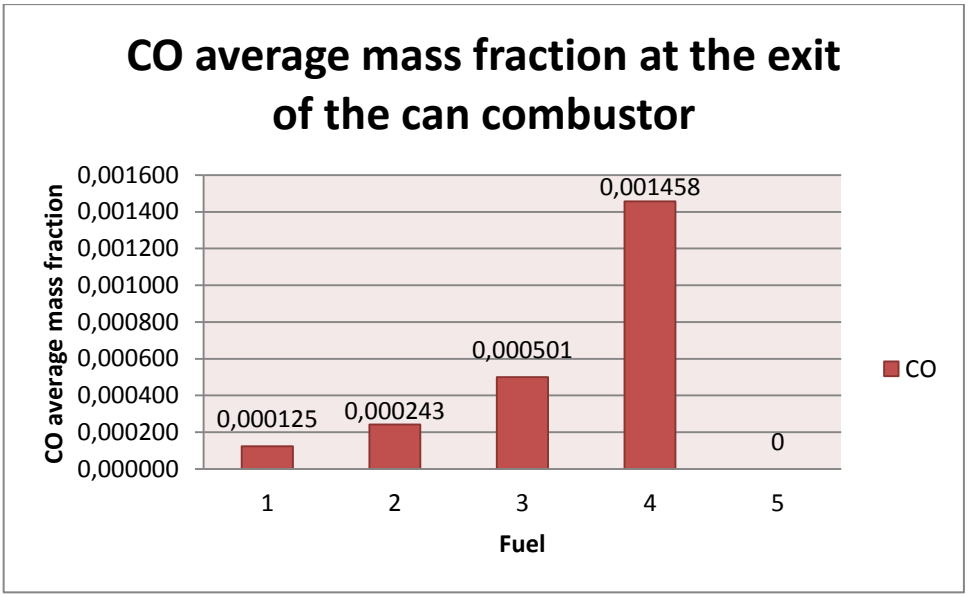

Figure 31 - CO average mass fraction at the exit of the can combustor for the several fuels.

In Figure 31 are expressed the values of CO obtained in all simulations, where it can be conclude that

- The combustion of pure methane (Fuel 1) it is the one that shows lower levels of CO emission, when compared with Fuel 2, 3 and 4.
- The adding of hydrogen to methane leads to an increase of the average mass fraction of CO;
- Only when pure hydrogen is used (Fuel 5) there is zero CO emission.

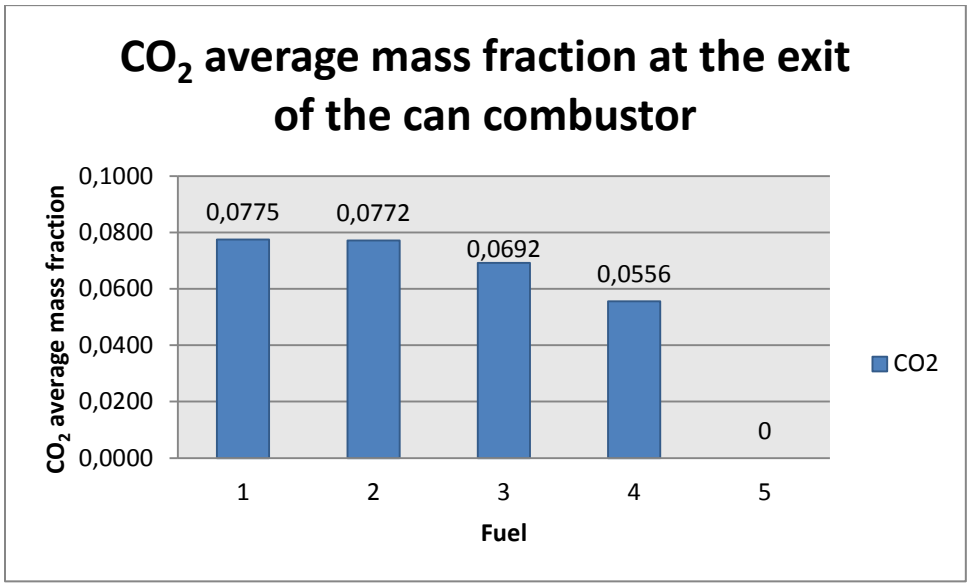

Figure 32 - CO_2 average mass fraction at the exit of the can combustor for the several fuels.

For the average mass fraction of CO_2 it can be determined by examining Figure 32 that

- The combustion of pure methane presents the highest values of CO_2 average mass fraction;
- The greater the amount of hydrogen added to methane the lower the CO_2 emission;
- For the combustion of pure hydrogen the CO_2 average mass fraction at the outlet is null.

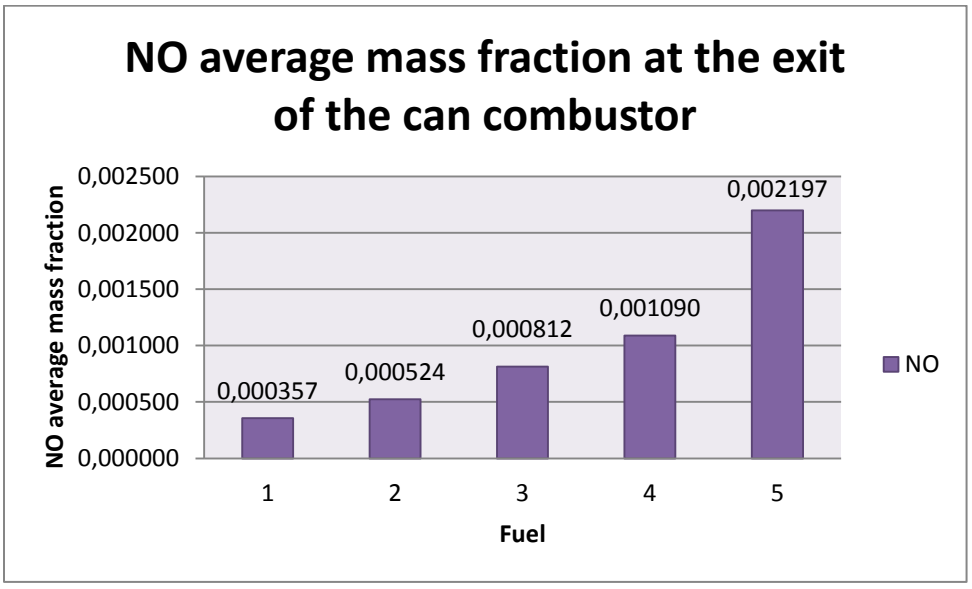

Figure 33 - NO average mass fraction at the exit of the can combustor for the several fuels.

For the NO values was verified through the analysis of Figure 33 that

- The combustion of methane presents the lower emission of NO average mass fraction;

- The adding of hydrogen to methane leads to an increase of the value of NO;
- The greater value of NO average mass fraction is achieved when the combustion fuel is one hundred percent H_2.

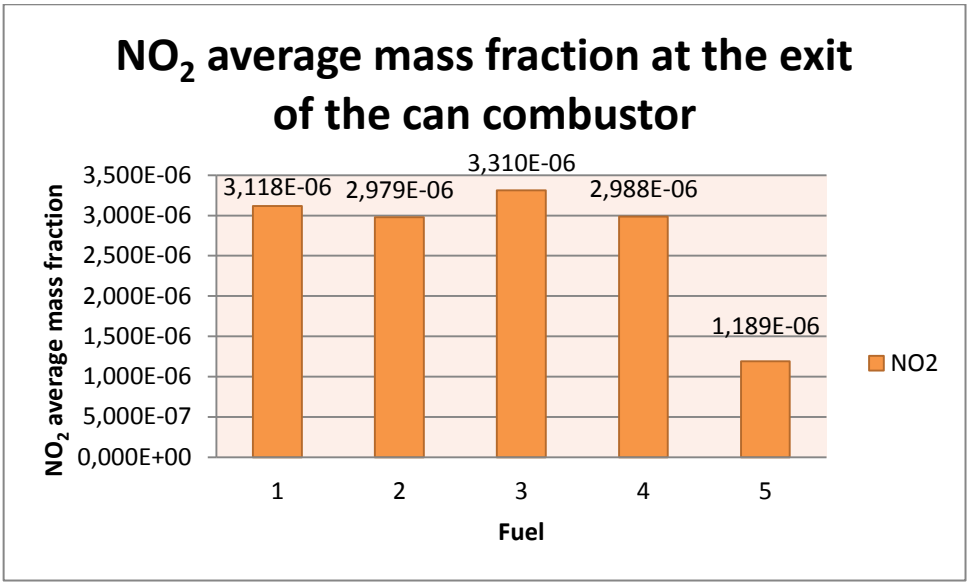

Figure 34 - NO_2 average mass fraction at the exit of the can combustor for the several fuels.

Finally for the average mass fraction of NO_2 at the exit of the can combustor (see Figure 34) the results were inconclusive. When Fuel 2 is analyzed it can be noticed that there is a slightly drop of the emission of NO_2 when compared with the combustion of Fuel 1. Fuel 3 presents the maximum NO_2 value of all simulations and Fuel 5 the minimum. Ultimately for Fuel 4 and 5 a decrease of the average mass fraction of NO_2 at the outlet occurs, even though the value obtained for Fuel 4 is slightly greater than the one of Fuel 2.

The values of the contours of static temperature, static pressure, and velocity magnitude of the study case for every single considered fuel are exhibited further down. Note that for better understanding a plane was used to show the contours, as if all the combustor was presented the results would be unclear. Therefore the used plane, for all the applied fuels (Fuel 1, 2, 3, 4 and 5), to show the contours was the $\boldsymbol{xz}$ plane (meaning that the coordinate $\boldsymbol{y = 0}$).

For Fuel 1 the contours of static temperature, static pressure, and the velocity magnitude are exposed in Figure 35, Figure 36, and Figure 37.

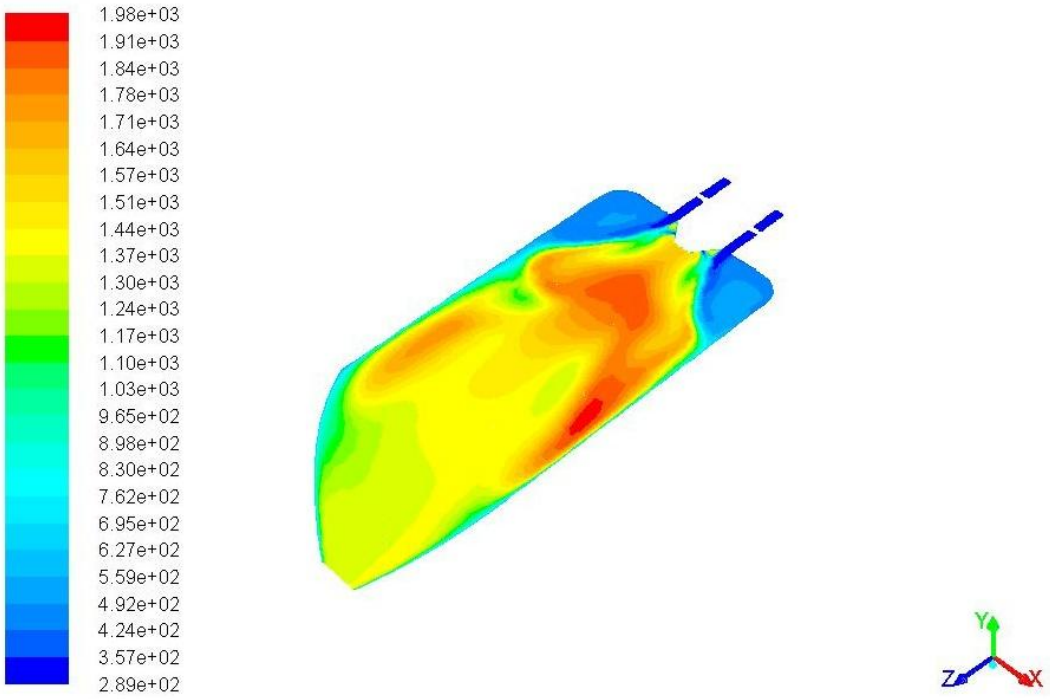

Figure 35 – Contours of static temperature ($\boldsymbol{K}$) for Fuel 1.

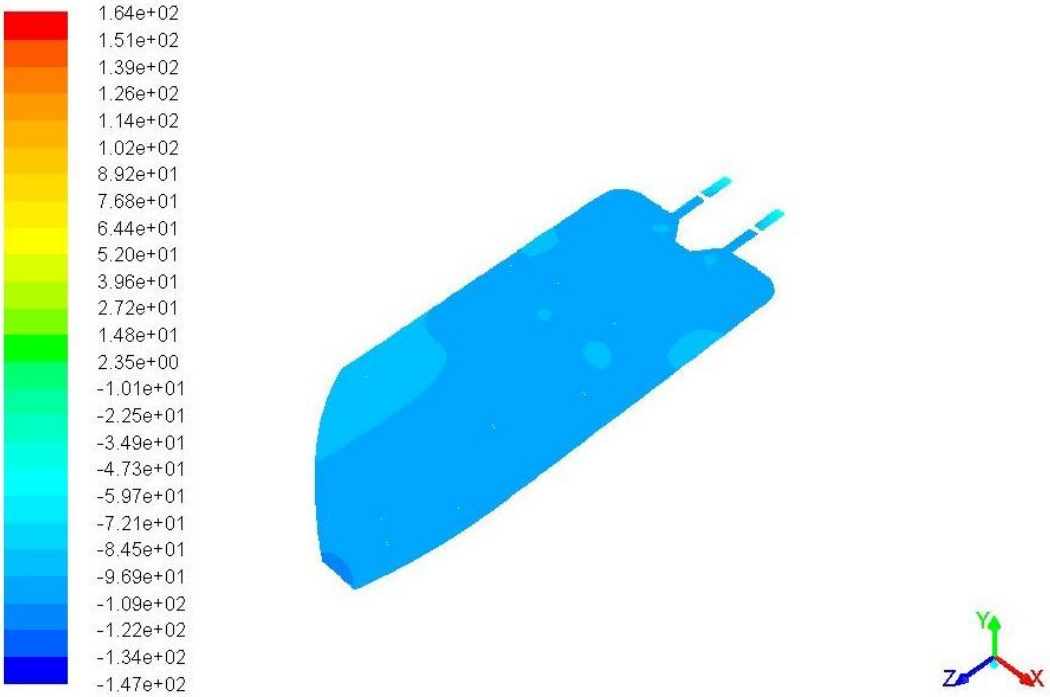

Figure 36 – Contours of static pressure ($\boldsymbol{Pascal}$) for Fuel 1.

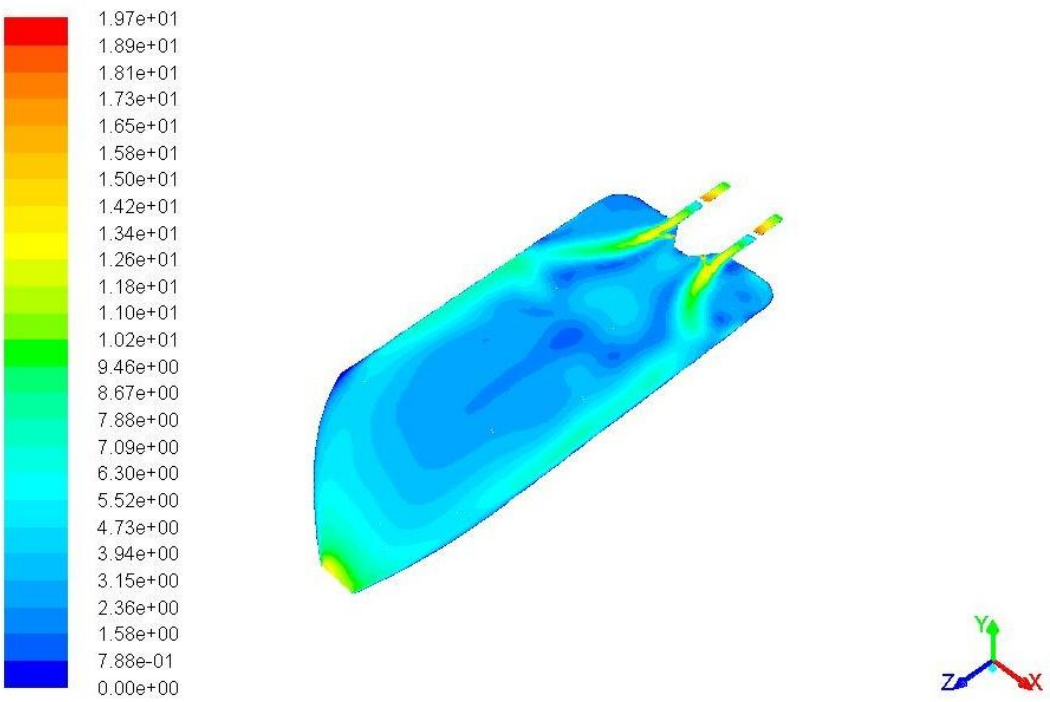

Figure 37 – Contours of velocity magnitude ($\boldsymbol{m/s}$) for Fuel 1.

For the Fuel 2 the contours of static temperature, static pressure, and the velocity magnitude are exposed in Figure 38, Figure 39, and Figure 40.

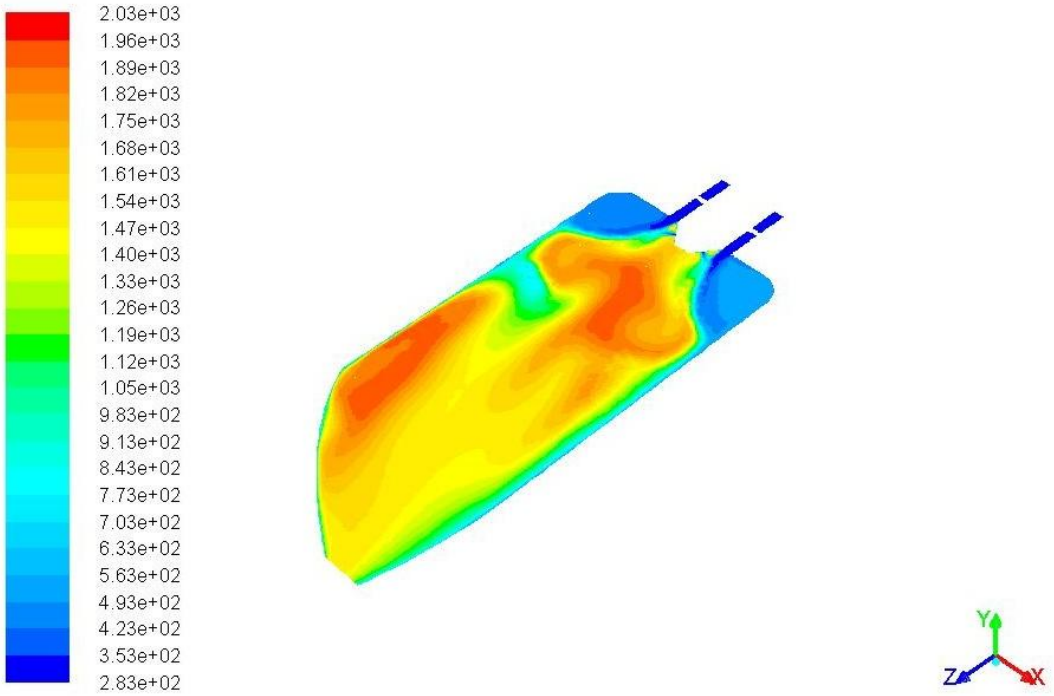

Figure 38 – Contours of static temperature ($\boldsymbol{K}$) for Fuel 2.

Figure 39 - Contours of static pressure ($\boldsymbol{Pascal}$) for Fuel 2.

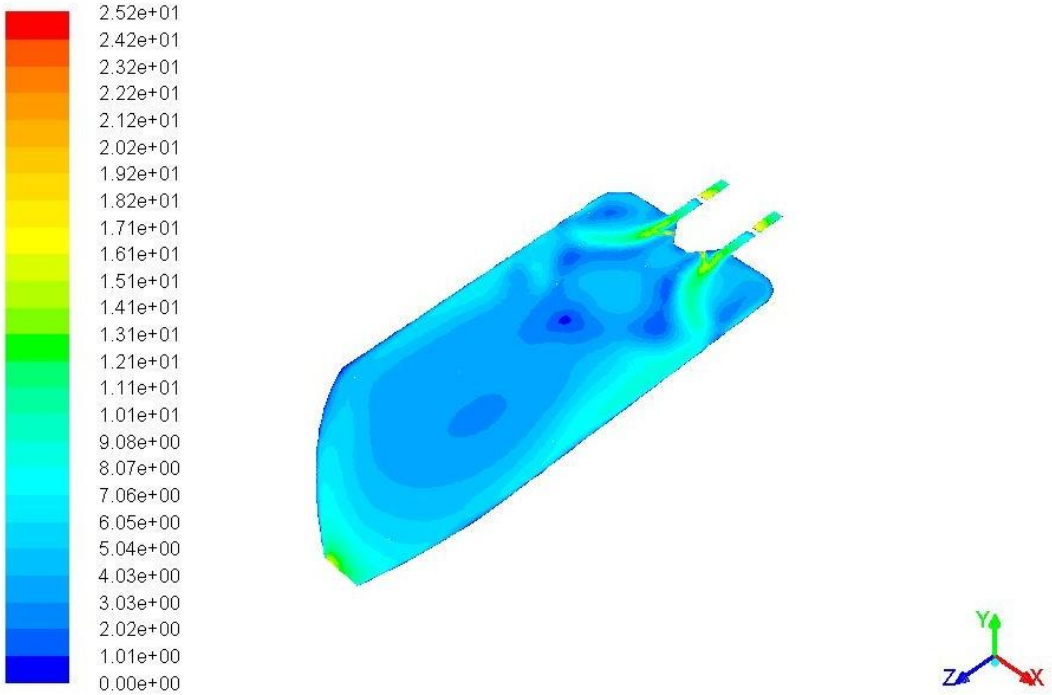

Figure 40 - Contours of velocity magnitude ($\boldsymbol{m/s}$) for Fuel 2.

For Fuel 3 the contours can be seen in Figure 41, Figure 42, and Figure 43.

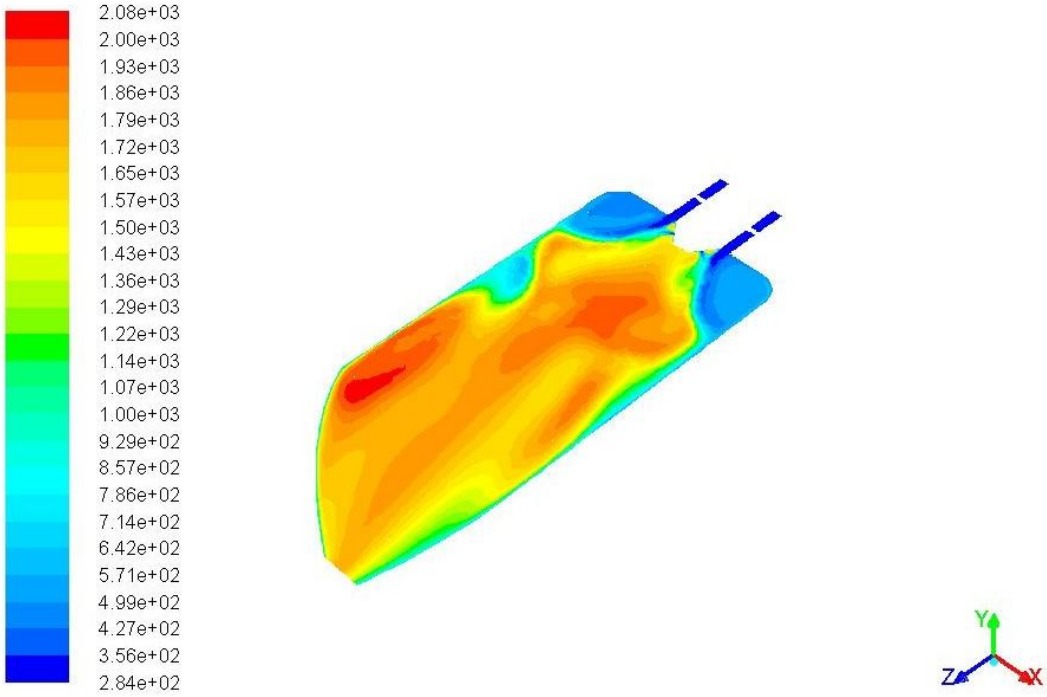

Figure 41 - Contours of static temperature ($\boldsymbol{K}$) for Fuel 3.

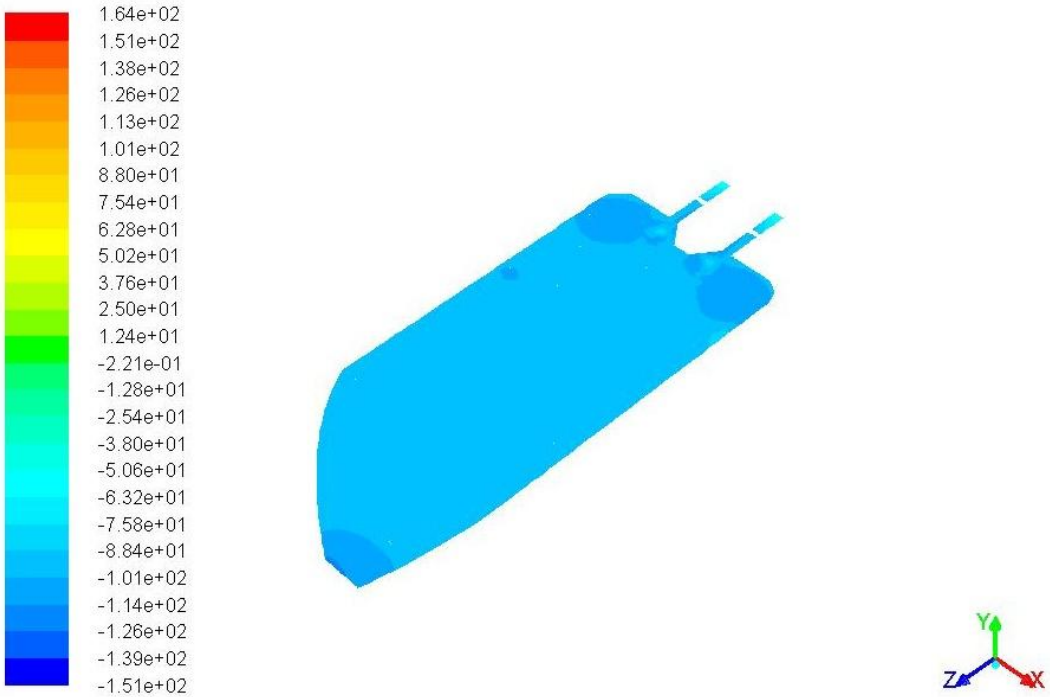

Figure 42 - Contours of static pressure ($\boldsymbol{Pascal}$) for Fuel 3.

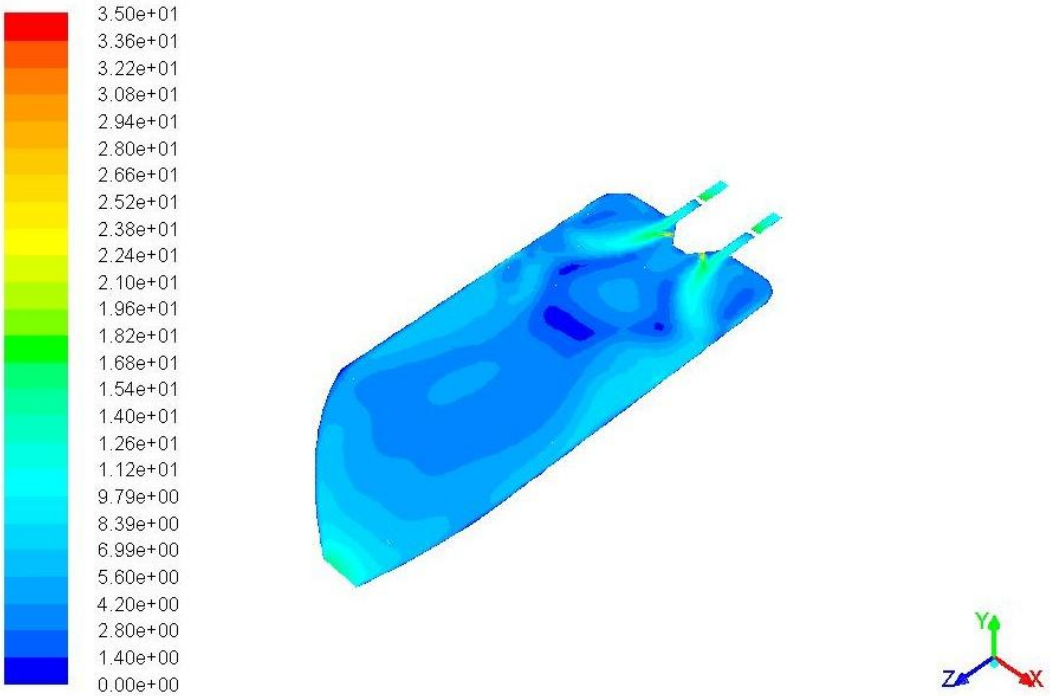

Figure 43 - Contours of velocity magnitude ($\boldsymbol{m/s}$) for Fuel 3.

The contours shown in Figure 44, Figure 45, and Figure 46 are the ones regarding the simulation of the Fuel 4.

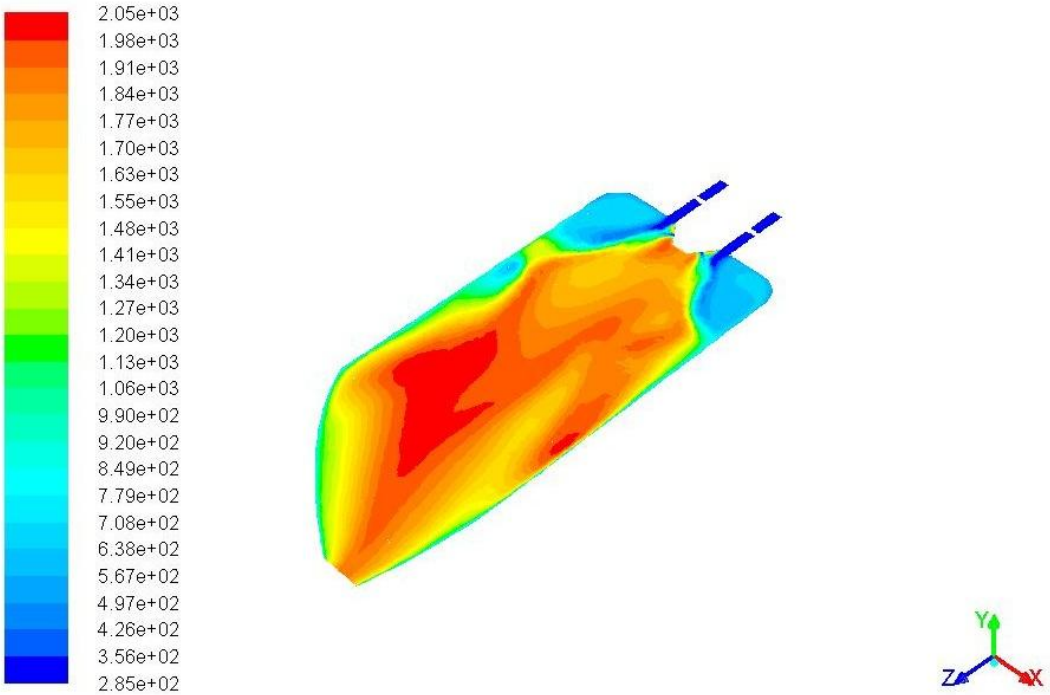

Figure 44 - Contours of static temperature ($\boldsymbol{K}$) for Fuel 4.

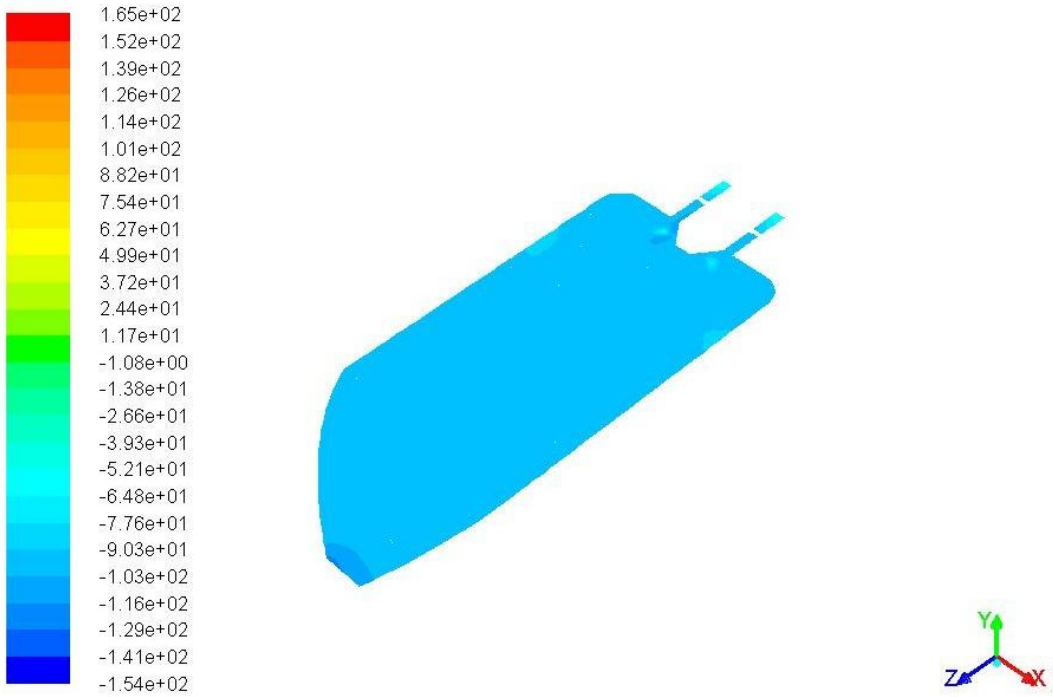

Figure 45 - Contours of static pressure ($\boldsymbol{Pascal}$) for Fuel 4.

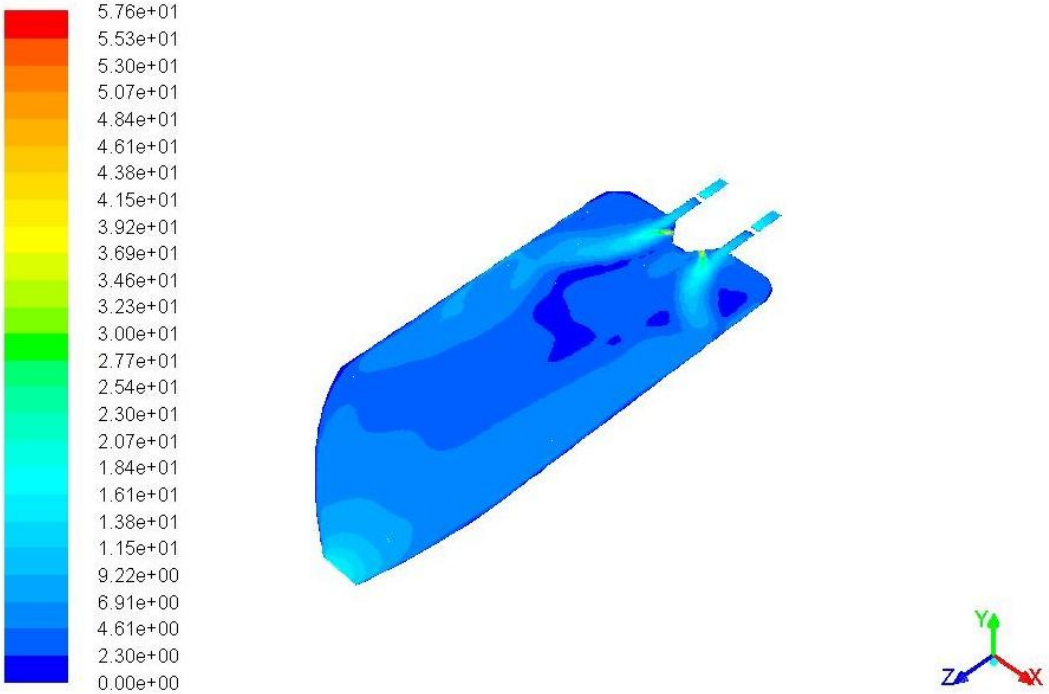

Figure 46 - Contours of velocity magnitude ($\boldsymbol{m/s}$) for Fuel 4.

Finally for Fuel 5 the contours can be observed in Figure 47, Figure 48, and Figure 49.

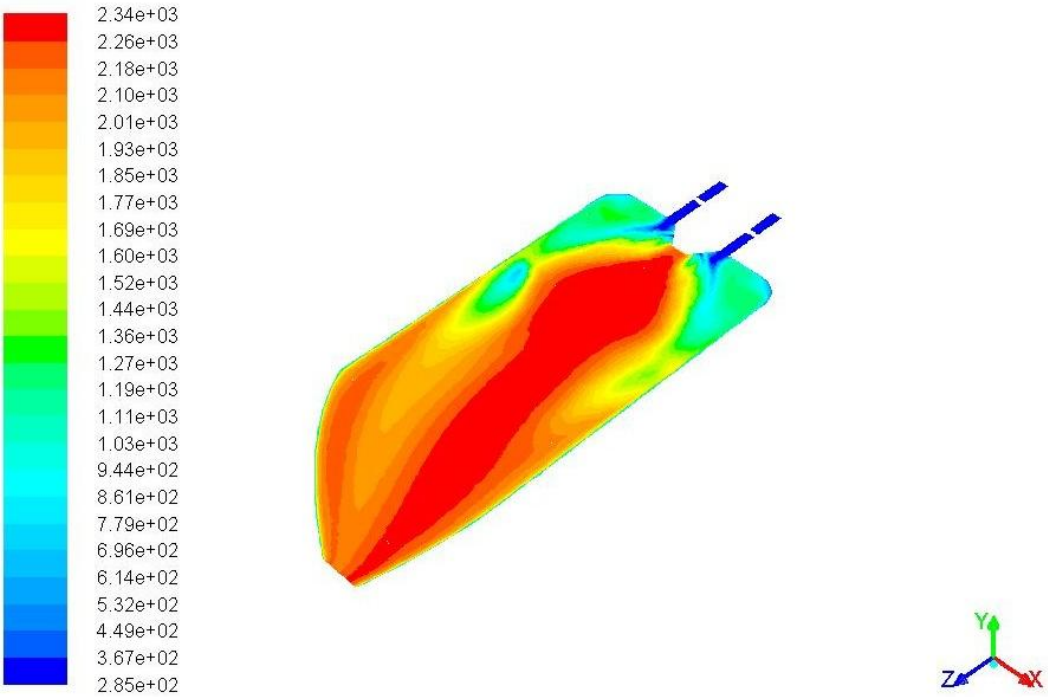

Figure 47 - Contours of static temperature ($\boldsymbol{K}$) for Fuel 5.

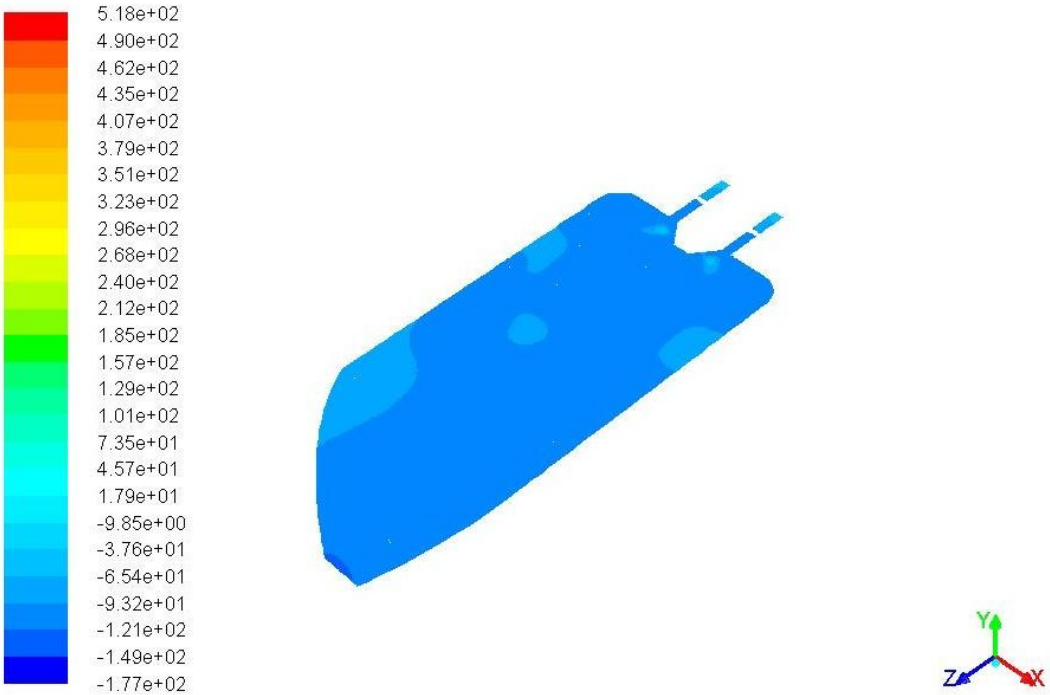

Figure 48 - Contours of static pressure ($\boldsymbol{Pascal}$) for Fuel 5.

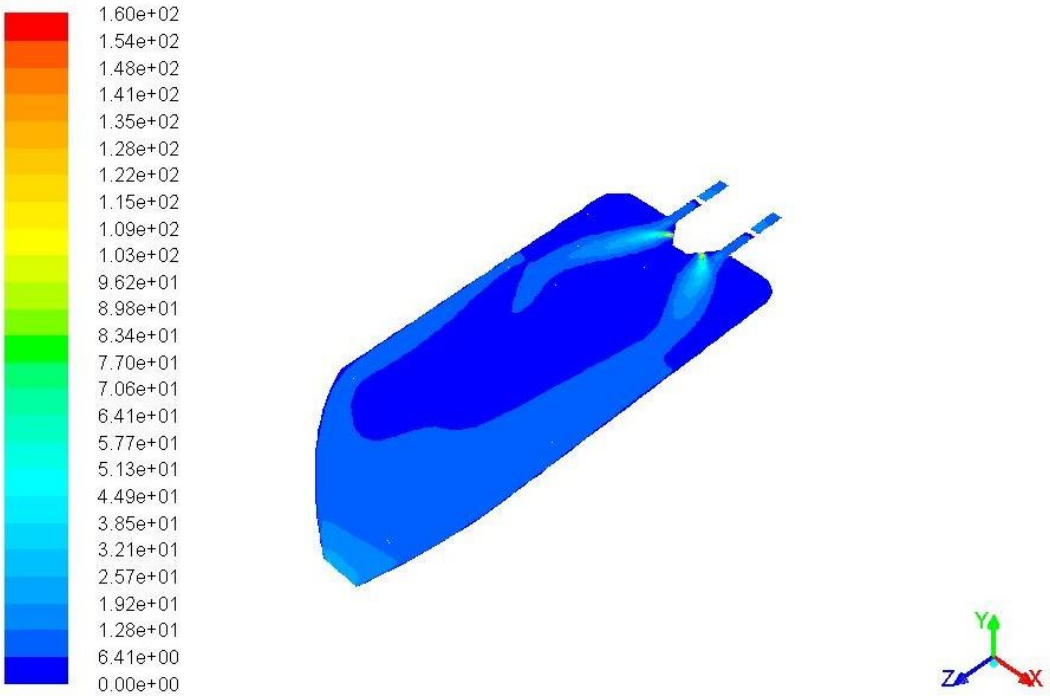

Figure 49 - Contours of velocity magnitude ($\boldsymbol{m/s}$) for Fuel 5.

A concise analysis of the obtained contours give us that

- In a general way there is an increase in the maximum static temperature when more hydrogen is added to methane, being the simulation that used Fuel 5 the one where the maximum static temperature achieved higher values; the minimum static temperature is very similar in all five cases;
- The maximum and minimum values of the static pressure are very similar in the first four simulations, but when pure hydrogen is applied there is a large increase in the maximum static pressure value;
- Lastly for the velocity magnitude the minimum value (zero) is equal in all five simulations, but the maximum value as an enormous increase with the addition of hydrogen to the methane, achieving the greater value when pure H_2 is employed.

5.5 Conclusions

In this part of the dissertation was made a fuel optimization, where methane (CH_4) and hydrogen (H_2) in the pure state, and also methane-hydrogen mixtures were applied. This optimization had as main goal evaluate the average mass fraction of the pollutants CO, CO_2 and NO_x at the exit of the can combustor, but also a brief assessment of the static temperature and pressure, and velocity magnitude in the several CFD simulations was performed.

Finally some of the most important findings attained were that

- The hydrogen addition to methane leads to an increase of the average mass fraction of carbon monoxide as seen in Fuel 2, 3 and 4; but when only pure H_2 is employed there isn't any carbon monoxide emission;
- For the carbon dioxide the average mass fraction at the outlet of the combustor it's null when Fuel 5 is used; and for the methane-hydrogen mixtures the higher the content of H_2 the lower will be the production of CO_2;
- There is an increase of the nitric oxide average mass fraction at the exit of the can combustor as there is an increase in the amount of hydrogen in the fuel composition;
- Regarding the average mass fraction of the nitrogen dioxide the results obtained were inconclusive;
- The augmentation of hydrogen in the can combustor in a general way leads to an increase in the maximum static temperature, static pressure and velocity magnitude.

Chapter 6

Conclusions and Future Work

In this final chapter a succinct summary of the most important conclusions is compiled, and some considerations for future work are stated.

6.1 Conclusions

This dissertation had as main purpose evaluate through a CFD analysis on FLUENT the performance of the combustion in a gas turbine can combustor when fed with methane, hydrogen and methane-hydrogen mixtures without any changes of the general combustion system. So a deeper analysis was made on the emission of the pollutants CO, CO_2 and NO_x.

The chosen combustor chamber geometry was based on the one used by Ghenai [45], that also was used in the work of Pathan et al. [46], but as in both works the data of the geometry is not complete some data has been estimated, and hence some differences occur for the geometry used. Being that so, in order to validate the numerical model the average carbon dioxide and NO mass fractions at the exit of can combustor of the combustion of methane were taken in consideration and compared with the ones obtained by Chaouki Ghenai [45] in is work *"Combustion of Syngas Fuel in Gas Turbine Can Combustor"*, were it was conclude that the fact that there is some divergences in the geometry it leads that the values obtained in the validation simulations are not equal to the ones of Ghenai's work.

Also in the work of Ghenai was applied a $k-\varepsilon$ model, but in our simulation there was the need to employ a $k-\omega$ model, which also contribute to the dissimilarities of the NO and CO_2 average mass fraction at the outlet.

Is important to note that in order for the work to be validated were made simulations using the standard $k-\varepsilon$ model and the SST $k-\omega$ model, where both the results were compared and it was perceived that very similar results were obtained. Once the numerical model was validated, the fuel optimization could be proceeded.

In the fuel optimization was evaluated the average mass fraction of the pollutants CO, CO_2 and NO_x at the exit of the can combustor, but also a brief evaluation of the static temperature and pressure, and velocity magnitude in the several CFD simulations was performed. Finally some of the most important findings obtained were that

- The hydrogen addition to methane leads to an increase of the average mass fraction of carbon monoxide as seen in Fuel 2, 3 and 4; but when only pure H_2 is employed there isn't any carbon monoxide emission;

- For the carbon dioxide the average mass fraction at the outlet of the combustor is null when Fuel 5 is used; and for the methane-hydrogen mixtures the higher the content of H_2 the lower will be the production of CO_2;
- There is an increase of the nitric oxide average mass fraction at the exit of the can combustor as there is an increased amount of hydrogen in the fuel composition;
- Regarding the average mass fraction of the nitrogen dioxide, the results obtained were inconclusive;
- Increasing the amount of hydrogen in the fuel composition, in a general way, leads to an increment of the maximum static temperature, static pressure and velocity magnitude.

6.2 Future Work

In future works it can be carry out some variations in combustion chamber geometry and together with the same fuel variations applied in this study compare the outcomes.

Also different percentages of methane-hydrogen mixtures can be studied in order to comprehend in more detail the impact of the hydrogen addition. Furthermore the methane could be exchanged by other fuels in order to comprehend the impact they have on the combustion when combine with hydrogen.

Asides from numerical studies, experimental ones could also be carried on to better understand if the numerical results are equivalent to the experimental.

Bibliography

[1] M. P. Boyce, *Gas Turbine Engineering Handbook*, Third Edit. Gulf Professional Publishing.

[2] "Peaking Power, Chapter 4: Sir Frank Whittle, Father of the Gas Turbine – A Turbine Blog." [Online]. Available: http://www.pondlucier.com/peakpower/2011/01/11/peakingpower/chapter-4-sir-frank-whittle-father-of-the-gas-turbine/. [Accessed: 11-Jul-2014].

[3] "Turbine Engine History | AviationPros.com." [Online]. Available: http://www.aviationpros.com/article/10383708/turbine-engine-history. [Accessed: 10-Jul-2014].

[4] "Heron of Alexandria -- Britannica Online Encyclopedia." [Online]. Available: http://kids.britannica.com/eb/art-57541/Herons-aeolipile-Heron-of-Alexandria-fashioned-the-first-known-steam. [Accessed: 10-Jul-2014].

[5] P. Coelho and M. Costa, *Combustão*, Orion. Amadora, 2007.

[6] R. Leakey, *The Origin of Humankind*. BasicBooks, 1996, p. 171.

[7] "hydrogen (H) (chemical element) -- Encyclopedia Britannica." [Online]. Available: http://www.britannica.com/EBchecked/topic/278523/hydrogen-H. [Accessed: 18-Aug-2014].

[8] A. H. Lefebvre and R. BallalDilip, *GAS Turbine Combustion: Alternative Fuels and Emissions*, THIRD EDIT. CRC Press Taylor & Francis Group.

[9] Cornell, Clayton B. and C. B. Cornell, *Natural Gas Cars: CNG Fuel Almost Free in Some Parts of the Country*. 2008.

[10] G. E. K. Stefanakos and A. Steinfeld, "Handbook of Hydrogen Energy."

[11] T. YAMAMOTO, N. KOBAYASHI, N. ARAI, and T. TANAKA, "EFFECTS OF PRESSURE ON FUEL-RICH COMBUSTION OF METHANE-AIR UNDER PRESSURE," *Energy Consers.*, vol. 38, no. 10–13, pp. 1093–1100, 1997.

[12] Z. R. Ismagilov, N. V. Shikina, S. a. Yashnik, A. N. Zagoruiko, M. a. Kerzhentsev, V. a. Ushakov, V. a. Sazonov, V. N. Parmon, V. M. Zakharov, B. I. Braynin, and O. N. Favorski, "Technology of methane combustion on granulated catalysts for

environmentally friendly gas turbine power plants," *Catal. Today*, vol. 155, no. 1–2, pp. 35–44, Oct. 2010.

[13] J. Yin, S. Su, X. X. Yu, and Y. Weng, "Thermodynamic characteristics of a low concentration methane catalytic combustion gas turbine," *Appl. Energy*, vol. 87, no. 6, pp. 2102–2108, Jun. 2010.

[14] A. Di Benedetto, G. Landi, V. Di Sarli, P. S. Barbato, R. Pirone, and G. Russo, "Methane catalytic combustion under pressure," *Catal. Today*, vol. 197, no. 1, pp. 206–213, Dec. 2012.

[15] S. de Persis, G. Cabot, L. Pillier, I. Gökalp, and A. M. Boukhalfa, "Study of Lean Premixed Methane Combustion with CO2 Dilution under Gas Turbine Conditions," *energy&fuels*, vol. 27, pp. 1093–1103, 2013.

[16] N. KOBAYASHI, T. Mano, and N. ARAI, "FUEL-RICH HYDROGEN-AIR COMBUSTION FOR A GAS-TURBINE SYSTEM WITHOUT CO2 EMISSION," *Energy*, vol. 22, no. 2, pp. 189–197, 1997.

[17] J. Strohle and T. Myhrvold, "Reduction of a detailed reaction mechanism for hydrogen combustion under gas turbine conditions," *Combust. Flame*, vol. 144, no. 3, pp. 545–557, Feb. 2006.

[18] T. Shudo, K. Omori, and O. Hiyama, "NOx reduction and NO2 emission characteristics in rich-lean combustion of hydrogen," *Int. J. Hydrogen Energy*, vol. 33, no. 17, pp. 4689–4693, Sep. 2008.

[19] Y. Yu, W. Gaofeng, L. Qizhao, M. Chengbiao, and X. Xianjun, "Flameless combustion for hydrogen containing fuels," *Int. J. Hydrogen Energy*, vol. 35, no. 7, pp. 2694–2697, Apr. 2010.

[20] M. C. Lee, S. Bin Seo, J. H. Chung, S. M. Kim, Y. J. Joo, and D. H. Ahn, "Gas turbine combustion performance test of hydrogen and carbon monoxide synthetic gas," *Fuel*, vol. 89, no. 7, pp. 1485–1491, Jul. 2010.

[21] P. Gobbato, M. Masi, A. Toffolo, and A. Lazzaretto, "Numerical simulation of a hydrogen fuelled gas turbine combustor," *Int. J. Hydrogen Energy*, vol. 36, no. 13, pp. 7993–8002, Jul. 2011.

[22] S. Park, U. Kim, M. Lee, S. Kim, and D. Cha, "The effects and characteristics of hydrogen in SNG on gas turbine combustion using a diffusion type combustor," *Int. J. Hydrogen Energy*, vol. 38, no. 29, pp. 12847–12855, Sep. 2013.

[23] H.-J. Tomczak, G. Benelli, L. Carrai, and D. Cecchini, “INVESTIGATION OF A GAS TURBINE COMBUSTION SYSTEM FIRED WITH MIXTURES OF NATURAL GAS AND HYDROGEN,” *IFRF Combust. J.*, no. 200207, 2002.

[24] C. Termaath, E. Skolnik, R. Schefer, and J. Keller, “Emissions reduction benefits from hydrogen addition to midsize gas turbine feedstocks,” *Int. J. Hydrogen Energy*, vol. 31, no. 9, pp. 1147–1158, Aug. 2006.

[25] G. Juste, “Hydrogen injection as additional fuel in gas turbine combustor. Evaluation of effects,” *Int. J. Hydrogen Energy*, vol. 31, no. 14, pp. 2112–2121, Nov. 2006.

[26] V. K. Arghode and A. K. Gupta, “Hydrogen addition effects on methane–air colorless distributed combustion flames,” *Int. J. Hydrogen Energy*, vol. 36, no. 10, pp. 6292–6302, May 2011.

[27] H. Guo and W. S. Neill, “The effect of hydrogen addition on combustion and emission characteristics of an n-heptane fuelled HCCI engine,” *Int. J. Hydrogen Energy*, vol. 38, no. 26, pp. 11429–11437, Aug. 2013.

[28] H.-Y. Shih and C.-R. Liu, “A computational study on the combustion of hydrogen/methane blended fuels for a micro gas turbines,” *Int. J. Hydrogen Energy*, vol. 39, no. 27, pp. 15103–15115, Aug. 2014.

[29] “ANSYS Help 14.” .

[30] “Thermal-FluidsPedia | Integral governing equations | Thermal-Fluids Central.” [Online]. Available: https://www.thermalfluidscentral.org/encyclopedia/index.php/Integral_governing_equations#Conservation_of_Mass_Species. [Accessed: 14-Jul-2014].

[31] G. K. Batchelor and A. D. Young, “An Introduction to Fluid Mechanics,” *Journal of Applied Mechanics*, vol. 35. p. 624, 1968.

[32] P. A. Durbin and B. A. Pettersson Reif, *Statistical Theory and Modeling for Turbulent Flows*, Wiley. 2011.

[33] W. P. Jones and B. E. Launder, “The prediction of laminarization with a two-equation model,” *Int. J. Heat Mass Transf.*, vol. 15, pp. 301–314, 1972.

[34] B. E. Launder and B. I. Sharma, “Application of the energy-dissipation model of turbulence to the calculation of flow near a spinning disk,” *Lett. Heat Mass Transf.*, vol. 1, pp. 131–138, 1974.

[35] B. E. L. and D. B. Spalding, *Lectures in Mathematical Models of Turbulence*. England: Academic Press, 1972.

[36] T.-H. Shih, W. W. Liou, A. Shabbir, Z. Yang, and J. Zhu, "A New k - ε Eddy-Viscosity Model for High Reynolds Number Turbulent Flows - Model Development and Validation," *Comput. Fluids*, vol. 24 (3), pp. 227–238, 1995.

[37] W. C. Reynolds, "Fundamentals of turbulence for turbulence modeling and simulation," 1987.

[38] D. C. Wilcox, *Turbulence Modeling for CFD*. Inc. 5354 Palm Drive, La Cañada, California, 1998.

[39] F. R. Menter, "Review of the shear-stress transport turbulence model experience from an industrial perspective," *International Journal of Computational Fluid Dynamics*, vol. 23. pp. 305–316, 2009.

[40] F. R. Menter, "Two-equation eddy-viscosity turbulence models for engineering applications," *AIAA Journal*, vol. 32. pp. 1598–1605, 1994.

[41] P. Cheng, "Two-Dimensional Radiating Gas Flow by a Moment Method," *AIAA J.*, vol. 2, pp. 1662–1664, 1964.

[42] R. Siegel and J. R. Howell., *Thermal Radiation Heat Transfer*, Hemisphere. Washington DC, 1992.

[43] "Dimensionless wall distance (y plus) -- CFD-Wiki, the free CFD reference." [Online]. Available: http://www.cfd-online.com/Wiki/Dimensionless_wall_distance_(y_plus). [Accessed: 27-Aug-2014].

[44] R. Jauregui and F. Silva, "Numerical Validation Methods." Universitat Politècnica de Catalunya (UPC), Barcelona, Spain, 2008.

[45] C. Ghenai, "Combustion of Syngas Fuel in Gas Turbine Can Combustor," *Adv. Mech. Eng.*, vol. 2010, pp. 1–13, 2010.

[46] F. H Pathan, N. K Patel, and M. V Tadvi, "Numerical Investigation of the Combustion of Methane Air Mixture in Gas Turbine Can-Type Combustion Chamber," *Int. J. Sci. Eng. Res.*, vol. 3, no. 10, pp. 10–12, 2012.

[47] “methane (chemical compound) -- Encyclopedia Britannica.” [Online]. Available: http://www.britannica.com/EBchecked/topic/378264/methane. [Accessed: 18-Aug-2014].

[48] A. J. Chorin, “Numerical Solution of the Navier-Stokes Equations,” *Math. Comput.*, vol. 22, pp. 745–762, 1968.

[49] M. Frey and R. Robson, “Hydrogen as a Fuel Learning from Nature Edited by Richard Cammack,” 2001.

[50] J. Strohle and T. Myhrvold, “Reduction of a detailed reaction mechanism for hydrogen combustion under gas turbine conditions,” *Combust. Flame*, vol. 144, no. 3, pp. 545–557, Feb. 2006.

[51] “What Is Hydrogen Combustion? (with pictures).” [Online]. Available: http://www.wisegeek.com/what-is-hydrogen-combustion.htm. [Accessed: 18-Aug-2014].

[52] “Renewable Hydrogen Network (RH2 Network).” [Online]. Available: http://en.rh2.org/. [Accessed: 18-Aug-2014].

[53] C. C. D. US EPA, “Carbon Dioxide Emissions.” .

[54] “Tox Town - Nitrogen Oxides - Toxic chemicals and environmental health risks where you live and work - Text Version.” [Online]. Available: http://toxtown.nlm.nih.gov/text_version/chemicals.php?id=19. [Accessed: 01-Sep-2014].